Title
Kinetic Resolution of Ras and Arf Signaling Activation by GEFs on Lipid Membranes and in Live Cells

Permalink
https://escholarship.org/uc/item/0d4842z0

Author
Triplet, Meredith Gahn

Publication Date
2017

Peer reviewed|Thesis/dissertation

Kinetic Resolution of Ras and Arf Signaling Activation by GEFs on
Lipid Membranes and in Live Cells

By

Meredith Gahn Triplet

A dissertation submitted in partial satisfaction of the

requirements for the degree of

Doctor of Philosophy

in

Chemistry

in the

Graduate Division

of the

University of California, Berkeley

Committee in charge:

Professor Jay T. Groves, Chair
Professor Ke Xu
Professor James H. Hurley

Summer 2017

Kinetic Resolution of Ras and Arf Signaling Activation by GEFs on
Lipid Membranes and in Live Cells

By

Meredith Gahn Triplet

University of California, Berkeley

Abstract

Kinetic Resolution of Ras and Arf Signaling Activation by GEFs
on Lipid Membranes and in Live Cells

by

Meredith Gahn Triplet

Doctor of Philosophy in Chemistry

University of California, Berkeley

Professor Jay T. Groves, Chair

Supported Lipid Bilayers (SLBs) were used in conjunction with live cell measurements to better understand the activation of the small GTPases Ras and Arf by their respective GEFs SOS and ARNO. As membranes are crucial for proper activity of these proteins, membrane-mimic assays were developed to quantitatively measure kinetic activation and diffusion.

Ras is a common oncogene that causes over 30% of all human cancers. SOS is one of Ras's activators that is known to play a role in the determination of cell fate. The kinetics of SOS activation of Ras was explored in four of the following chapters. Firstly, a nanofabricated platform that incorporated liposome reaction chambers was developed to assess the kinetic activity of single SOS molecules with single nucleotide turnover resolution. Secondly, the measurement of SOS motility and localization in live cells contributed to an understanding of SOS regulation through a stable membrane-associated active state, resulting in SOS endocytosis. Thirdly, a small molecule inhibitor was shown to impact SOS binding to Ras *in vitro* and *in vivo*. Fourthly, the impact of oncogenic Ras mutations on SOS binding and catalytic rate was measured. These results provide insight in the tight regulation of SOS-mediated Ras activation, and also suggest future directions for rational drug design targeting oncogenic Ras.

Arf is a small GTPase in the Ras family that regulates membrane traffic and morphology. In the final chapter, a SLB-based assay for GEF-mediated Arf recruitment studies was developed and diffusion rates for both Arf-GTP and Arf-GDP were measured, demonstrating a well-defined, transient membrane interaction for Arf in the GDP state. Additionally, autoinhibition of the GEF ARNO was confirmed. This yields new insight into the mechanism of Arf signaling initiation.

Overall, it is demonstrated that *in vitro* membrane mimics, in combination with live cell measurements, provide a powerful tool to gain a deeper understanding about the activity and regulation of GTPases.

TABLE OF CONTENTS

I dedicate this to my Christ Church family for welcoming me as I am,
while still supporting me towards becoming a truer version of myself.
Soli Deo Gloria.

LIST OF FIGURES

CHAPTER 1.

INTRODUCTION

Membranes are a crucial component for cell function, as they provide a barrier between the cell and its outside environment; are the entry point for food, information, and pathogens; and are the focal point for many essential protein systems, including actin and signaling synapses (**Fig 1.1**). Despite their importance, technological developments that allow for quantitative imaging of membrane and membrane-mimic environments are relatively recent, and are still under development.

Lipid membranes
Protein interactions with membranes
Lipids themselves are a key component of signaling reactions. The composition of lipids at different cell membranes (such as the endoplasmic reticulum, the Golgi apparatus, and endosomes) are unique and well-maintained[1]. In particular, PIP lipids (phosphoinositides) are often produced or destroyed during signaling in a highly regulated fashion. At least 10 distinct binding domains, including the PH domain, bind to PIP lipids which can recruit proteins to the membrane for further signaling in an environmentally sensitive way[2–4]. In addition to somewhat transient associative reactions, proteins often undergo a post-translational modification step that covalently tethers a lipid group to a specific residue in a way that controls their localization[5]. Additionally, lipids can play a role in bringing proteins in a pathway into the same vicinity to increase the chance of a protein-protein interaction. Although this is often simplified as being a benefit of moving to 2D space instead of 3D space, in fact the reduction of diffusion rate at the membrane is likely to ameliorate any gains in reduced exploration space[6]. In order for confinement to the membrane to provide a benefit a kinetic advantage, the reactions would likely need to be confined to a defined reaction area.

Theoretical and experimental exploration of 2D diffusion
One key feature of lipid membranes is their fluidity. In cells, lipids are constantly exchanging; this feature is important for the interaction of proteins as described above. One simple way to explore the diffusion of proteins associating with or embedded in a lipid bilayer is the simple 2D random walk. This method assumes that a protein takes a step of a given size within a given unit of time, either up, down, left, or right. It assumes that the protein has no bias in its movement, but that the direction is strictly random, and that proteins do not interact with other elements in the environment. These restrictions are not well matched in a live cell environment, but nevertheless, the 2D random walk is a helpful starting point to consider the diffusion of a protein in a membrane given their simpicity[7]. This treatment yields the famous diffusion equation:

$$\langle r^2 \rangle = 4Dt$$

Fick's equations, show below, define the flux of particles diffusing from a high density area to a low density area after the release of a boundary. They highlight the relationship between time and curvature of the concentration gradient, or how quickly the high density region drops off to a low density region[7]. Although still simplistic and analytical, this model can provide some intuition of signaling propagation from one high-density region of the cell to another, low-density region.

$$\text{Net Flux } J_x = -D \frac{\partial C}{\partial x}$$
$$\frac{\partial C}{\partial t} = D \frac{\partial^2 C}{\partial x^2}$$

A more general analytical treatment to explore membranes utilizes concepts from hydrodynamics. This treats the membrane as a fluid, and ignores lipid structure. The main benefit is that is allows for the application of continuum physics. This approximation is sufficient for proteins that are large as compared to the membrane scale (at least three times bigger), and the dynamic timescale is limited to a minimum of 20 collisions per step. There is also a loss of z-directional variations, and other structural components. One interesting conclusion comes up in the application of fluid dynamics to 2D. In 3D, the Einstein-Stokes relation is as follows:

$$D = \frac{kT}{f}$$
$$f = 6\pi\eta_0 r$$

But, in 2D, it is impossible to define f in an infinitely extending fluid due to differing constraints of symmetry. A secondary length dimension is required. However, it does highlight the fact that a cylindrical body moving through a 2D fluid accumulates neighboring particles in its motion[8,9].

Free volume theory, as described by Cohen and Turnbull, operates under the assumption that a particle must move out of the way before another can take its place. This theory is best suited for molecules no larger than lipids, and can well explain the correlation between a fluid's viscosity and density. In this case, fluctuations are considered to be through either activation or redistribution of energy. It separates transport into the two steps of formation of a free volume, and then translational movement to fill the gap. Diffusion is summed for each free volume as shown in the equation below:

$$D = \int_{v^*}^{\infty} D(v_f) p(v_f) dv_f$$

Several additional excellent sources that fully treat the topic of membrane diffusion exist[10–13]. Diffusion can also be measured experimentally using Fluorescent Recovery After Photobleaching (FRAP), which is a bulk method to look at the rate of diffusion of fluorescent

particles into a bleached region (**Fig 1.6**, bottom). Single Particle Tracking (SPT) is a technique that finds and tracks individual fluorescently labelled particles on a membrane surface. SPT requires a large number of traces in order to make statistical conclusions, but it permits the imaging of slow diffusion, as well as different diffusive species in the same sample. Finally, Fluorescent Correlation Spectroscopy (FCS) measures diffusion by imaging the fluctuations of intensity as fluorophores move into and out of a confocal focus point. The intensity readout is then autocorrelated and fit in order to obtain diffusion information. FCS boasts less phototoxicity than either SPT or FRAP, but it is somewhat computationally intensive. FCS has better time resolution than SPT, but worse spatial resolution; it also can be harder to identify multiple species using FCS. In conclusion, all of these theoretical and experimental techniques are complimentary.

Lipid rafts: a theory reconsidered
Although it is well accepted that lipids play an important role of signaling, the exact mechanism of lipid function has been an ongoing conversation. One topic of debate is the role of lipid microdomains in the generation of signaling platforms. Early results used detergents and solubility features to identify distinct membrane components, and suggested that these "lipid rafts" of cholesterol-associating, liquid-ordered phase membrane could serve as protein-binding domains[14]. The imaging of large-scale membrane domains with distinct compositions are known to exist in GUVs and other model membrane environments suggested a large scale for these lipid rafts[15]. As the ability to image membranes at high resolution increased, highly dynamic, very small microdomains were proposed to replace the initial concept of larger, static lipid rafts[16–18]. However, new results exploring lipid diffusion[19] and lipid distribution in live cells[20–22] challenged even this role of lipid rafts, leading to a new conversation about the true role of lipids in signaling processes. A new consensus is emerging around the important role of the actin cytoskeleton in the localization of proteins to membranes, the formation of small microdomains, and the constrained motion of lipids. The actin network and its tethered protein partners can be understood to associate with other proteins that form signaling reaction chambers which confine signaling partners, restrict diffusion, and incorporate an enrichment of key signaling lipids[23–31]. These small-scale, protein-enriched environments likely play a key role in signaling outcome[32,33].

Membrane-bound signaling proteins
The Ras superfamily
Ras is arguably the best-understood membrane-bound signaling protein. The Ras superfamily of small GTPases is composed of five subfamilies: Ras, Rho, Rab, Ran, and Arf[34]. Initial research into the Ras family yielded the insight that these highly regulated proteins are active when bound to GTP, and inactive when bound to GDP[35]. These G-proteins can cycle between active and inactive states, providing a molecular switch (**Fig 1.2**). GTPase activation is catalyzed by Guanine nucleotide Exchange Factors (GEFs) (originally called Guanine Nucleotide Release Proteins (GNRPs), and the deactivation is catalyzed by GTPase Activating Proteins (GAPs)

(given that these proteins activate the GTPase activity of GTPases)[36]. As their name suggests, these GTPases do in fact hydrolyze GTP – but at a rate that is quite slow without the support of an effector to complete the stabilization of a negative charge via an "arginine finger" provided by the GAP that inserts into the active site[37]. GTPases are also mostly membrane-associating, and depend upon the membrane for proper function[38]. Ras, Rho, and Rab proteins are prenylated, which localizes these proteins onto membranes. The highly hydrophobic lipid addition can be shielded by a Guanine Dissociation Inhibitor (GDI) to solubilize the protein[39]. (The name came from the initial discovery of the role of GDIs, rather than their solubilizing properties.)

The functional roles of the subfamilies within the Ras superfamily are quite diverse, but all play an important role in cell viability. The Rho family functions in actin polymerization and morphology, as well in cell-cycle progression[40]. Rab protiens highly depend on GDIs for their function, so are only membrane associated in their GTP form. Rab regulates membrane maturation[41]. Ran, the most abundant of the small GTPase family, is unique in that it is solution soluble. Ran regulates nucleocytoplasmic transport and mitosis[42].

Arf biology
Arf has a unique "interswitch toggle" that leaves a binding pocket for the lipid-associating N-terminus in the GDP-bound state, but that forces this hydrophobic end to locate at the membrane when in the GTP-bound configuration[43]. Therefore, the G-protein cycle shuttles Arf off of and on to the membrane even without the assistance of a GDI (**Fig 1.2,c**). Note that Arf GAPs utilize a "zinc finger" motif, instead of the RasGAP "arginine finger"[44]. Arf protiens function in vescicular trafficking, exocytosis, endocytosis, lipid modification and localization, and actin regulation[44,45].

Arf proteins play different roles on different membrane compartments. Arfs are deeply involved in the regulation of the secretory pathway and transport from the ER, to the ER-Golgi Intermediate Compartment (ERGIC), to the Golgi complex, with specific interactions happening from the *cis*-Golgi to the *trans*-Golgi network (TGN). Arfs 1 and 4 interact at the *cis*-Golgi, where they recruit CERT, FAPP2 and OSBP, facilitating the transport of ceramide and glucosylceramide lipids, as well as sterols, to later stages of the Golgi. Arf recruits all three of these proteins to their proper location, in conjunction with their PH domains[44]. Arf3 localizes to the TGN, where it regulates exocytosis. Additionally, Arfs recruit coat proteins – such as coatamer complex I (COPI) – to mediate the formation of lipid droplets. At the ERGIC, Arf1 acts with COPII to regulate the formation of lipid droplets. The exact role of Arf in this highly involved pathway is not yet clear[46]. Arf1 and Arf4 work with PLA2G6-A to regulate ERGIC morphology; Arf1 and Arf4 bind to PLA2G6-A and deactivate it, preventing the generation of ERGIC tubules[47].

Arfs also play an important role on plasma membranes. Arfs can recruit phosphatidylinositol-4-phosphate 5-kinase (PtdIns4P5K) to generate PtdIns-4,5-bisphosphate (PtdIns(4,5)P_2) lipids, and

Arf6 is believed to be the major such driver[44]. Arf1 also exhibits such functionality[48]. Once activated, Arf6 works with ARL4 to recruit cytohesin (a GEF also known as ARNO) to the plasma membrane, where a positive feedback loop further activates Arf1. Cytohesins interact with an IPCEF-DOCK180 complex to recruit and activate Rac (a Rho GTPase). As PIP lipids and Rho are both actin regulators, Arf's tight interfaces with these proteins lead to regulation of the cortical actin network[44,46].

Ras: a highly studied oncogene
Because they play a major role in oncogenesis, the Ras subfamily is the most studied branch of the eponymous superfamily; in fact, Ras mutations cause over 30% of all human cancers. The cancer-causing potential of these proteins is apparent given their function in cell proliferation, differentiation, and survival, among other things[45,49]. Despite its clinical relevance, no Ras-specific drug targets have yet made it to market[50]. This makes Ras a prime target for additional research.

Most oncogenic mutations are at the 12, 13, or 61 codons. These mutations are understood to lead to hyper-proliferation, either through increased spontaneous nucleotide exchange, or decreased GTP hydrolysis activity (**Fig 1.4**)[51]. The G12 and G13 residues both have van der Waals interactions with a GAP arginine finger[51,52]. Larger resides at these locations prevent GAP binding (note star in **Fig 1.4a**, showing the insertion site of the arginine finger). More importantly for the G13 residue, however, is its close proximity to the nucleotide; a larger, and particularly charged, residue at this location greatly stabilizes the nucleotide-free state of Ras, increasing the rate of intrinsic exchange by over an order of magnitude (**Fig 1.4b**)[53]. The Q61 residue is important for both intrinsic and GAP-mediated hydrolysis; the amide charge-stabilizes the γ-phosphate of GTP as it is hydrolyzed, and also hydrogen bonds with the GAP during the transition state[51]. Note that Q61 is also near the active nucleotide binding site on Ras, and further is well positioned on Switch 2 to have interactions with effector proteins (**Fig 1.4a**).

The Ras protein itself has three different isoforms: N-Ras, H-Ras and K-Ras (with the two splice variants K-Ras4A and K-Ras4b). Although all three isoforms interact with the same GAPs and GEFs, their activation leads to different signaling outcomes – likely due to changes in their membrane localization. While H-Ras and N-Ras are present throughout the cell, K-Ras is less prevalent at the Golgi. Although the catalytic core is highly conserved, the hyper-variable region (HVR) varies substantially between these isoforms and is suspected to play a role in their different localization. Additionally, the lipid modifications are distinct for these different isoforms. All three have a membrane-associating C-terminal CAAX motif and are farnesylated in a post-translational modification step. All three are methylated at the C-terminus, although K-Ras is methylated the most efficiently. However, whereas N-Ras and H-Ras are palmitoylated, K-Ras is not; K-Ras has a polylysine sequence that interacts with negatively charged bilayers[54]. The GDI-like protein PDEδ also plays a role in proper Ras localization[55]. These isoforms also differ in prevalence in different cancers. K-Ras is the most common oncogene among the three,

and is especially associated with pancreatic and colorectal cancers; N-Ras is associated with melanoma and acute myelogeneous leukaemia; and H-Ras is associated with follicular and papillary thyroid, bladder, and renal cell cancer[56].

Ras: a molecular switch in signal transduction
Ras interacts with three GEFs: SOS, RasGRP, and RasGRF. These GEFs – SOS in particular – have been highly studied[57]. The Ras GAPs have not demonstrated the same level of regulatory complexity. Ras GAPs include: SynGAP, p120, NF1, RASAL, CAPRI, GAP1^m, and GAP1^{IP4BP}. Ras GEFs and GAPs regulate Ras as it moves through the G-protein cycle (**Fig 1.2b**)[58]. Besides its role in cancer, Ras is an interesting signaling target due to its role in translating an analog molecular input to a digital, activated/non-activated output. This role has been particularly explored via SOS activity[59], and continued research is still exploring Ras activation as a deterministic step.

SOS is a highly autoinhibited protein. The full protein includes a C-terminal PR domain, as well as N-terminal Histone-fold, Dbl-homology domain, and PH domain PIP-binding site, in addition to the catalytic core of REM domain and a CDC25 domain. Even with only the catalytic core, SOS is fully active; SOS can stay associated to the membrane through a stable interaction at the allosteric site (**Fig 1.3**). Upon SOS allosteric binding to GTP-bound Ras, the catalytic core slightly opens to further activate the CDC25 domain. SOS can then processively activate a pool of Ras at the catalytic site, while maintaining membrane association through the allosteric site[60]. Both the PH and the Histone fold occlude the Ras binding sites; however, upon association with membranes, these domains serve to increase SOS catalysis. Similarly, the PR domain occludes the SOS catalytic binding site, but is relieved by Grb2 binding[61,62].

Activation of Ras by SOS occurs in T-cell triggering. As T-cells are known to signal in response to single-molecule levels of activating antigen, this system is particularly interesting to explore with high resolution. In this pathway, a T-Cell Receptor (TCR) binds to an antigen on the exterior membrane leaflet, and a conformational shift causes phosphorylation to occur on the cytosolic leaflet. Lck, Zap-70, and LAT are recruited; LAT then recruits Grb2[33,63]. Grb2 binds the PR domain of SOS, bring SOS into close proximity with the membrane for activation of Ras (**Fig 1.1**). However, this is simply one paradigm; additional activating signals other than TCRs include B-Cell Receptors (BCRs), Receptor Tyrosine Kinases (RTKs), Integrins, Cytokine recpetors, and GPCRs. The agonist-mediated activation of these transmembrane receptors triggers activator proteins to recruit Grb2 and SOS[57]. RTKs are distinct from TCRs in that they themselves include a kinase phosphorylation domain[64]. Other GEFs besides SOS play a role in Ras activation; GPCRs can activate Ras through Ca^{2+} signaling and RasGRF, and PLC activation transpires through Ca^{2+} signaling and RasGRP. Although there are distinctions between the proteins involved in each signaling pathway, all utilize specific interactions in a signaling cascade to achieve both specificity and robust outcome.

After Ras activation, the signal is relayed to achieve protein production through a downstream kinase cascade. Downstream effectors including the Raf1 – MEK – ERK – MAPK pathway, but also PI3K, RASSF, TIAM, RALGDS, PLCε, and RIN1[65]. Although crosstalk between all of these distinct Ras-mediated signaling pathways has been speculated, such coordination is as of yet poorly understood. In the most studied kinase cascade pathway, Ras activates Raf1 by recruiting it to the membrane. Raf1 serves as a kinase, and is activated upon its interaction with Ras. Raf1 phosphorylates MAPK/Erk Kinase (MEK), which then in turn phosphorylates Erk1 and Erk2, activating them. Erk1 and Erk2 have a wide range of targets, including cytosolic proteins. Once phosphorylated, Erk forms dimers that are transported into the nucleus and activate the Ets family of transcription factors via phosphorylation, including Elk1. Elk1 is a highly studied transcription factor[64]. See **Fig 1.1** for a schematic of Ras signaling embedded in the T-Cell from antigen binding to transcription in the nucleus.

Technical advances in membrane studies
SLBs
In order to study membrane-associating proteins *in vitro*, a membrane mimic is required. Supported lipid bilayers (SLBs) serve as an excellent such mimic, and can be made on glass slides by piranha etching glass slides to create a negatively charged surface. An etching time of 5-10 minutes is recommended. A shorter etch might not sufficiently charge the slide, and a longer etch can make the thin glass too brittle to effectively work with. Note that different surface treatments impact the resultant mobility of the SLB[66]. Phospholipids, which in physiological contexts typically have a negative charge, assemble on this negative surface through a thin (~1nm) intermediary layer of water molecules arranged to balance the charge. The layer of phospholipids on top of the glass is then mobile.

The lipids are prepared first in chloroform to achieve the desired mixture. The chloroform can be removed using a rotovap, and the lipids can be resuspended in an aqueous solution. Upon resuspension, lipids form a wide variety of conformations, including multilamellar vesicles; these can be sheared down to single lamellar vesicles (SUVs) using either extrusion or sonication (**Fig 1.5**). Several freeze-thaw cycles can also increase the amount of SUVs in the sample, but this technique is not preferred. Extrusion creates a shear force as the lipids are pushed through a small pore (typically 30nm); note that the resultant vesicles are typically larger than the pore size, as vesicles can withstand some deformation pressure without rupturing[67]. (Vesicles pushed through a 30nm pore are typically 50-70nm in diameter.) Acceptable vesicles can be formed upon 7-13 passes through an extruder, although even greater consistency can be obtained by extruding up to 21 times. Sonication functions by rupturing the multilamellar vesicles, allowing for the creation of smaller, more uniform SUVs. As the sonicator can heat the sample, it is important to keep the vesicles in an ice bath during sonication to prevent unnecessary oxidation of the lipids. As extrusion is highly dependent on the pressure and speed applied to the lipid sample as it is pushed through the pores, results can vary substantially from day to day; in contrast, sonication results can be more consistent.

It is important to note that liposomes made in this way can have a wide range of lipid compositions between them, even from the same batch[68]. The size distribution of SUVs can be measured through Dynamic Light Scattering (DLS) or through quantitative intensity readings[69]. Note that accurate interpretation of DLS data can be complicated by the presence of any aggregates or dust within the sample, as larger sized particles can overwhelm the signal. For proper thresholding, it is imperative to test the operation of the DLS by using a standard (such as beads) of a known size that are in a comparable range to the sample of interest. If desired, SUVs can be used as a platform end-point, often when tethered to a PLL-g-PEG surface[70].

Upon exposure to the negative glass slide, SUVs spontaneously form SLBs (**Fig 1.5**), particularly if the salt concentration is increased. The charges on lipid head groups interact with salts in solution, and this interaction can change the effective size. Based on the size ratios between lipid head groups and tail groups, different lipid structures are preferred. For example, micelles form when the lipid tail group is much smaller than the lipid head group, such as when there is only one non-polar tail (soaps generally fall into this category). Increasing the salt concentration can increase the size of the lipid head groups, and favor the SLB confirmation (cylindrical) over the SUV form (truncated cone). This also can explain the varying difficulty of making bilayers with different compositions. It can be quite technically challenging to make bilayers with a charge of less than a 3% charge. After the bilayer has been formed (a process that takes roughly 30 minutes), small defects still remain on the glass slide. These defects can nucleate bilayer destruction, especially under buffer exchange. (Bilayers are sensitive to salt concentration, and can be destroyed if placed under a large change.) In order to prevent defect nucleation, it is important to block the bilayer with a protein such as casein or BSA. These proteins bind non-specifically to the negatively charged defects, and stabilize the surrounding lipids. Maintaining casein in all protein addition steps is recommended in order to reduce the amount of non-specific binding of the protein of interest to these defects. For additional information on the creation of lipid bilayers, see Ref. [71]. For additional information on the properties of lipid surfaces, see Ref. [72].

Nanodiscs
Another, more recently developed membrane mimic are nanodiscs. These are small lipid domains that are encapsulated by a protein band, and can be either about 8 or 11nm in diameter[73]. Nanodiscs prove promising in applications where proteins need to be individually confined while yet preserving the membrane environment, such as for structural determination. However, the small size of the nanodisc can create problems in the heterogeneity of lipid composition. If a lipid should make up a small fraction (1%, for example) of the membrane surface, the random fluctuation of just a lipid or two can make a large difference in the exposure felt by a protein on a single nanodisc. Additionally, the synthesis of nanodiscs is much more involved than that of SUVs, and has not yet been as well characterized as SLBs.

TIRF microscopy

SLBs, and other surface functionalized platforms, work in tandem with Total Internal Reflection Fluorescence (TIRF) microscopy for to provide quantitative kinetic information about signaling systems *in vitro*[74] (**Fig 1.6**). TIRF is a surface imaging technique that uses an incident wave sent through an objective at an angle to lead to refraction through the change of medium (oil to coverglass to aqueous buffer) to create an evanescent wave with minimal penetration depth (hundreds of nanometers)[75]. The depth of evanescent wave propagation is dependent upon the critical angle (θ) of incident wave encounter with the sample, according to the following equations, where d is the propagation depth; n_1 and n_2 are the refractive indices for the sample and coverglass, respectively; λ is the wavelength of light; I_z is the intensity at depth z; and I_0 is both the initial intensity and the intensity at depth 0:

$$\theta_{critical} = \sin^{-1}\left(\frac{n_1}{n_2}\right)$$

$$d = \frac{\lambda_0}{4\pi\sqrt{n_2{}^2 sin^2\theta - n_1{}^2}}$$

$$I_z = I_0 e^{-z/d}$$

Given the dependence of both intensity and depth on the refractive index and the angle, consistency in the RI of the imaging oil is imperative, as is an assessment of the incident angle before each experiment. Additionally, the alignment of the light path through the microscope system should be regularly checked and optimized[76].

For a general introduction to fluorescence microscopy, see Refs. [77] and [78].

Micro- and nano-fabrication

Surface fabrication, both on the micro and the nano scale, can also be used in conjunction with SLBs and TIRF imaging to create patterned features. Fabricated substrates can allow for exploration of membrane curvature, Raman-enhanced measurements, forced organizational constraints, and other specialized assays[79–82]. Several techniques for surface fabrication exist, each best suited for differing applications. For techniques where the exact shape and distance between features is less important, colloidal dispersions can be the most efficient way of creating a structure[83]. Printing techniques allow for the reproduction of pre-defined features, and use some combination of deposition and removal steps to form shapes of the specified pattern. In pattern printing, a master mold is generally used to create a printable polymer stamp. The stamp is then bathed in the "ink" to be printed (often a light-reactive chemical or a catalyst) is the desired areas, with subsequent release and etch steps to yield the desired conformation. Traditional printing techniques yield micron-scale patterns[84]. Lithography is a more sensitive technique that allows for design formation at the nano-scale. Photolithography uses a light sensitive layer called a photoresist, which can then be activated in defined regions by exposure to light through a mask. Masks are costly and time-intensive to produce. Scanning Electron

9

Microscopy (SEM) and Focus Ion Beam (FIB) etching both allow for more specialization between samples. Each technique utilizes a "gun" of material (either electrons or ions) to directly ablate the sample surface. Both can also be used for imaging of conductive samples, but can damage delicate surfaces. FIB has the smallest theoretical resolution, being in the tens of nanometers range[85,86].

Live cell imaging
While SLBs and TIRF provide an essential platform for controlled, quantitative measurements *in vitro*, the true strength of this platform can be realized in conjunction with live cell measurements. The physiological relevance of data can best be understood by comparison to the cell environment, and data sets from *in vitro* and *in vivo* experiments can suggest the best, most accurate interpretation when considered together. The development of several fluorescent proteins, in combination with TIRF, confocal, super-resolution, and FRET microscopy, has provided the opportunity to make live-cell measurements that can be directly compared to SLB counterparts[87,88]. Live-cell imaging is a growing field with new techniques earning high-profile reception[89–92].

Herein, SLBs and TIRF microscopy are used in conjunction with live cell measurements to better understand the regulation and kinetics of the small GTPases Ras and Arf as they are activated by the GEFs SOS and ARNO, respectively.
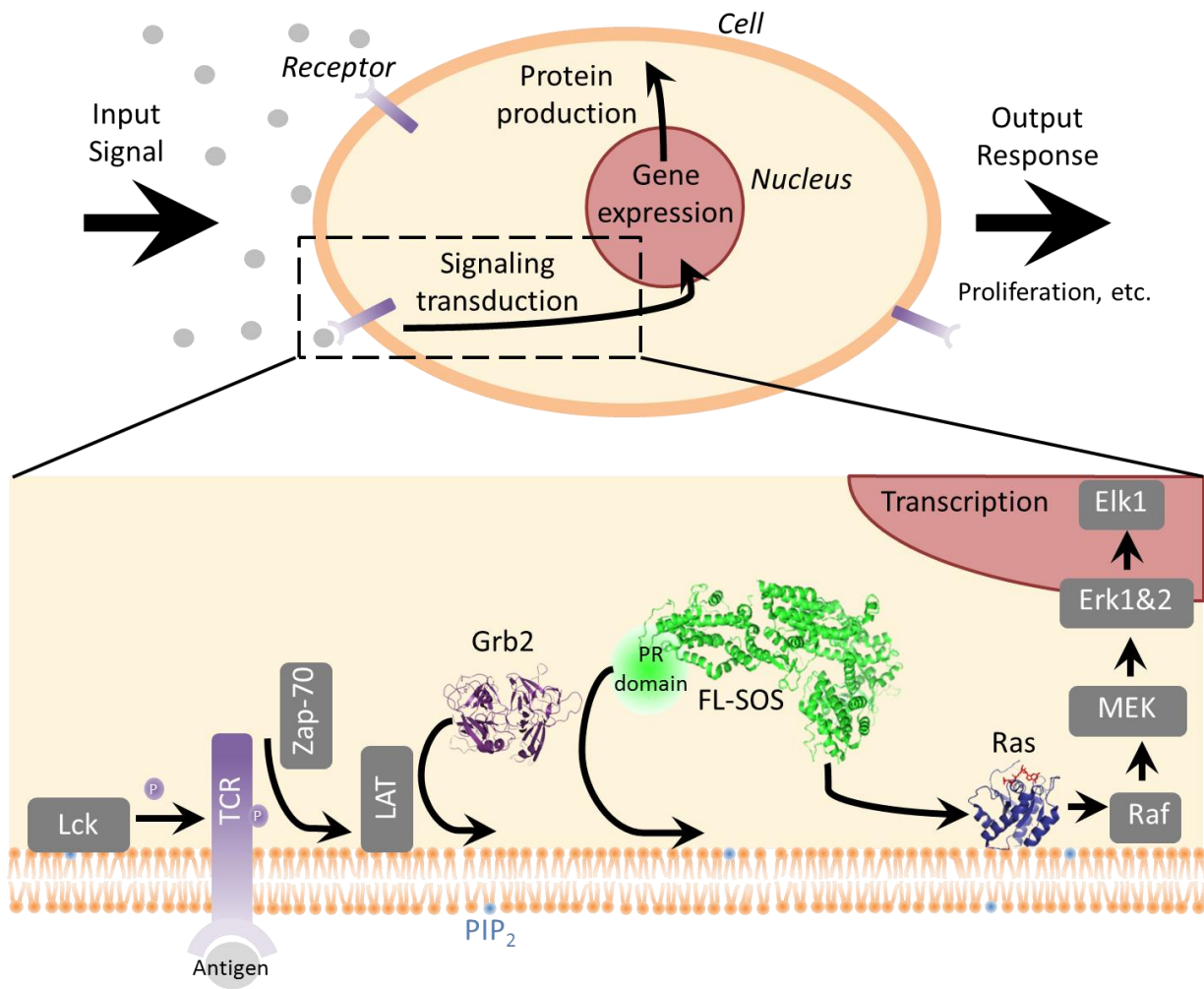
Figure 1.1. The role of the cell membrane in signal response. Top: Schematic of cell responding to a generic input signal. Bottom: interacting proteins in response to TCR stimulation by antigen, leading finally to SOS activation of Ras and activation of the MAPK pathway.
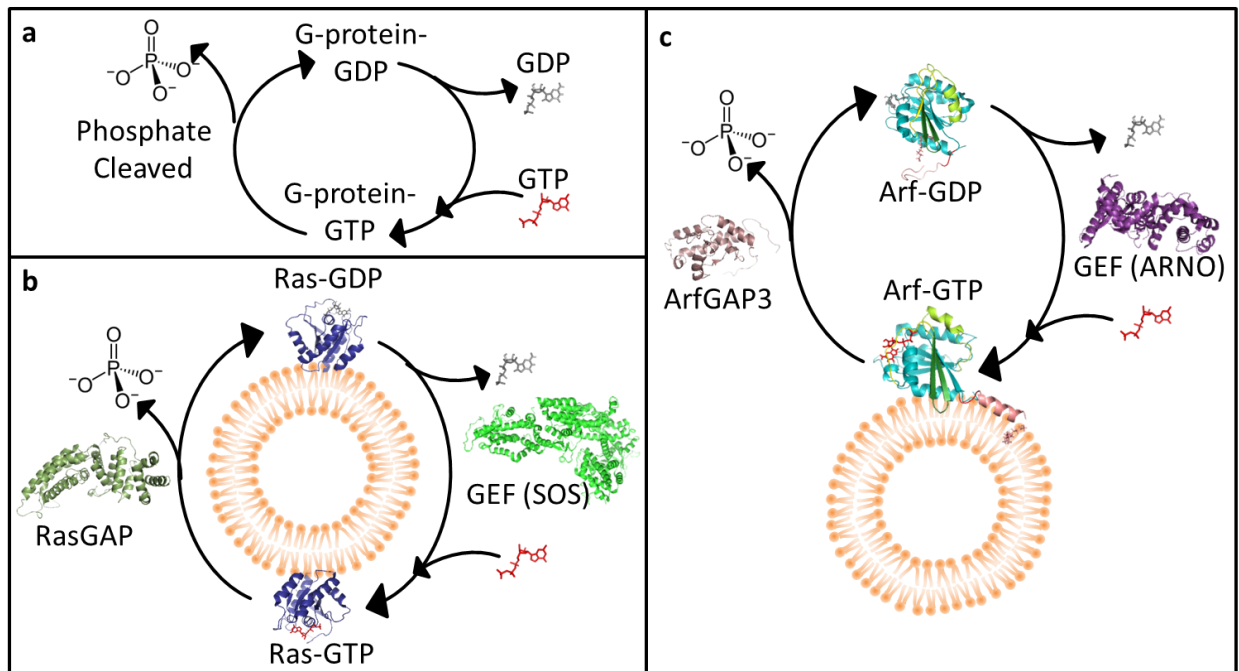
Figure 1.2. The G-protein cycle of activation and deactivation. (**a**) Generalized schematic of G-protein activation via nucleotide exchange, and deactivation via phosphate cleavage. (**b**) G-protein cycle for Ras. Ras activation through nucleotide exchange is catalyzed by GEFs such as SOS, shown (PDB 3KSY) to form Ras-GTP (PDB 4EFL). Deactivation is catalyzed by GAPs, such as RasGAP, shown (PDB 1WQ1) to form Ras-GDP (PDB 1CRQ). (**c**) G-protein cycle for Arf. Arf-GDP (2K5U) is not membrane associated, but Arf-GTP (PDB 2KSQ) does bind stably to membranes. Arf activation is catalyzed by GEFs such as ARNO, shown (PDB 4Z21). Arf deactivation is catalyzed by GAPs, such as ArfGAP3, shown (PDB 2CRW).
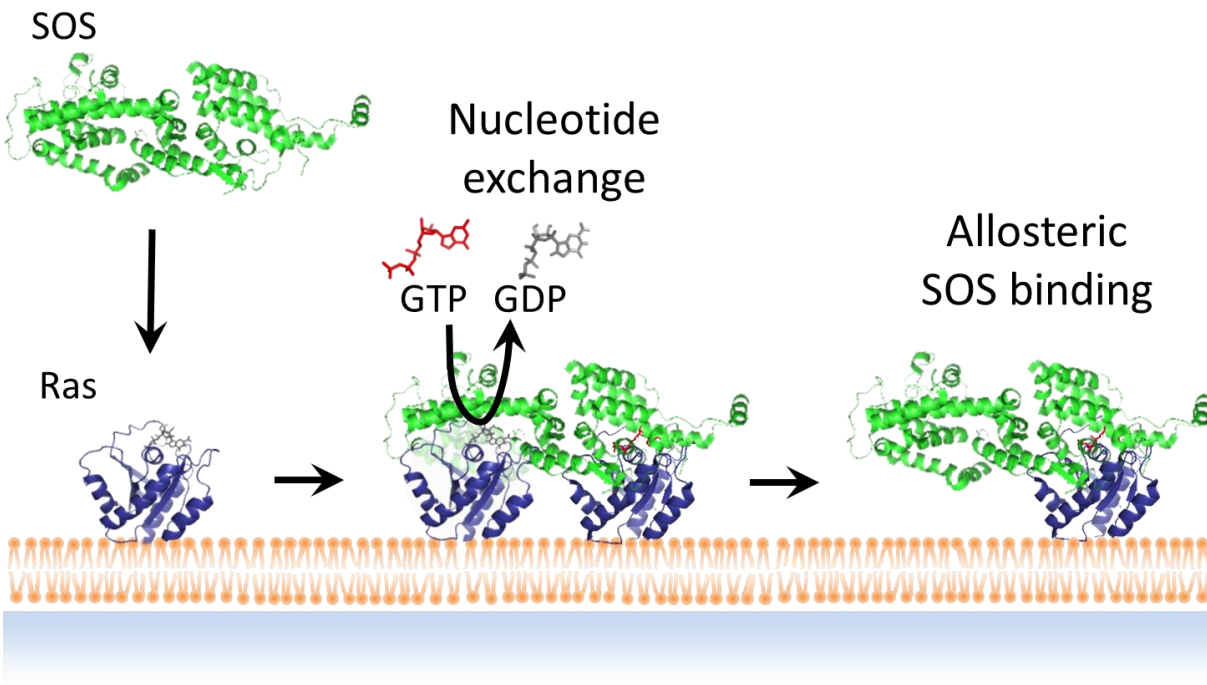
Figure 1.3. SOS recruitment to and activation of Ras. The catalytic domain of SOS (PDB 2II0) binds to membrane-associating Ras via allosteric binding, and can catalytically activate Ras at the catalytic site.
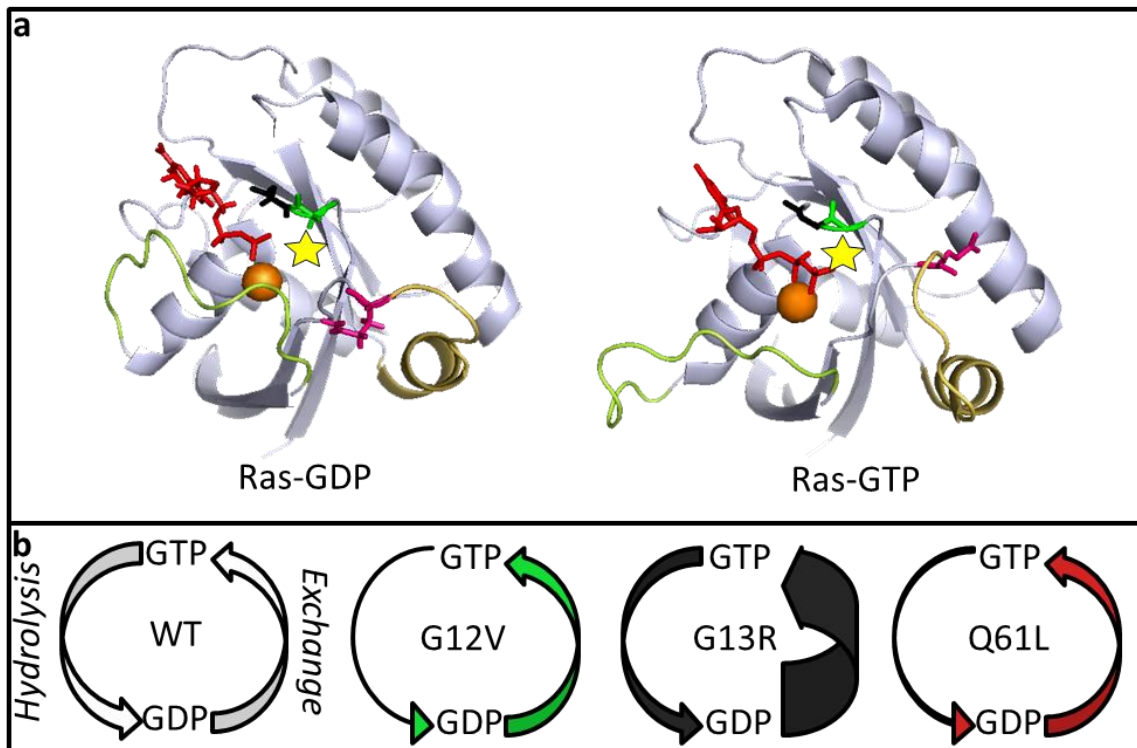
Figure 1.4. Mechanism of Ras oncogenesis. The G12 and G13 locations have van der Waals interactions with the GAP arginine finger, and their mutations reduce GAP-mediated hydrolysis. (**a**) Structures of Ras-GDP (PDB 1CRQ) and Ras-GTP (PDB 4EFL) with nucleotide highlighted in red; Mg2+ in orange; G12 in black; G13 in green; and Q61 in pink. Switch 1 is highlighted in light green, and Switch 2 is highlighted in yellow-orange. The yellow star marks the insertion site of a GAP arginine finger. (**b**) Schematic showing the impact of specific mutations at the most common oncogenic residues. G12V and G61L have decreased hydrolysis rates, while G13R has an increased exchange rate. Note that these changes all result in an over-activation of Ras.
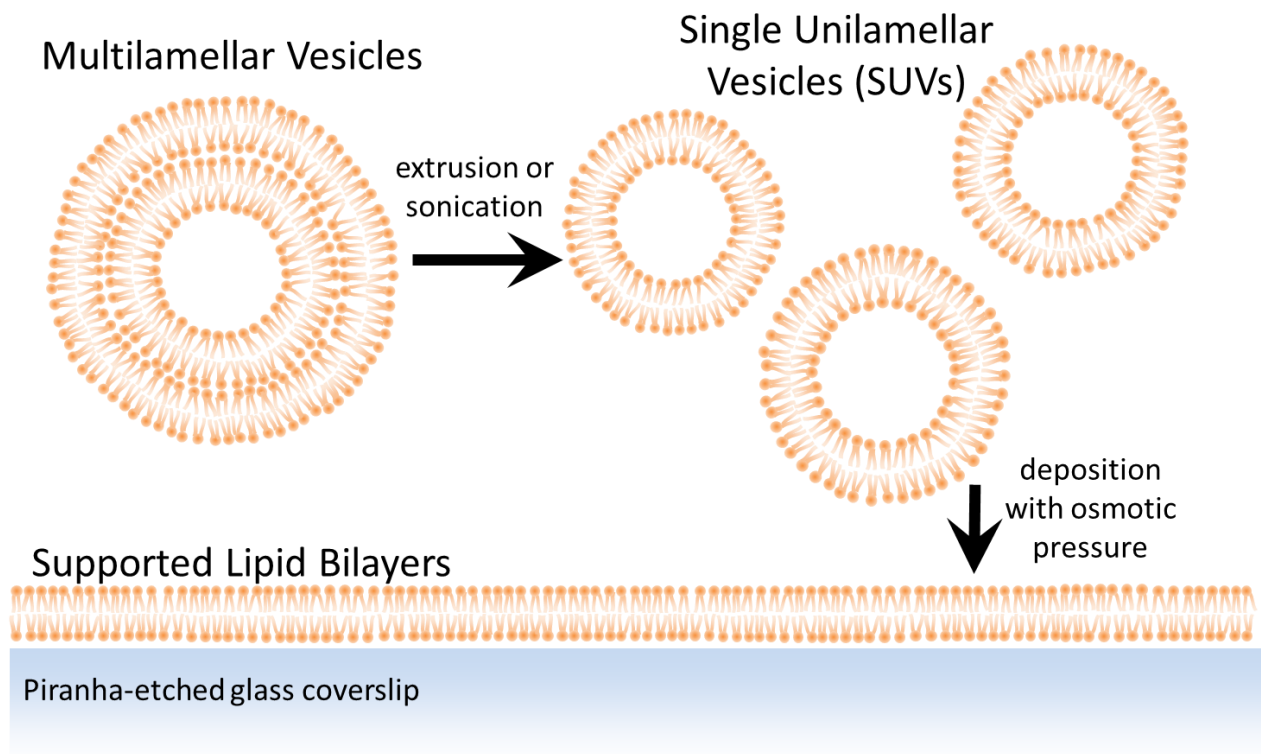
Figure 1.5. Fabricating in-vitro lipid structures.
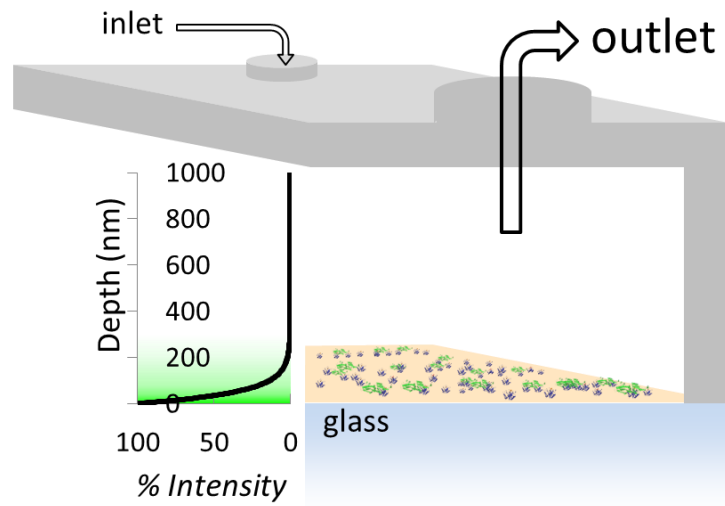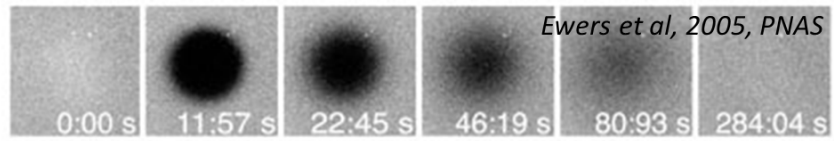
Figure 1.6. TIRF imaging in a flow cell.

CHAPTER 2.

MONITORING THE WAITING TIME SEQUENCE OF SINGLE RAS GTPASE ACTIVATION EVENTS USING LIPOSOME FUNCTIONALIZED ZERO-MODE WAVEGUIDES

Sune M. Christensen[§,†], Meredith G. Triplet[§], Christopher Rhodes[§,‡], Jeffrey S. Iwig[⊥,#], Hsiung-Lin Tu[§,Γ], Dimitrios Stamou[¶], Jay T. Groves [§,]*

§Department of Chemistry, University of California, Berkeley, CA 94720, USA.
⊥Howard Hughes Medical Institute, Department of Molecular and Cell Biology, University of California, Berkeley, CA 94720, USA.
¶Department of Chemistry and Nano-Science Center, University of Copenhagen, Copenhagen, Denmark

AUTHOR CONTRIBUTIONS

SMC and JTG conceived experiments. SMC and MGT performed experiments and analyzed data. CR, MGT and SMC prepared ZMW substrates. MGT and CR performed finite element simulations. SMC wrote software for data analysis. HLT assisted with experiment design and with SOS labeling. JSI purified proteins. SMC and JTG wrote the paper with assistance from MGT. All authors discussed and commented on the manuscript.

ACKNOWLEDGEMENTS

ABSTRACT

Activation of small GTPases of the Ras superfamily by guanine nucleotide exchange factors (GEFs) is a key step in numerous cell signaling processes. Unveiling the detailed molecular mechanisms of GEF-GTPase signaling interactions is of great importance due to their central roles in cell biology, including critical disease states, and their potential as therapeutic targets. Here we present an assay to monitor individual Ras activation events catalyzed by single molecules of the GEF Son of Sevenless (SOS) in the natural membrane environment. The assay employs zero-mode waveguide (ZMW) nanostructures containing a single Ras-functionalized liposome. The ZMWs facilitate highly localized excitation of fluorophores in the vicinity of the liposome membrane, allowing direct observation of individual Ras activation events as single SOS enzymes catalyze exchange of unlabeled nucleotides bound to Ras with fluorescently labeled nucleotides from solution. The system is compatible with continuous recording of long sequences of individual enzymatic turnover events over hour timescales. The single turnover waiting time sequence is a molecular footprint that details the temporal characteristics of the system. Data reported here reveal long-lived activity states that correspond to well-defined conformers of SOS at the membrane. Liposome functionalized ZMWs allow for studies of nucleotide exchange reactions at single GTPase resolution, providing a platform to gauge the mechanisms of these processes.

MAIN TEXT

Membrane-bound small GTPases of the Ras superfamily function as regulatory toggle switches in many signal transduction pathways and are implicated in a number of severe pathologies, including cancer[94–96]. GTPases shuttle between an inactive GDP-bound state and a GTP-bound state that promotes downstream signaling. Guanine nucleotide exchange factors (GEFs) activate their target GTPases by facilitating release of GDP from the nucleotide binding cleft, which is followed by uptake of a GTP nucleotide from the cell's cytosol. Activation of Ras by the GEF Son of Sevenless (SOS) relays signals from transmembrane receptors downstream to the mitogen-activated protein kinase (MAPK) cascade[64]. In the cell, Ras is anchored to the inner leaflet of the plasma membrane through palmitoyl and farnesyl moieties[65] whereas SOS resides in the cytosol and gets recruited to the membrane upon activation of transmembrane receptors[97,98]. At the membrane, SOS catalyzes the exchange of Ras-bound GDP with GTP, thus activating Ras and triggering downstream signaling[99,100]. Pathological mutations in Ras map to more than 30% of human cancers[96,101], whereas several mutations in Son of Sevenless (SOS) are implicated in the developmental disorders Noonan's[102,103] and CFC syndrome[104]. For this reason, extensive resources have been invested in developing inhibitors of Ras activation[105,106] and towards blocking the Ras-SOS interaction[107–109]. However, clinical success to this end has been limited. Shedding light on the molecular scale functional properties of Ras activation by SOS can provide insights into this problem, possibly exposing new pharmacalogical strategies.

Here we present a fluorescence microscopy assay that enables detection of single GEF-catalyzed Ras GTPase activation events reconstituted at a lipid membrane surface. Single turnover recording is the ultimate resolution limit in enzyme activity assays and has radically widened our view of enzyme kinetics, most prominently by uncovering the mechanistically important concept of memory effects[110–112], i.e., dynamic spontaneous fluctuations between distinct active conformers. In addition, studies of single enzyme turnover statistics have provided a means for inferring complex enzyme reaction landscapes that cannot be mapped from ensemble experiments[110,113]. Single turnover assays have been established for a number of enzyme classes (e.g. cholesterol oxidase[114], lysozyme[115] and metabolic lipases[111]), but at this stage no such method is available for the broad class of GEF-mediated activation of small GTPases, including Ras.

We recently reported that Ras binding to the allosteric pocket within the catalytic module of SOS (SOS^{Cat}) is sufficient for recruiting SOS to lipid bilayers in a sustained manner[38,116]. This finding enables isolation of single molecules of SOS using micropatterned supported lipid bilayers and subsequent assay of their time-averaged nucleotide exchange activity[116]. These studies revealed that Ras activation by SOS does not occur at a constant pace; SOS activity fluctuates between discrete long lived (up to minutes) activity states with lifetimes comparable to that of cellular signaling responses. A key insight from these experiments was that alteration of the activity fluctuation pattern of SOS has the capacity to alter the integrated output of an entire signaling pathway. Most importantly, this modulation exists in the time sequence of activity and is not detectable in the averaged behavior of SOS. However, due to the limited temporal resolution in the supported bilayer assay it is unclear whether fast (second scale) activity fluctuations are also present in the system or if the observed states correspond to discrete structures with well-defined catalytic rates. Here, by monitoring the time sequence of single GTPase activation events we show that there are no systematic rapid fluctuations in the kinetics of Ras activation by SOS, thus demonstrating the observed long lived activity states of SOS correspond to well-defined conformations of the enzyme at the membrane surface.

We reconstituted SOS mediated activation of membrane-coupled H-Ras (henceforth simply Ras) at the surface of liposomes that have been incorporated within arrays of zero-mode waveguides (ZMWs) (**Figure 2.1a**). ZMWs are nanoscopic apertures ($\varnothing$~100 nm) in thin metal films (**Figure 2.5**) that, upon illumination with light, produce a highly confined evanescent field with an effective focal volume in the atto- to zeptoliter range (10^{-18}-10^{-21} L)[117]. We exploit this property to minimize background signal from fluorescently labeled nucleotide analogs, distributed in solution and functioning as reporters of single Ras activation events (**Figure 2.1a**). The good match between the physical size of individual ZMWs and small unilamellar liposomes[69] facilitates stoichiometric 1:1 loading of these two components simply by incubation and spontaneous adsorption (**Figure 2.1b**).

The highly confined excitation volume inside a ZMW allows for single molecule imaging at μM concentration of fluorescently labeled reactants in solution, a concentration range relevant for

numerous protein-protein and protein-ligand interactions natively occurring in cells[118]. ZMW technology has enabled a number of single enzyme applications, including DNA sequencing by tracing of polymerase activity[119], real-time monitoring of protein translation by the ribosome[120] and probing the lifetime of protein-protein interactions in the GroEl-GroES chaperonin system[121]. A fundamental requirement in these experiments is that the enzyme of interest is tethered at the floor of the ZMWs, thus confining a single enzyme to a single waveguide. However, this strategy is incompatible with studying enzymes that either are embedded in, or functionally coupled, to lipid membranes. Our use of surface supported liposomes[70] as the reconstitution scaffold circumvents this issue. A crucial strength of this approach is that proteins and ligands bound to the liposome membrane retain lateral fluidity, and thus their ability to collide and react, while being confined to individual ZMWs. We note that continuous supported lipid bilayers can be formed on glass surfaces[122] and have previously been interfaced with arrays of ZMWs to study diffusion of membrane associated fluorescent molecules[123,124]. In those studies, however, proteins and ligands were not trapped within the ZMW and, as such, that configuration is incompatible with extended single molecule observation. While supported membranes could conceivably be formed in confined ZMWs in combination with membrane patterning methods[116,125,126] we chose to work with whole liposomes as a simpler approach. Liposomes have the additional advantage of accommodating transmembrane proteins, which are notoriously problematic in the supported membrane configuration[127].

The evanescent field inside a ZMW exhibits a non-trivial decay profile, which potentially could complicate observation of fluorescence from dyes diffusing at the membrane of immobilized liposomes. We performed finite element simulations of electromagnetic wave propagation in ZMWs[118] to illuminate this aspect (see Methods in the Supporting Information). **Figure 2.1c** shows the result of a simulation where a liposome (dashed line) was situated at the center of a ZMW. The excitation field intensity at the membrane varies with approximately a factor of two between the top and the bottom of the liposome (see also world map representation in **Figure 2.1d**). However, molecules at the membrane are not fixed but undergo Brownian motion in the course of a camera exposure at the microscope. A direct consequence is that fluorophores sample an ensemble of excitation intensities during each exposure. Indeed, for the imaging settings used in the reported work (≈20 ms per frame), we find that Brownian motion is sufficient to average out any experimentally relevant heterogeneity in the excitation field (see **Methods** and **Figure 2.6**). This is a critical feature, because it allows the detection of single fluorophore binding and bleaching events as, respectively, abrupt step increases and step decreases in fluorescence intensity.

We monitored successive single Ras activation events by observing SOS mediated exchange of unlabeled nucleotides bound to Ras with a fluorescent nucleotide analog (GTP-ATTO488) from solution (**Figure 2.1a**). Ras was chemically linked to the liposome bilayer via coupling of a C-terminal cysteine to maleimide functionalized lipids[38] (see **Methods**). Prior to immobilization, the Ras decorated liposomes were incubated with SOS, resulting in stable anchoring of SOS to the liposome upon binding of Ras to the allosteric pocket[116]. The liposomes serve as a vector for

20

docking the reactant complex in the ZMWs and provide an authentic membrane environment reminiscent of the native signaling platform of these enzymes.

The experimental design allows direct imaging of the location of ZMWs (bright field), liposomes (via a membrane marker), and SOS (labeled with a single dye molecule) (**Figure 2.1e)**. Experiments were run under conditions where each active liposome is likely to bind only a single molecule of SOS, which was confirmed by step-photobleaching of the SOS label (**Figure 2.1f)**. Control experiments in which fluorescent nucleotide is incubated on the same ZMW array before and after immobilization of Ras liposomes and, ultimately, in the presence of SOS verify that nucleotide exchange activity (observed as increased fluorescence intensity) is evident only in the presence of SOS (**Figure 2.1g** and **Figure 2.7)**.

Upon activation of single Ras proteins, the fluorescence intensity recorded from individual ZMWs exhibits an abrupt increase, followed by a plateau, and finally step photobleaching of the nucleotide label (**Figure 2.2a-b)**. Following bleaching, the fluorescence intensity remains at baseline level until the next Ras activation event, resulting in telegram-type sequence of activation events, as shown in **Figure 2.2b**. We fit entire hour-long trajectories, with hundreds of activation events, employing a change point algorithm and a set of level assignment criteria to sort the trace into "on" (corresponding to the scenario where a fluorescing nucleotide is bound to Ras at the liposome) and "off" (no fluorescing nucleotide bound) states (**Figure 2.2b**, see also **Methods)**. In this way, the waiting times between consecutive Ras activation events are extracted (**Figure 2.2b)**. The resulting single turnover waiting time sequence is a molecular footprint that details the temporal characteristics of the system comprised by a single SOS enzyme catalyzing Ras activation at a particular liposome.

Figure 2.3a and **Figure 2.3d** illustrate cumulated nucleotide exchange events as a function of time for a SOS^{Cat} (construct containing only the catalytic core of the protein, comprised by the CDC25 and REM domains) and a SOS^{DPC} enzyme (construct that, in addition to the catalytic core, has a DH-PH module). For each trace, the associated histogram of waiting times (respectively, **Figure 2.3b** and **Figure 2.3e)** and the autocorrelation function of the waiting times (respectively, **Figure 2.3c** and **Figure 2.3f)** are calculated. The SOS^{DPC} trace exhibits slightly longer average waiting times (corresponding to slower catalysis) which is in qualitative agreement with previous results showing that the domains N-terminal to the catalytic module of SOS dampens the nucleotide exchange activity[38,61,116] (**Figure 2.8)**. Under the conditions of these measurements, the observed nucleotide exchange kinetics in the ZMW were slower compared to our previous study with planar supported membranes[116] (see also **Figure 2.8)**. While this effect could conceivably be due to membrane curvature, other differences in the assay format, such as nucleotide concentration (10 µM in the ZMW vs. 120 µM in the planar supported bilayer measurements), cannot be ruled out. However, we do observe distinct features among the recorded traces indicating kinetics in the lipsome-ZMW system are not dominated by limited diffusion.

An enzyme working at a fixed catalytic rate (characteristic of a well-defined protein conformation) throughout a finite time interval exhibits no correlation between consecutive waiting times[110] (see also **Figure 2.9**). On the contrary, dynamic fluctuations in enzyme catalytic rate manifests as a non-zero autocorrelation function with a decay time characteristic to the timescale of the underlying fluctuations[110]. Extremely long timescale (e.g., hundreds to thousands of seconds) dynamic heterogeneity in the catalytic rate of Ras activation by SOS have been observed directly in single molecule membrane assays[116]. Those earlier studies, however, lack the temporal resolution to determine if faster dynamic heterogeneity exists, as would be expected if the structure of SOS on the membrane is very flexible, or if the long-lived activity states correspond to well-defined structures. Data reported in **Figure 2.3** exhibit no indication of systematic fluctuations in SOS activity on shorter timescales. Thus, we conclude that individual SOS catalytic states exist in well-defined conformations with highly regular catalytic cycles on the membrane. We did also observe the extremely long timescale state transitions[116], as illustrated by a trace from SOS^{DPC} with correlated waiting times at timescales of ≈1300 s. (**Figure 2.4a-b**).

We have introduced a liposome-interfaced ZMW assay employed here to measure time sequences of single Ras activation events catalyzed by SOS on a lipid membrane surface. This is, to the best of our knowledge, the first example of continuously resolving single GTPase activation kinetics mediated by an individual GEF enzyme. The assay principle with Ras and SOS can be readily generalized to study a multitude of biologically important GEF-GTPase signaling reactions at lipid membranes. We anticipate that studies of single GTPase activation kinetics will make important contributions toward deciphering the detailed molecular mechanisms of GEF-GTPase interactions. The introduced single molecule assay based on liposome-interfaced ZMW nanostructures enables experimental assessment of the fundamental kinetic properties of these critically important regulatory enzymes.

METHODS

Fabrication and functionalization of ZMWs for liposome immobilization
A #1 glass slide (Fisher Scientific) was pre-cleaned and plasma etched for 5 minutes. Thermal deposition of aluminum (99.9% purity Al pellet, Kurt J. Lesker Company) was achieved using an NRC evaporator and single-use tungsten baskets (Mathis Company, Long Beach, CA). During deposition, pressure was less than $5x10^{-6}$ Torr. Current was monitored manually to maintain a deposition rate of 0.1–0.2 nm/s. The total thickness was measured using a crystal monitor. Deposition was stopped by shutter when 75–100 nm total thickness was achieved.

Zero-Mode Waveguides (ZMWs) were etched into the aluminum surface with a FEI Quanta FIB. This instrument has a dual-beam SEM that was used to periodically assess quality of focus during fabrication. Alignment marks were etched on each substrate to optimize beam focus and

facilitate microscope localization of the area of interest. A mask with a 12x12 grid of 100 nm diameter circles and 2.5 µm pitch was used to pattern each substrate. Grids were arranged in groups of four for maximum imaging throughput (576 per field of view). To achieve a range of waveguide sizes, etching power and time were in the ranges of 50 pa-0.25 nA and 100–750 ms, respectively.

Prior to experimentation, the ZMW substrate was plasma etched for 30 s, mounted in a pre-cleaned teflon microscope chamber (custom made) and incubated for 30 min. with a 1:5 mixture of PLL(20)-g[3.5]-PEG2 : PLL(20)-g[3.5]-PEG2/PEG-(3.4)-Biotin(20%) (SuSoS, Dübendorf, Switzerland). The substrate was then washed copiously in buffer, incubated for 10 min. with 0.05 g/l Neutravidin (Sigma-Aldrich, St. Luis, MO) followed by another washing cycle.

Protein purification and labeling
SOS: SOS^{Cat} (residues 566-1049 with following mutations: C838A, C635A, C980S, E718C) and SOS-DPC (residues 198-1049) of human SOS1 were expressed in *E. Coli* and purified as previously described[38]. Labeling of SOS constructs with Atto647N-maleimide was carried out by reacting 1:10 molar ratio of purified protein with the dye for 2 hours at 23°C. Unreacted fluorophores were removed using PD-10 columns (GE Healthcare). Labeling efficiency was assessed by UV/Vis spectroscopy (NanoDrop 2000, Thermo Scientific) yielding; 90% for SOScat cyslite and 119% for DPC. The labeling efficiency larger than 100% for DPC is explained by the DPC construct harboring multiple cysteines.
Ras: H-Ras^{C118S,C181} (construct comprising residues 1-181 with a single cysteine at position C181 used for coupling to the liposome bilayer via MCC was expressed in *E. Coli* and purified as previously described[38].

Optical microscopy
Imaging was performed on an inverted microscope (Nikon Eclipse Ti (Ti HUBC/A), Technical Instruments, Burlingame, CA) equipped with a Nikon Apo TIRF 100x/1.49 oil objective. The microscope had a custom-built laser launch with 488 nm and 633 nm lasers (both from the OBIS product line, Coherent Inc. Santa Clara, CA) controlled via a laser control module (OBIS scientific remote). The 488 nm and 633 nm lasers were reflected to the specimen via dichroic mirrors and emission was collected in EPI mode. Emission signal was filtered using, respectively, ET525/50M and ET600/50 filters (Chroma, Bellows Falls, VT). Images were collected on an EM-CCD (iXon ultra 897, Andor Inc., South Windsor, CT) and the microscope was operated using micro-manager[128]. Bright field images to locate the position of ZMWs were acquired with a Nikon Intensilight C-HGFIE lamp.

Liposome preparation
All lipids were purchased from Avanti Polar Lipids, Alabaster, AL except BODIPY 500/510 C12-HPCm, which was from Life Technologies, Carlsbad, CA. Lipids were mixed in chloroform in a round-bottomed flask. The lipid composition was 88 mol% Egg-PC: 5% MCC-DOPE:5%

DOPS:1% 18:1 Biotinyl Cap PE: 1% BODIPY 500/510 C12-HPC (for SOS[cat] measurements) and 91mol% DOPC: 5.5% MCC-DOPE:1% DOPS: 1% 18:1 Biotinyl Cap PE: 1% BODIPY 500/510 C12-HPC: 0.5% PiP$_2$ (in experiments with SOS[DPC]). Chloroform was removed by 30 min. spinning on a rotary evaporator at 40 °C followed by at least 10 min. under nitrogen flow. Liposomes were formed by rehydrating the lipids in 20 mM HEPES [pH 7.0], 150 mM NaCl, 10 mM beta-mercaptoethanol. Liposomes were extruded in 3 consecutive runs using the LiposoFast mini-extruder (AVESTIN Inc., Ottawa, ON, Canada) equipped with 30 nm pore size filters (product number 800307, GE Healthcare). 365 µl vesicle suspension at 5 g/l lipid concentration was mixed with 50 µl Ras181 at 6 g/l. Coupling of the C-terminal cysteine of the Ras construct to the MCC headgroups on the liposomes was carried out at room temperature for 2.5 h. The resulting proteoliposome suspension was snap frozen using liquid nitrogen and stored at -80 °C.

Ras activation assay
All dilutions, washes and nucleotide exchange assays were done in 40 mM HEPES [pH 7.4], 5 mM MgCl$_2$, 100 mM NaCl, 1 mM TCEP. ZMW positions were located in bright field imaging mode. 10 µM EDA-ATTO488-GTP (Jena Bioscience, Gmbh) was added to the sample to check the signal in absence of nucleotide exchange activity and time-series were recorded at the different grid positions. The fluorescent nucleotide was then washed out of the chamber. Ras loaded liposomes at 5 g/l (see above) were reacted for 5 min. with 5 mM BME to quench any remaining reactivity of the MCC lipid head groups. Liposomes were then incubated with ≈300 nM SOS[DPC]-ATTO647N or 100 nM SOS[cat]-ATTO647N for 10 min. at room temperature and then stored at ice until injection on sample. In the absence of nucleotide, SOS gets stably recruited to the vesicles via allosteric Ras binding and locked with nucleotide-free Ras bound at the active site[99,116]. 10 µl of the SOS reacted liposomes were injected into a volume of 500 µl buffer in the ZMW mounted microscope chamber. Efficient loading of the ZMWs typically took on the order of 30 min. after which unbound vesicles and SOS were removed by washing.

A series of bright field images of the grids and corresponding EPI images were acquired to locate the liposome and SOS positions (from, respectively, BODIPY and ATTO647N fluorescence). The SOS label was then bleached by continuous illumination with high laser power (≈75 mW laser power incident on the objective) followed by bleaching of the liposome label. 10 µM EDA-ATTO488-GTP was added to the chamber to initiate the nucleotide exchange reaction and time-series were acquired at the different grids.

Fitting of single turnover traces
Data analysis was accomplished with a software suite written in Igor Pro (Wavemetrics, Lake Oswego, OR). Activity traces from single ZMWs were extracted from the time-series by integrating the intensity inside a region of interests (ROI). Prior to analysis traces were filtered to *(i)* remove baseline drift by subtracting from the trace a running average of the trace itself calculated using the "boxcar" smoothing algorithm in Igor Pro, with a box width of 1000 points (the width was chosen as to avoid distorting the step features in the traces) and *(ii)* reduce

24

random noise by subtracting a high pass filtered version of the trace from itself (conducted using the FilterFIR command in Igor Pro with the following flags /DIM=0/HI={0.2,0.3,101}).

Levels in the resulting traces were identified using the Bayesian change point detection algorithm developed by Ensing and Pande for Gaussian distributed data[5]. A Bayes factor of 3 was employed for level detection. The cumulative distribution of the identified intensity levels were then fitted with a double Gaussian and based on the fit a threshold was defined to categorize levels as belonging to either on or off states (see main text for definitions). The threshold was initially set to $I_h-(I_h-I_l)/4$, where I_h indicates the average of the higher intensity level and I_l the intensity of the lower intensity level. The threshold was then refined such that only a few events were detected in the control region of the traces. The change point algorithm for Gaussian distributed data is incapable of detecting levels with fewer than 4 data points and therefore an additional refinement of level identification was implemented. This was achieved by searching the assigned baseline regions for clusters of intensity values (defined as two or more consecutive points) that exceeded the local baseline with more than ¾ x ΔI, where $\Delta I = I_h-I_l$). Identified clusters were now tested for significance using the change point algorithm of Ensing and Pande derived for binomially distributed data[129]. In this case, for each baseline region a putative change point candidate was tested by artificially moving the given cluster of data to the end of that baseline region and testing for the presence of a change point at this location. A Bayes factor of 10^6 was employed as a criteria for acceptance. Finally, dwell times and waiting times were extracted based on the identified intensity levels.

Simulations of the excitation field inside a ZMW
Finite-element simulations using COMSOL Multiphysics' RF Module were used to model the excitation field inside a ZMW containing a liposome. The Electromagnetic Waves platform was used in 3D mode to model the excitation field. A free tetrahedral mesh was used with "Extra Fine" resolution and a refinement applied to the aluminum layer. Although only one waveguide was used for the bulk of the studies, a study was done to demonstrate that the spacing between waveguides is sufficient to isolate the excitation effects. A perfectly matched layer (PML) was incorporated in the borosilicate glass component to cancel any reflection artifacts from the simulation boundaries. The waveguide was simulated in a 100 nm layer of aluminum with refractive index (RI) as 0.77 and 5.9 for the real and imaginary part, respectively, as interpolated from literature tables[130]. A 488 nm wavelength of excitation was used from the bottom of the glass module, arriving perpendicular to the plane of the aluminum thin film.

The waveguide was modeled with a width of 100 nm and with a 10 nm over-etch into the glass, with the vesicle of 50 nm diameter centered at 10 nm up from the surface. Field simulations were conducted to demonstrate that over-etching reduced the effects of increased intensity at the bottom corners of the waveguide, and that minimal (but noticeable) effects were caused by altering the vesicle's location relative to the waveguide in the x,y, and z directions, and that more of the vesicle was more highly excited for wider waveguides. The vesicle was simulated as two

hollow shells with distinct RI values, with the outer layer mimicking Ras (RI 1.6 with imaginary component 10^{-9} [131] with 5 nm thickness) and the inner layer mimicking the lipid component as modeled by octane (RI 1.53 with imaginary component 10^{-9} [132] with 3.87 nm thickness[133], with the central region having the same values as the water-based buffer. Studies with varied RI demonstrated minimal sensitivity to small changes in the lipid or protein values, so these rough approximations were deemed acceptable. A diagonal cross-section of the 3D model was used to visualize the excitation dynamics within the waveguide, and a map was also formed of the excitation intensity at the outer surface of the vesicle.

Estimating the effective excitation flux impinging on fluorophores diffusing at the membrane of a ZMW immobilized liposome

Consider a liposome tethered at the center of a zero-mode waveguide (**Figure 2.1c**). From finite element simulations we have obtained a list of excitation field intensities at a set of discrete points on the liposome surface $I(x_i,y_i,z_i)$. In the experiments, we are integrating over a time bin of approximately 20 ms when imaging the fluorescence emission of dye molecules on the camera. Because dye molecules are free to diffuse at the liposome membrane they will experience a varying excitation field in the course of camera exposure. To estimate the effective excitation flux I_{Eff} experienced by a fluorophore started at height z with respect to the ZMW floor and diffusing in the course of a camera exposure we replaced each $I(x_i,y_i,z_i)$ with a weighted average over all other locations on the liposome surface as follows:

$$I_{Eff}(x,y,z) = S(x,y,z) \sum_i \frac{P(x,y,z,x_i,y_i,z_i)I(x_i,y_i,z_i)}{\rho(z_i)} \quad , \quad S = \left(\sum_i \frac{P(x,y,z,x_i,y_i,z_i)}{\rho(z_i)} \right)^{-1}$$
[eq. 1]

Here $\rho(z_i)$ denotes the density of discrete samples on the liposome surface at a given height from the ZMW surface (as defined by the simulation, due to symmetry we only consider the z component). S is a scaling factor that for a given point (x,y,z) was adjusted to comply with the normalization criterion at the right side of eq. 1. The sum runs over all discrete samples (x_i,y_i,z_i) of the excitation field. The sampling density $\rho(z_i)$ was estimated by fitting the simulated data with an exponential function yielding the (approximated) relation:

$$\rho(z_i)[\text{nm}^{-2}] = 0.248 + 7.922exp\left(-\frac{z - 0.00125}{0.00121}\right)$$
[eq. 2]

The weights $P(x,y,z,x_i,y_i,z_i)$ were calculated as the time-integrated probability density of finding a particle undergoing Brownian motion at a certain auxiliary point located a distance r away on the sphere surface (where r denotes the great circle distance between the point (x, y, z) and (x_i, y_i, z_i)):

$$P(r(x_i, y_i, z_i), t, D) = \int_{t_0}^{t_1} \frac{1}{4\pi Dt} exp\left(-\frac{r^2}{4Dt}\right) dt$$

[eq. 3]

t_0 was taken as 1 µs (to circumvent the discontinuity at t=0) and t_1=20 ms, the exposure time on the camera. The great circle distance, r, is a function of the point in consideration (given by the vector r_2 pointing from the center of the sphere, $C(x_c, y_c, z_c)$, to the given point on the liposome surface) and the auxiliary point (given by the vector r_2)):

$$\begin{aligned} r_1 &= \langle x - x_c, y - y_c, z - z_c \rangle \\ r_2 &= \langle x_i - x_c, y_i - y_c, z_i - z_c \rangle \\ r(x, y, z, x_i, y_i, z_i) &= R \ cos^{-1}\left(\frac{(x - x_c)(x_i - x_c) + (y - y_c)(y_i - y_c) + (z - z_c)(z_i - z_c)}{R^2}\right) \end{aligned}$$

[eq. 4]

Where R denotes the radius of the sphere. Combining equation 1-4 above yields the effective excitation field shown in Supporting Information **Figure 2.3** (t=20 ms). The solution was evaluated numerically.

The provided estimation is intended as a qualitative gauge for the order of magnitude of the diffusion effect. In this regard, it is important to note that we observe clear plateaus from single molecule signals in the traces, which is only expected if diffusion effectively cancels out the heterogeneity in the excitation field.

FIGURES
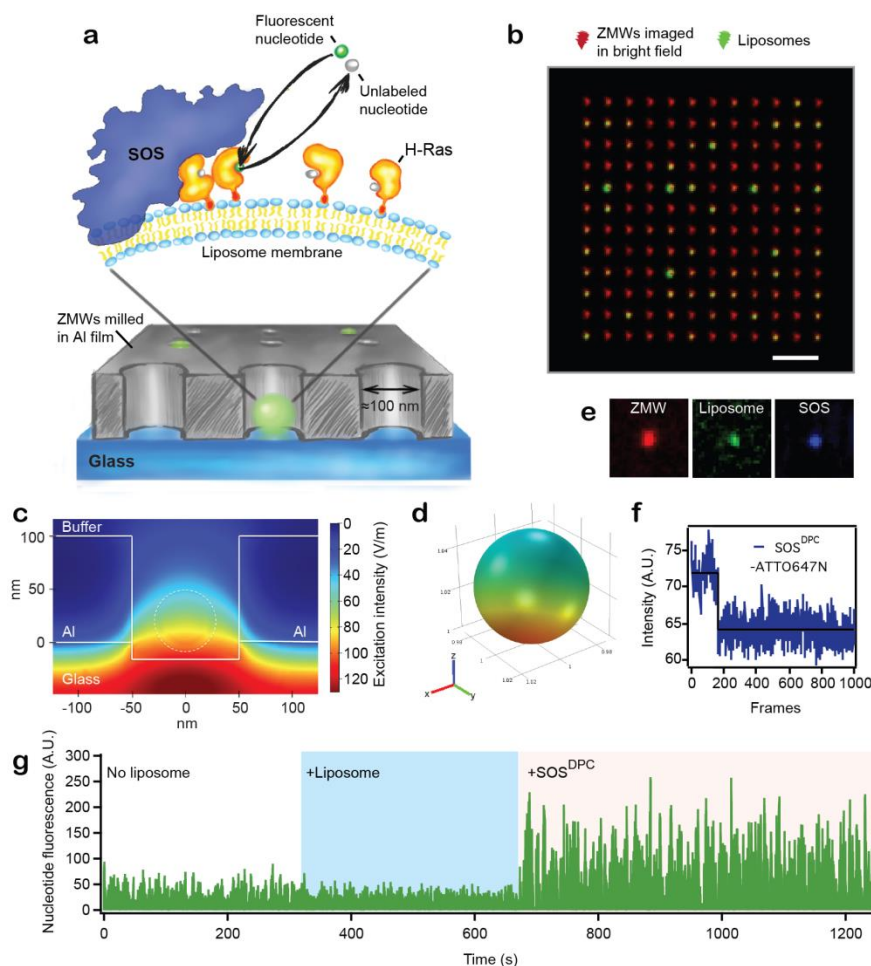
Figure 2.1. ZMWs functionalized with Ras-SOS decorated liposomes. (**a**) ZMWs with diameters of ~100 nm loaded with liposomes of compatible dimensions (average Ø ~30 nm, see Methods in the Supporting Information). H-Ras is chemically anchored via a lipid to the liposome surface. The liposomes also bear a single copy of the Ras-GEF SOS, which is stably associated with the lipid membrane via binding of Ras at an allosteric binding pocket. SOS catalyzed nucleotide exchange on Ras is observed by following the acquisition of fluorescently labeled GTP from solution. (**b**) Micrograph of a ZMW array (red, imaged in bright field) and colocalized liposomes (green, fluorescence image of membrane marker). (**c**) Simulation of the electromagnetic excitation field inside a ZMW with a liposome bound at the glass interface. Dashed line indicates the position of the liposome. (**d**) World map representation of the excitation field on the surface of the liposome. (**e**) Micrographs showing a ZMW and the associated liposome and SOS signal. (**f**) Bleaching of the SOS label (ATTO647N) in a single step signifies that the liposome harbors a single SOS molecule (trace corresponding to the micrographs in (e)). (**g**) Intensity trace of ATTO488-GTP from a single ZMW. The first part of the trace reflects the signal from a single ZMW without a Ras decorated liposome present. In the second part of the trace, a Ras loaded liposome was immobilized in the same ZMW. Finally, SOS was added from solution, resulting in apparent recruitment of fluorescent nucleotides (observed as a marked signal increase). The fluorescent nucleotide, ATTO488-GTP, was incubated at the ZMW grid at 10 µM. See also Supplementary Figure 3.

28
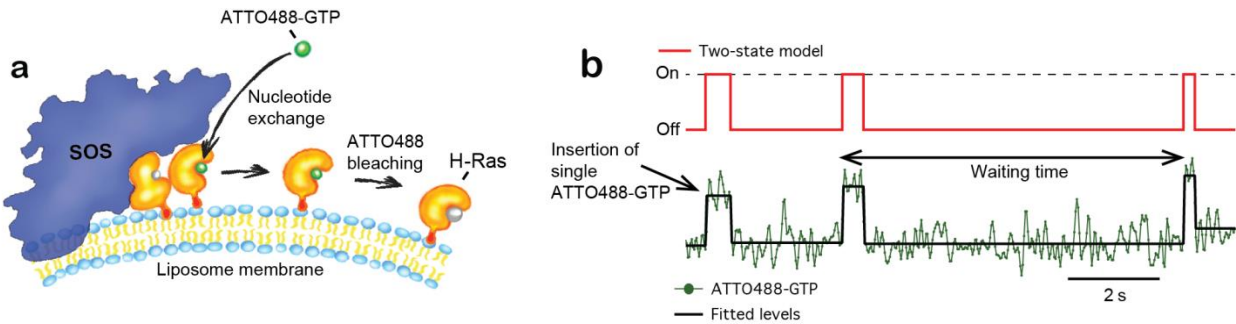
Figure 2.2. Single turnover recording of reconstituted Ras activation by SOS. (**a**) Assay principle: SOS exchanges unlabeled nucleotide on Ras for ATTO488-GTP. Shortly after binding of the nucleotide to Ras, ATTO488 bleaches and the fluorescence signal reverses to baseline before the next insertion event. This gives rise to telegram-like kinetic traces, where individual insertion events stand out as transient step increases of the fluorescence nucleotide signal. (**b**) Nucleotide exchange activity trace (green) showing single Ras activation events characteristic by abrupt step increases in ATTO488-GTP fluorescence intensity followed by single step bleaching of the nucleotide label. To quantify waiting times, steps were located using a change point detection algorithm (black trace) and then fitted to a two-state on/off model (red trace).

29
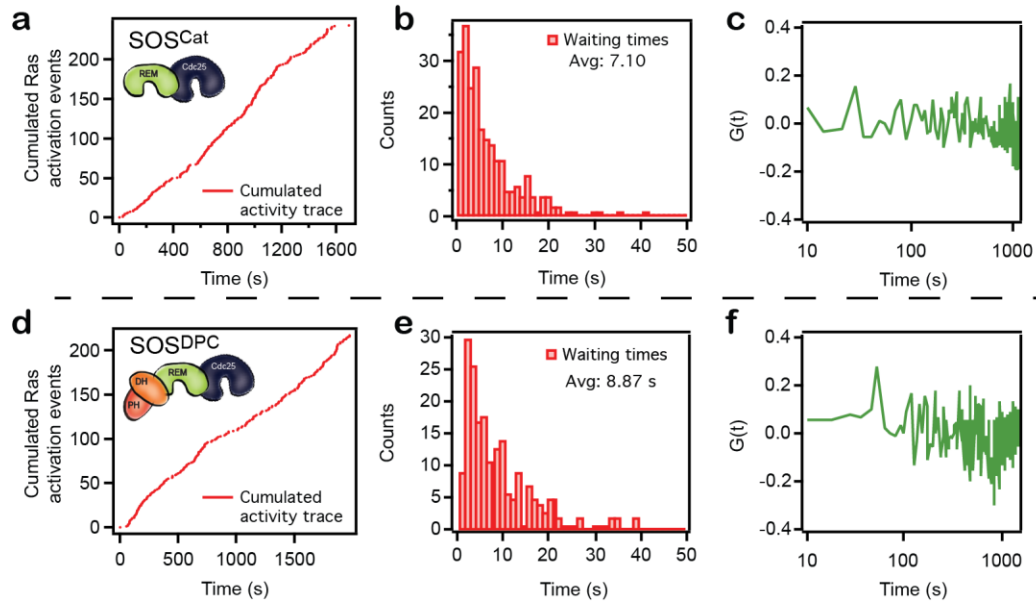
Figure 2.3. Single turnover analysis reveals that SOS catalytic states correspond to well-defined conformations of the enzyme. (**a**) Cumulated Ras activation events as a function of time for an activity trace acquired with the catalytic core of SOS (SOS^Cat). (**b**) Waiting time histogram corresponding to data in a. (**c**) Autocorrelation (G(t)=< $\Delta\tau(0)$ $\Delta\tau(m)$>/ <$\Delta\tau^2$>, $\Delta\tau(m)$= $\tau(m)$- <τ> [20]) of the waiting times corresponding to data shown in a. (**d-f**) Same data format as in a-c but for an activity trace acquired with SOS^DPC, a construct containing the N-terminal DH-PH domains of SOS in addition to the catalytic core. It should be noted that this type of data are intrinsically stochastic and therefore no two traces are the same. Importantly, the overall method is reproducible in its ability to capture these long sequences of Ras activation events.
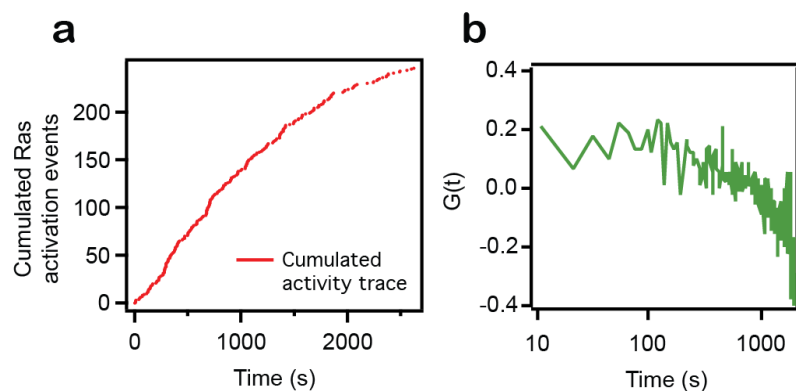
Figure 2.4. Evidence for long timescale state transition in SOS activity. (**a**) Cumulated Ras activation events as a function of time (trace acquired with SOS^{DPC}). Note the decreased turnover activity towards the end of the trace. (**b**) Normalized autocorrelation of waiting times for a SOS^{DPC} trace exhibiting a non-zero G(t), indicative of dynamically disordered enzymatic activity.
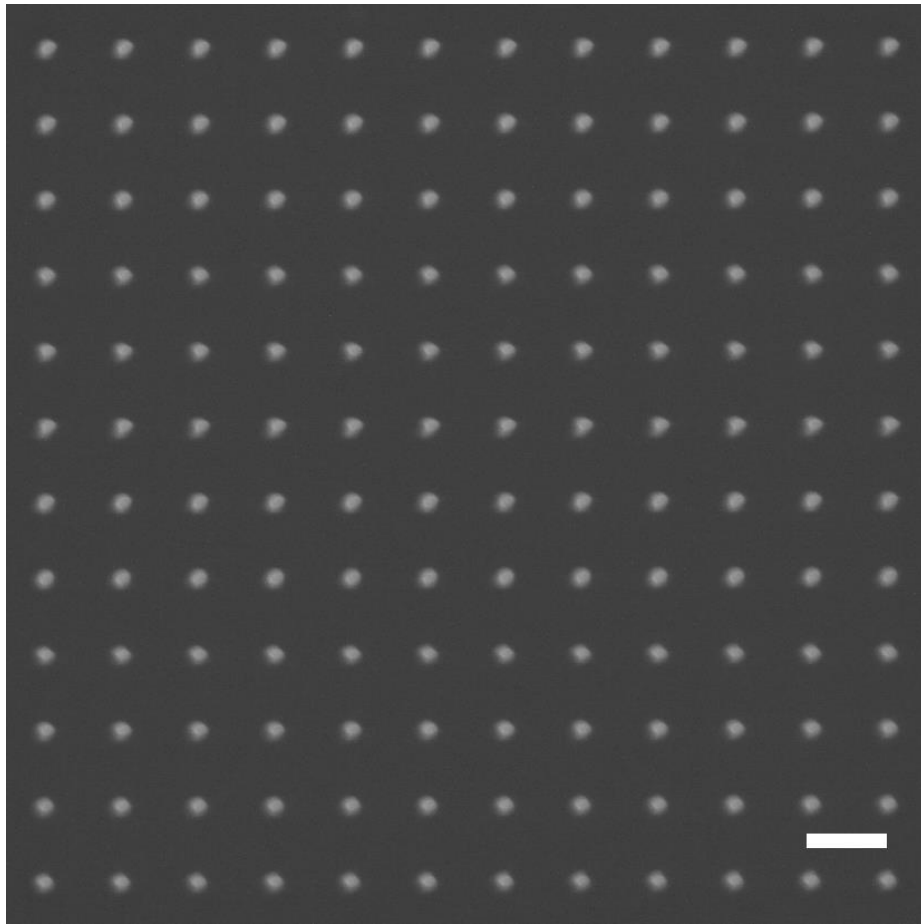
Figure 2.5. SEM image of ZMW grid. Bar: 2.5 µm.
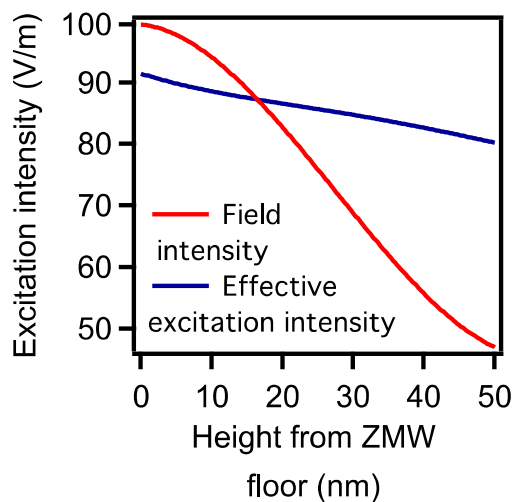
Figure 2.6. Brownian diffusion balances the effect of a heterogeneous excitation field over the liposome membrane. Red trace shows the excitation field at the liposome membrane at a given height from the ZMW floor. Blue trace shows the estimated effective excitation field experienced by a fluorophore diffusing at the membrane with diffusion coefficient of 1 μm^2/s during a camera exposure of 20 ms, when started at the membrane at a given height from the ZMW floor. See the methods for details on the calculation.
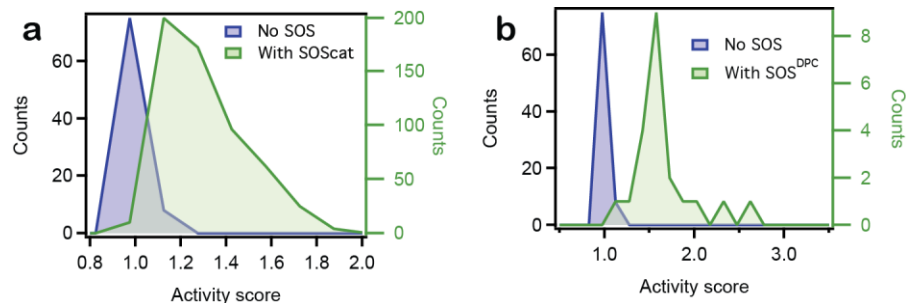
Figure 2.7. Nucleotide exchange activity is specific to the presence of SOS. Histograms of activity scores recorded from arrays of ZMWs with immobilized liposomes, with and without SOS (liposomes were incubated with elevated levels of SOS in order to bind SOS on all liposomes). The activity score was defined as follows: standard deviation of baseline subtracted trace (see Methods) from single ZMW in the presence of SOS divided by the standard deviation of background subtracted trace from the same ZMW in the absence of SOS. Increased fluctuation in a baseline subtracted trace upon addition of SOS corresponds to increased nucleotide exchange activity, thus resulting in an increased activity score. In (**a**) liposomes were present both before and after adding SOS. In (**b**) the no SOS part of the traces used to obtain the activity score was acquired without liposomes present (i.e., simply incubating labeled nucleotide on a ZMW array). The "With SOS" histograms in (a) and (b) comprise data from one sample each. The "No SOS" reference histogram is the same for the two panels and was obtained by comparing traces from ZMWs before and after immobilization of liposomes in the absence of SOS (see Figure 1g). The total counts for each histogram is as follows: "No SOS" (N=83), "With SOScat" (N=568) and "With SOS^{DPC}" (N=21).
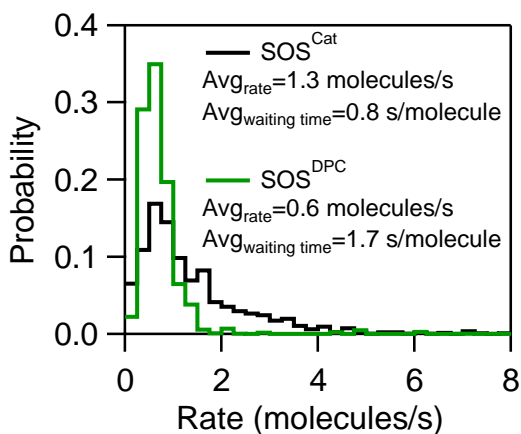
Figure 2.8. Single SOS nucleotide exchange activity rate distributions for SOS^{Cat} and SOS^{DPC} recorded on supported lipid bilayers. Histogram of single SOS activity states for SOS^{Cat} and SOS^{DPC} obtained using micro-patterned supported lipid bilayers, as described in Iversen et al., *Science* **2014,** 345, (6192), 50-4. Average turnover rates and corresponding waiting times (calculated from the measured average rates) are indicated in the legend. The histogram for SOS^{DPC} comprise data from 4 supported lipid bilayer samples whereas the histogram for SOS^{Cat} comprise data from 5 samples.
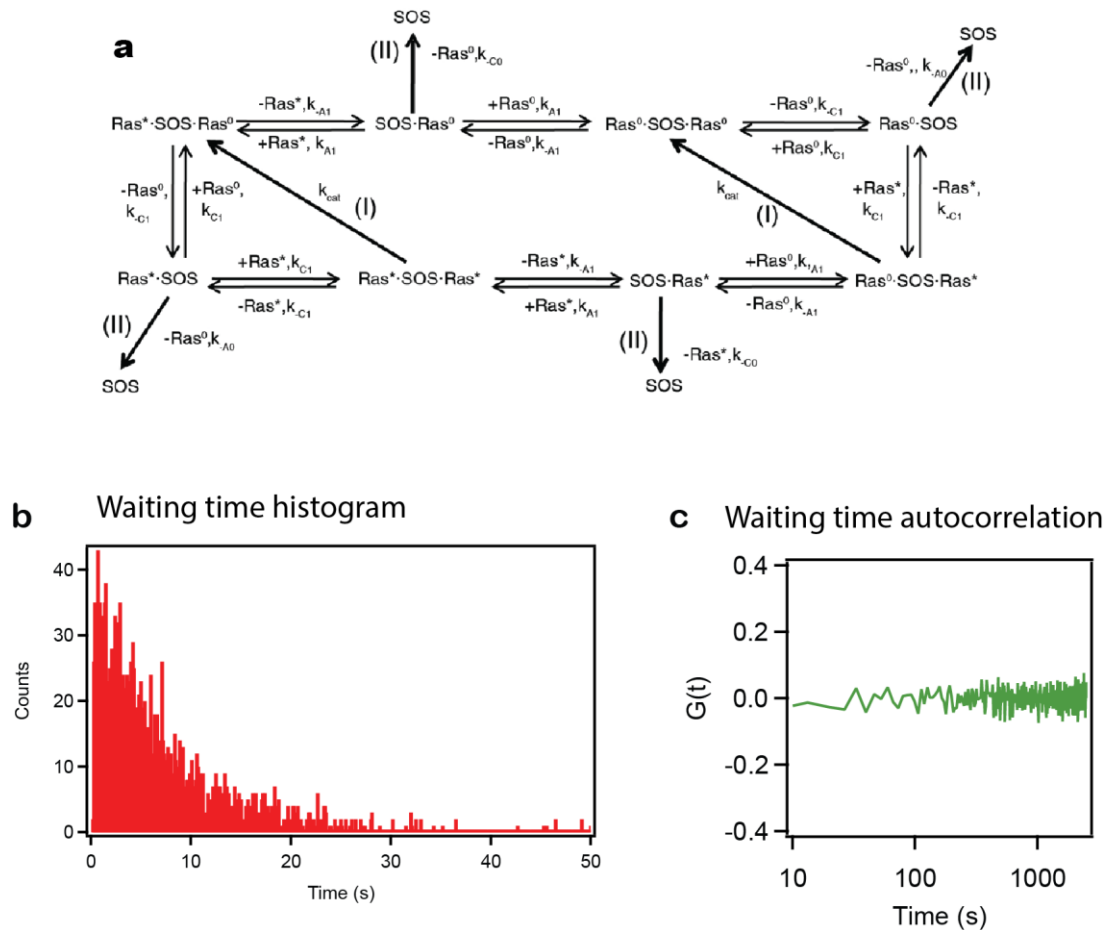
Figure 2.9. Stochastic simulations of SOS catalyzed nucleotide exchange. **(a)** Reaction network for a single-state SOS molecule (i.e., working at a fixed catalytic rate) turning over Ras. Ras·SOS indicates Ras bound in the allosteric site, SOS·Ras indicates Ras bound in the catalytic site, and Ras·SOS·Ras indicates Ras in both allosteric and catalytic sites. Ras* represents a Ras loaded with fluorescent nucleotide whereas Ras0 is a Ras with non-fluorescent nucleotide. Channel (I) leads to a nucleotide exchange reaction and channel (II) describes the case where a SOS unbinds from the surface. The reaction model is adapted from Iversen et al., *Science* **2014,** 345, (6192), 50-4 **(b)** Waiting time data from a stochastic simulation based on the reaction network in a. Simulation condition: Time steps of 0.06 ms for 15,000 seconds. kcat=0.16, Ras density 4,000 molecules/μm^2. **(c)** Autocorrelation function for the waiting time list histogrammed in b. As expected for a SOS enzyme catalyzing nucleotide exchange at a fixed catalytic rate, G(t) indicates that subsequent waiting times are entirely uncorrelated. The simulation was performed using the simulation procedure reported in Iversen et al., *Science* **2014,** 345, (6192), 50-4. The simulation was repeated twice.

CHAPTER 3.

ONE-WAY MEMBRANE TRAFFICKING OF SOS IN RECEPTOR-TRIGGERED RAS ACTIVATION

Sune M. Christensen[1,†,§], Hsiung-Lin Tu[1,†,‡], Jesse E. Jun[2,†], Steven Alvarez[1], Meredith G. Triplet[1], Jeffrey S. Iwig[3], Kamlesh K. Yadav[4,¶], Dafna Bar-Sagi[4], Jeroen P. Roose[2,#,], Jay T. Groves[1,#,*]*

[1]Department of Chemistry, University of California, Berkeley, California, USA.
[2]Department of Anatomy, University of California, San Francisco, California, USA.
[3]Howard Hughes Medical Institute, Department of Molecular and Cell Biology, University of California, Berkeley, California, USA.
[4] Department of Biochemistry, New York University School of Medicine, New York, USA.
† These authors contributed equally to this work.
# These authors jointly supervised this work.

AUTHOR CONTRIBUTIONS

S.M.C., H.L.T., J.E.J. performed experiments and analyzed data. S.A., M.G.T. assisted with live-cell experiments. J.S.I. purified proteins. K.K.Y. performed COS1 cell experiments under supervision of D.B.-S. J.T.G., J.P.R., S.M.C., H.L.T., and J.E.J. conceptualized and designed experiments. S.M.C., H.L.T., J.E.J., J.P.R. & J.T.G. wrote the paper. J.T.G., J.P.R. supervised the project. All authors discussed and commented on the results.

ACKNOWLEDGMENTS

ABSTRACT

SOS is a key activator of the small GTPase Ras. In cells, SOS-Ras signaling is thought to be initiated predominantly by membrane-recruitment of SOS via the adaptor Grb2 and balanced by rapidly reversible Grb2:SOS binding kinetics. However, SOS has multiple protein and lipid interactions that provide linkage to the membrane. In reconstituted-membrane experiments, these Grb2-independent interactions are sufficient to retain SOS on the membrane for many minutes, during which a single SOS molecule could processively activate thousands of Ras molecules. These observations raised questions concerning how receptors maintain control of SOS in cells and how membrane-recruited SOS is ultimately released. We addressed these questions in quantitative assays of reconstituted SOS-deficient chicken B cell signaling systems combined with single-molecule measurements in supported membranes. These studies reveal an essentially one-way trafficking process in which membrane-recruited SOS remains trapped on the membrane and continuously activates Ras until being actively removed via endocytosis.

INTRODUCTION

Ras is a membrane-anchored small GTPase that plays a central role in many signaling pathways. Ras can exist in an inactive (GDP-bound) or active (GTP-bound) state. Ras activation is mediated by a variety of Ras guanine-nucleotide-exchange factors (RasGEFs) that catalyze the exchange of Ras-bound nucleotide with cytoplasmic GTP[101,135,136]. This process is opposed by Ras-GTPase-activating proteins (RasGAPs) that enhance the intrinsic GTPase activity of Ras and thus promote Ras deactivation[135]. Ras activation must be tightly regulated; aberrant activation of Ras is responsible for many human cancers[106].

Son of Sevenless (SOS) is a widely distributed RasGEF[97,100,137] whose full activation through an allosteric mechanism results in digital (i.e., bimodal) patterns of receptor-induced Ras kinase signaling[59,138]. The activation of Ras by SOS is critical for diverse processes such as cell growth[139], T-cell activation and development[59,138,140,141], early B-cell development[142], embryogenesis[143], and differentiation of embryonic stem cells[144].

Receptor-triggered activation of SOS is a multilayered process involving membrane recruitment, release of autoinhibition, and allosteric modulation by Ras. The initial membrane recruitment of SOS is thought to occur via association of PxxP motifs in the C-terminal proline-rich (PR) domain with Grb2, which in turn binds phospho-tyrosine motifs on activated receptors or transmembrane adaptor proteins[100,137,139,145–150]. SOS additionally contains a series of N-terminal domains with homology to Dbl (DH) and pleckstrin (PH) as well as a histone-fold (HF) domain (**Fig. 1a**), which autoinhibits SOS activity when assayed in solution. On membranes, this autoinhibition is released through interactions with various membrane lipids[38,61,151] (reviewed in ref. [138]). Full activation of SOS is contingent on binding of Ras to an allosteric pocket situated at the rim of the REM and CDC25 domains[152]. The REM and CDC25 domains in SOS1 together

38

form the catalytic core, which we denote SOS^{Cat} herein (**Fig. 3.1a**). Mutations in SOS1 that perturb these regulatory functions result in altered signaling behavior and have been implicated in developmental disorders such as Noonan[103], Costello, and CFC syndromes[104]. SOS2 has a very similar domain makeup but appears to be somewhat redundant with SOS1 in cells[142]; in this study, we focused solely on SOS1.

Historically, SOS activation has been rationalized in terms of a simple membrane-recruitment model based on substrate accessibility (**Fig. 3.1b**). Grb2 binding to activated receptors recruits the SOS–Grb2 complex from the cytosol, thereby positioning SOS in proximity to membrane-anchored Ras and consequently promoting nucleotide exchange[97,153]. However, the importance of Grb2-mediated membrane recruitment is challenged by observations that truncated SOS constructs lacking the PR domain still localize to the membrane after receptor stimulation and are fully signaling competent or even exhibit increased responsiveness compared with that of the full-length enzyme[154–159]. Recent work with mouse embryonic stem cells[144] has demonstrated that, beyond Grb2-facilitated membrane recruitment, SOS activity is governed by a combination of weak-to-moderate protein-protein and protein-lipid interactions mediated by the multiple domains of SOS[144,151,158,160]. These studies suggest that the recruitment to membrane integral receptors via Grb2 is an oversimplified model for SOS function (**Supplementary Note 1**). We observed that SOS constructs lacking the Grb2-binding PR domain are successfully recruited to reconstituted Ras-functionalized membranes through Ras- and lipid-binding interactions. Additionally, using a micropatterned fluid supported-lipid-bilayer platform[125,126] in which the catalytic activity of individual SOS molecules can be directly resolved[116], we found that a single SOS molecule has the capacity to processively activate thousands of Ras proteins during a single membrane residency period (**Fig. 3.1c,d**). Such high degrees of processivity and essentially irreversible membrane recruitment in the activation of Ras by SOS have not been captured in earlier mechanistic and computational models of SOS activity, or in synthetic-biology approaches using Grb2-SOS1 fusion proteins[59,144].

Does such extreme processivity of SOS occur in cells, and, if so, how it is regulated? To address this question, we mapped the individual contributions of the different domains of SOS1 to membrane association, through a series of single-molecule dwell-time measurements and bulk kinetic observations. These studies used a reconstituted-membrane system in combination with quantitative cell-based signaling assays (details in **Supplementary Note 1**). Altogether, our results reveal an essentially one-way trafficking process in which membrane-recruited SOS1 remains trapped on the membrane and continuously activates Ras until being actively removed, such as by endocytosis. This mechanism differs substantially from the reversible Grb2-dependent process that has been generally assumed[100,137,139,145–148]. The Ras-activation machinery may remain active or be inactivated regardless of the triggering state of the receptor that initiated the signal; this phenomenon substantially affects the quantitative input-response function for Ras activation by receptor triggering and underscores the importance of strong inhibition of spontaneous SOS activation.

RESULTS

Supported-lipid-bilayer SOS-activation assay

We developed an imaging assay to study the interaction of SOS with Ras on supported lipid bilayers (SLBs; **Fig. 3.2a**). In this experimental configuration, we coupled H-Ras (residues 1–181, C118S mutant, henceforth referred to as Ras) to the bilayer at C181 via a maleimide-functionalized lipid (Online Methods), thus yielding permanently bound and laterally mobile Ras that was fully functional with respect to SOS activity[38,116,161] (**Supplementary Fig. 3.1a**). A calibration curve obtained with fluorescence correlation spectroscopy provided access to the local surface density of Ras via epifluorescence imaging of Ras-bound fluorescent nucleotide labels (GDP- and GTP-BODIPY; **Supplementary Fig. 1b** and ref. [116]). Labeling of SOS with a photostable and bright fluorophore (ATTO 647N) facilitated reliable counting and tracking of individual SOS molecules at the membrane surface by total internal reflection fluorescence microscopy (TIRFM). Control experiments showed that labeling did not perturb the observed activity of SOS (**Supplementary Fig. 3.1c**).

In this system, we initiated measurements by flowing purified SOS1 over the Ras-functionalized SLBs in a transient pulse with a defined concentration profile (**Fig. 3.2a**). During such a pulse, SOS1 interacts with membrane-bound Ras and, in the absence of free nucleotide in solution, becomes trapped after binding Ras at the catalytic site[99,155]. This method provided a convenient means of quantifying the probability of SOS1 engaging Ras by directly counting the number of SOS1 molecules remaining at the bilayer after a pulse (**Fig. 3.2b** and Online Methods). Chasing with unlabeled nucleotide initiated the exchange reaction and resulted in processive (i.e., sustained) turnover of Ras by the recruited and successfully activated SOS1 molecules (**Fig. 3.2a** and **Supplementary Fig. 1d**). A constant flow during the experiment ensured that dissociated SOS1 was removed from the reaction chamber, thus permitting measurement of the desorption kinetics.

Allosteric activation of SOS via altered membrane recruitment

An important functional aspect of SOS1 in the cellular context is its activation by RasGTP binding to an allosteric site, located between the CDC25 and Ras-exchanger motif (REM) domains in the catalytic core, termed SOS^{Cat} (ref. [152]). This allosteric activation sensitively depends on the nucleotide state of Ras[162] and is thought to enable a RasGTP positive feedback loop operating at the membrane[59,138].

Allosteric binding of Ras by SOS also provides an alternate mechanism to recruit SOS to the membrane. Here, we first quantitatively analyzed recruitment by examining the SOSCat module, which contains both the active site and the allosteric Ras-binding pocket but lacks any lipid-binding domains[152]. SOS^{Cat} was recruited to the Ras bilayer during the pulse phase of the assay (**Fig. 3.2c**). The known concentration profile of SOS^{Cat} during the pulse, combined with locally measured Ras densities, permitted quantification of the recruitment probability from the

adsorption traces (i.e., the probability of a SOS$^{\text{Cat}}$ molecule being trapped after collision with Ras at the membrane (**Fig. 3.2d** and Online Methods)).

We found that membrane recruitment of SOS$^{\text{Cat}}$ was sensitive to the nucleotide state of Ras, observing an ~16-fold enhancement on SLBs displaying RasGTP (**Fig. 3.2d**). A Y64A point mutation in Ras, previously shown to abolish Ras binding to the catalytic site of SOS[163], resulted in only transient recruitment of SOS$^{\text{Cat}}$, thus demonstrating that, as expected, SOS is trapped at the membrane after binding Ras at the catalytic site in the absence of free nucleotide (**Fig. 3.2c**). Nucleotide-dependent recruitment was preserved for RasY64A, thus indicating that the allosteric binding pocket is the primary determinant of this property of SOS$^{\text{Cat}}$ (**Fig. 3.2d**). A W729E point mutation in SOS1, known to prevent binding of allosteric Ras[59,164], essentially abrogated recruitment (**Fig. 3.2c,d**). After chasing with nucleotide, a population of highly processive SOS$^{\text{Cat}}$ remained at the membrane (tail of the curve in **Fig. 3.2c**), which we identified as successfully activated SOS$^{\text{Cat}}$ molecules. The long-lived (minute-to-hour scale) membrane-bound SOS$^{\text{Cat}}$ was catalytically active (**Supplementary Fig. 1d** and ref. [116]), thus indicating that release of SOS from the membrane was predominantly limited by the allosterically bound Ras.

We substantiated our findings in the SLB experiments with cellular assays (**Supplementary Note 2** and **Supplementary Fig. 2a–d**). Collectively, the data demonstrated a distinct positive allosteric effect of RasGTP at the stage of membrane recruitment. These results, together with the insensitivity of the average specific activity of SOS to the nucleotide state of Ras[116], indicated that RasGTP-mediated recruitment of SOS via its allosteric site is one mechanism by which the well-known accelerating effect of RasGTP on SOS mediated Ras activation is achieved (commonly referred to as positive feedback)[38,59,162].

Regulation of membrane binding by N-terminal domains
It is not known whether membrane recruitment and retention of SOS$^{\text{Cat}}$ are influenced by its flanking lipid-binding domains. At the N-terminal side, the catalytic core of SOS1 is flanked by a DH-PH cassette and an HF domain (**Fig. 3.3a**). Structural and biochemical studies have shown that the N-terminal domains exert an autoinhibitory effect on SOS1 activity, presumably through steric obstruction of the allosteric Ras-binding pocket, as observed in crystal structures[61,164]. The PH domain interacts with phosphatidylinositol 4,5-bisphosphate (PIP2) lipids[160,165] and phosphatidic acid[158], and the HF domain contains several additional interaction sites for negatively charged lipids[61,151]. These lipid interactions are generally believed to play a role in the release of autoinhibition, but the underlying mechanisms are unclear.

We observed a pronounced damping effect on initial membrane recruitment of SOS1 after adding the N-terminal domains to SOS$^{\text{Cat}}$. Appending the DH-PH unit to the catalytic core (SOS$^{\text{DPC}}$) reduced recruitment to the membrane by approximately three-fold. Inclusion of the full N terminus (construct comprising HF-DH-PH-Cat domains (SOS$^{\text{HDPC}}$)) damped recruitment by ~66-fold relative to that of SOS$^{\text{Cat}}$ (**Fig. 3.3b**). Even in the case of the highly autoinhibited

HDPC construct, Ras-specific binding was evident (**Supplementary Fig. 2e**). These observations clearly demonstrated that a major property of the N terminus is the down-modulation of spontaneous SOS1 activation by hindering its initial recruitment to the membrane, as evidenced by the steric hindrance of the allosteric Ras-binding site observed in structures[61,164]. Interestingly, a gain-of-function R552G point mutation associated with Noonan syndrome (SOS^{HDPC}R552)[100], compared with SOS^{HDPC}, caused a slight relief of such inhibition (**Fig. 3.3b** and Supplementary **Fig. 3.3a**), thus emphasizing the importance of a tightly regulated membrane recruitment step. As observed for SOS^{Cat} (**Fig. 3.2c,d**), the longer constructs also exhibited increased recruitment on bilayers displaying RasGTP (**Supplementary Fig. 3a**).

Although the N-terminal domains inhibited initial recruitment, SOS^{DPC} and SOS^{HDPC} exhibited extremely long dwell times on Ras-functionalized bilayers (with a mean residency period on the hour scale; **Fig. 3.3c**, **Supplementary Fig. 3b,c** and Online Methods). The N-terminal domains thus mediate two major functions: inhibition of the initial recruitment probability and enhancement of the dwell time in the active membrane-bound state. This anticorrelation between membrane recruitment probability and dwell time gives rise to an interesting dual functionality in which rare activation events are coupled to a potent response (**Supplementary Fig. 3d,e**).

Multicomponent analysis of SOS-Ras-ERK signaling
To establish the effects of intrinsic chemical SOS1 properties—as determined from reconstituted-SLB assays—on cellular SOS1-Ras signaling, we optimized a SOS1- and SOS2-double-deficient (SOS1−2−) DT40 chicken B-cell system that we have previously used to characterize digital SOS1-Ras-MAPK ERK signal transduction after B-cell receptor (BCR) ligation[59,98,166]. Here, we introduced EGFP-tagged variants of human SOS1 (hSOS1) into these cells entirely devoid of endogenous SOS1 and SOS2, left the cells unstimulated or induced BCR ligation, and monitored EGFP-SOS localization by fluorescence microscopy or activation of the ERK kinase by using an antibody to phospho-ERK (pERK) and flow cytometry[59,98] (**Fig. 3.4a,b**). The latter experimental platform, henceforth denoted the p-FLOW assay (Online Methods), revealed the quantitative magnitudes of Ras-ERK responses at the individual-cell level along with SOS1 expression levels. We depicted 3D representations of the data by mapping the time evolution of pERK after BCR stimulation as a function of SOS1 expression level (**Fig. 3.4c,d**). pERK traces corresponding to specific SOS1 levels represent 2D slices through the data (**Fig. 3.4f,g,i,j**).

Timely signaling requires SOS^{Cat}-flanking domains
Transient transfection of EGFP-tagged full-length human SOS1 (SOS^{FL}) rescued the characteristic BCR-induced pERK patterns in SOS-deficient DT40 cells (**Fig. 3.4b** and **Supplementary Fig. 4a,b**). SOS^{Cat}, lacking the Grb2-binding domain as well as the N-terminal lipid-interacting domains, triggered Ras-ERK signaling patterns that differed substantially from those triggered by SOS^{FL} (**Fig. 3.4c,d** and **Supplementary Fig. 4c,d**). Cells expressing high levels of SOS^{Cat}, compared with cells expressing SOS^{FL}, exhibited more spontaneous activation

of ERK in the absence of receptor stimulation (**Fig. 3.4e,h**). Even under these conditions, BCR stimulation further increased ERK activation in SOS^{Cat}-containing cells (**Fig. 3.4c,f,i**). Another notable difference was the signal attenuation. Whereas SOS^{FL}-induced pERK signals decreased at later time points after BCR stimulation (10–20 min.), SOSCat continued to signal in a sustained manner, and SOS^{Cat} outperformed SOSFL (**Fig. 3.4f,i**). The sustained signaling from SOS^{Cat} cells suggests that the essentially irreversible membrane anchoring of SOS^{Cat} observed in reconstituted assays may exist in cells as well, but not for SOS^{FL}.

Domains flanking SOS^{Cat} might initially appear to merely dampen signal output. However, selective examination of cells expressing intermediate SOS levels revealed that SOS$_{FL}$ signaled more efficiently than SOS^{Cat} in response to BCR stimulation (**Fig. 3.4g,j**). Moreover, this intermediate SOS^{FL} level resulted in rescued pERK responses that were nearly identical to those observed for wild-type DT40 cells, thus suggesting that reconstitution with intermediate hSOS1 levels matches the physiological level expressed in wild-type DT40 cells (**Supplementary Fig. 4b**). The data revealed that domains flanking SOS^{Cat} have both positive and negative regulatory roles.

SOS autoinhibition prevents spontaneous activation
A number of structural and cellular studies have established regulatory mechanisms that affect SOS1 activity, but several proposed mechanisms appear to be contradictory[38,61,151,164]. To understand how SOS1 restricts spontaneous signaling in cells yet allows for controlled allosteric activation near the membrane interface, we first focused on SOS^{Cat} flanking domains in the basal state (**Fig. 3.5a–c**), i.e., in resting cells[100,137].

Addition of N-terminal domains to SOS^{Cat} blocked the spontaneous activation of Ras-ERK in cells expressing high levels of SOS (**Fig. 3.5a,b** and **Supplementary Fig. 5a–d**). The inhibitory potential scaled in an incremental manner with the number of domains flanking the catalytic core; i.e., SOS^{DPC} signaling was more restrained than SOS^{Cat} signaling (**Fig. 3.5a**), and SOS^{HDPC} was more inhibited than SOS^{DPC} (**Fig. 3.5b**). These results corroborate the SLB results in **Figure 3.3b**. Structural and biochemical studies on SOS1 demonstrated that the DH domain limits Ras binding at the allosteric pocket, and without removal of DH-mediated autoinhibition and allosteric activation, the catalytic pocket cannot fully accommodate RasGDP or dislodge GDP from Ras[38,164]. The HF strengthens SOS autoinhibition by blocking allosteric activation and by stabilizing a closed conformation of SOS[61,167]. These structural findings are consistent with our p-FLOW results for the resting cell state (**Fig. 3.5a–c**). Notably, despite considerable effort, it has not been feasible to purify functional full-length SOS1 including the PR domain, thus preventing its examination in our earlier SLB assays[116].

The C-terminal PR domain is most noted for its positive regulatory role in connecting SOS to activated receptors via Grb2. Grafting only the PR domain onto SOS^{Cat} revealed an inhibitory effect of this domain in restricting ligand-independent activation of SOS1 (**Fig. 3.5c**); this effect

was independent of the autoinhibitory effect of the HF and DH-PH domains. The magnitude of inhibition conferred by the PR domain was comparable to that of the DH-PH domain relative to SOS^{Cat} (**Fig. 3.5a,c**), thus demonstrating that the N- and C-terminal domains have similar potency in curbing the activity of the catalytic SOS^{Cat} core in resting cells.

Positive regulation of SOS activity in stimulated cells
Next we investigated SOS1 regulation in BCR-stimulated cells expressing intermediate SOS1-EGFP levels (**Fig. 3.5d–f**). It has been reported that autoinhibition by the DH domain can be released by electrostatic interaction of the PH domain with membrane lipids, thus allowing allosteric Ras binding[38,144,158]. In our p-FLOW assay, we found that the DH-PH domain alone had a purely inhibitory effect relative to that of SOS^{Cat} under conditions of BCR stimulation (**Fig. 3.5d**). In contrast with inclusion of the DH-PH, inclusion of the HF domain in SOS^{DPC} resulted in increased signaling output (**Fig. 3.5e**). We also observed a positive regulatory role of HF after BCR stimulation for SOS containing the PR domain (**Supplementary Fig. 5e–g**). These findings are in agreement with the in vitro observation that HF enhances the residence time of membrane-recruited SOS (**Fig. 3.3c**).

For the DH-PH, our results from stimulated cells conflicted with the increased dwell time observed in the SLB assays (**Fig. 3.3c**). The inhibitory effect of DH-PH was unexpected because PH-lipid interaction has been reported to positively regulate GTP loading of Ras in COS-1 cells and in mouse embryonic-stem-cell differentiation[38,144,158]. This disparity may arise from the HF truncation counteracting the phospholipid binding of PH in the cell system. To test this possibility, we introduced combined mutation of K456E and R459E (KR-EE mutation) within the PH domain, thereby disrupting the PIP2-PH interaction[144,160], and compared the BCR-stimulated ERK activation associated with the mutant and wild-type SOS1 variants (**Fig. 3.5g–i**). The KR-EE mutation in DPC format had a relatively small effect, resulting in a small decrease in pERK (**Fig. 3.5g**). However, the KR-EE mutation in HDPC markedly antagonized SOS1 activation throughout the entire assay duration, thus supporting the requirement of HF in stabilizing membrane-targeted SOS1 through phospholipid-PH interaction[151] (Fig. 5h). The KR-EE HDPC signals were comparable to those of the shorter wild-type DPC, thereby negating the positive regulatory effect of HF domain (**Fig. 3.5i**). These observations collectively indicate that the HF and PH domains, through lipid interactions, cooperatively stabilize active SOS1 at the membrane.

In sum, p-FLOW results (**Fig. 3.5**) combined with single-molecule measurements in our SLB assays (**Figs. 3.2** and 3.**3**) indicated that the flanking domains on both sides of SOS^{Cat} have evolved the ability to simultaneously dampen SOS activity in the basal state but enhance SOS activity after receptor stimulation (further discussed in **Supplementary Note 3**).

Regulation of super-processive SOS by endocytosis
SOS^{Cat}, SOS^{DPC}, and SOS^{HDPC} are all highly processive in SLB assays and in cellular p-FLOW

assays are less sensitive than SOS^{FL} to attenuation at late time points of induced signaling. Interestingly, SOS^{FL} mimics these characteristics of SOS truncation when functionalized with a C-terminally grafted farnesylation signal sequence from H-Ras, which artificially targets SOS1 to the membrane[168] (**Supplementary Fig. 6**). Deletion of the Grb2-binding domain of SOS1, its putative primary mode of membrane recruitment, thus produces a molecular and cellular phenotype resembling artificial membrane targeting.

To further investigate membrane recruitment and subsequent trafficking of SOS1, we imaged SOS1-EGFP in living cells by TIRFM and spinning-disc confocal microscopy. For this experiment, we used the hybrid live-cell SLB platform[169–172] to simulate the native signaling geometry of B cells interacting with antigen-presenting cells (**Supplementary Fig. 7a**). SOS-deficient DT40 B cells expressing human SOS1-EGFP were spread on SLBs functionalized with antibody that recognizes and activates the BCR[173], thereby triggering activation of SOS[174,175] (Online Methods).

B-cell activation from the supported membrane led to formation of BCR microclusters, as observed through TIRFM imaging of a Cy5 label on the antibody (**Fig. 3.6a**). SOS^{FL} was efficiently recruited to sites of BCR clusters, whereas SOS^{Cat} did not colocalize with BCR clusters, although it did localize to the membrane, presumably through binding allosteric Ras (**Fig. 3.6a,b**). SOS^{HDPC} also did not colocalize with the BCR clusters (**Fig. 3.6b** and **Supplementary Fig. 7b**). Contrasting reports have addressed the roles of signaling complexes and SOS1 function. In our B-cell system devoid of any endogenous SOS expression, chimeric SOS^{HDPC}-SH2, with a single SH2 domain of Grb2 grafted onto SOS^{HDPC}, did not colocalize with sites of BCR microclusters (**Fig. 3.6b** and **Supplementary Fig. 7b**). In contrast, addition of the PR domain to SOS^{Cat} or to SOS^{DPC} enabled SOS1-BCR colocalization (**Fig. 6b**, **Supplementary Fig. 7b** and **Supplementary Note 4**).

Over time, the initially scattered BCR clusters concatenated and moved toward the center of the synapses formed between the B cells and the SLB. Approximately 15–20 min after cell landing, a large central cluster appeared, a phenomenon commonly referred to as 'BCR capping'[176] (**Fig. 3.6c** and **Supplementary Movie 1**). SOS^{FL} initially moved with the activated BCR, but at later time points we found that it was depleted from the central BCR cluster (**Fig. 3.6d,e**). Thus, SOS^{FL} leaves the plasma membrane at the site of the central BCR cluster, and this occurrence also correlates with attenuation of SOS^{FL}-driven Ras-ERK signaling at later time points (**Fig. 3.4g**). Confocal fluorescence microscopy revealed the appearance of punctate SOS structures, which were located inside the cells and were reminiscent of endocytic vesicles (**Fig. 3.7a**). Moreover, these vesicle-like structures appeared only for SOS^{FL} but not for SOS^{HDPC} or the chimeric SOS^{HDPC}-SH2, and only on bilayers displaying the BCR-activating antibody (**Fig. 3.7a,b**). These observations suggest that removal of SOS1 from the membrane in a BCR-signal-dependent process requires the C terminus.

To more definitively address disappearance of SOS^{FL} from the plasma membrane, we used COS-1 cells with a much larger cytoplasmic volume than that of DT40 B cells. Visualization of transfected EGFP-tagged SOS^{FL} revealed predominantly cytoplasmic and evenly distributed SOS1 before epidermal growth factor (EGF) stimulation. We observed prominent membrane recruitment of SOS1 at the plasma membrane 10 min after EGF stimulation. By 30 min after stimulation, most SOS molecules had localized to perinuclear vesicular structures (**Fig. 3.7c**). The vesicular SOS1 colocalized with the early endosomal marker protein Rab5 (ref. [177]), thus indicating that SOS1 molecules are removed from the plasma membrane via endocytosis (**Fig. 3.7d**). We found that the kinetics of SOS1 endocytosis was influenced by the allosteric Ras-binding pocket. A SOS1 mutant impaired in allosteric Ras binding (SOS$^{FL\ L687E\ R688A}$) exhibited accelerated endocytosis (**Fig. 3.7e**). Binding of SOS1 to Ras via its allosteric pocket thus appears to counteract the endocytosis of SOS1.

DISCUSSION

Signal propagation from receptors to the Ras pathway is commonly accepted to involve recruitment of SOS from the cytosol to the plasma membrane via the adaptor protein Grb2. In its classical interpretation, the increased membrane localization of SOS is presumed to tip the RasGEF-RasGAP balance at the membrane in favor of Ras activation, thus explaining how signals are relayed downstream. However, several results have challenged this classical model, particularly the recurring observation that SOS-truncation mutants lacking the Grb2-binding PR domain remain signaling competent in cells[154–159]. More recently, we have shown that SOS stably associates with a lipid-membrane surface by engaging Ras at the allosteric binding pocket. In reconstituted-membrane systems, this mechanism alone (i.e., independently of other mechanisms of SOS membrane anchoring) is sufficient for sustained association of SOS with the membrane, where it can processively activate thousands of Ras molecules[116]. Strikingly, essentially no dynamic equilibrium is present; membrane recruitment of SOS is quasi-irreversible at signaling-relevant timescales.

Here we demonstrated that the membrane recruitment probability of SOS by allosteric Ras is strongly accelerated by RasGTP relative to RasGDP, thereby explaining how SOS constructs lacking the Grb2-binding PR domain are capable of sensing receptor triggering. In a cellular context, RasGTP levels are primed after receptor activation, for example, because of the activity of RasGRP or other exchange factors that produce RasGTP and facilitate SOS recruitment; this process is fueled by strong positive feedback as the recruited SOS produces increasingly more RasGTP. This ability to respond to receptor stimuli independently of Grb2 is further augmented by the lipid-interacting PH and HF domains, which bind lipidic second messengers such as PIP2 and phosphatidic acid.

In light of the spontaneous and nearly irreversible activating characteristics of SOS, the question shifts to how receptor-mediated signals maintain control of SOS via Grb2 binding. The literature abounds with apparently conflicting results on this matter. In particular, it has been unclear whether the C-terminal PR domain plays a positive, redundant, or even negative regulatory role in SOS signaling. Our p-FLOW assay, which considers the multifactorial aspects of signal transduction (i.e., expression level, pathway activity, and time after receptor stimulation), revealed that the PR domain performs dual functions in receptor-stimulated cells, acting as either a signal facilitator or a signal terminator, depending on the phase of the signaling process. In addition, the PR domain contributes to inhibition of SOS in the basal state.

From the perspective of receptor-mediated activation of SOS, Grb2 binding by the PR domain clearly increases the rate of activation. Our multiparameter mapping of the activity of the SOS-Ras-ERK cascade, enabled by reconstitution of SOS1 in SOS-deficient B cells, revealed that spontaneous activation of SOS scales with SOS expression level. Essentially, the spontaneous activation of SOS is driven by Le Chatelier's principle and is simply a probabilistic event that scales with concentration. Under endogenous expression levels, this spontaneous activation must be sufficiently slow as to be inconsequential in the context of background GAP activity, thus requiring the additional boost from receptor-mediated Grb2 recruitment to trigger a productive Ras signal (extended discussion in **Supplementary Note 5**; **Supplementary Fig. 8a–d**). We propose endocytosis as a method of signal attenuation that provides an actively regulated mechanism to remove SOS from the plasma membrane, effectively cutting off access to new Ras molecules. SOS constructs lacking the PR domain are not endocytosed, and they exhibit sustained ERK activation levels (further discussed in **Supplementary Note 6**). Thus, in its natural state, SOS activation follows a one-way trafficking circuit with active removal from the membrane via the PR domain as the shutdown mechanism.

Recently, it has become clear that single–amino acid variants in RasGEFs have a profound biological effect. We established that the EF hands in RasGRP1 play a dual role in keeping this RasGEF in the autoinhibited state while simultaneously allowing for calcium-induced activation[178]. A single–amino acid variant allele, *Rasgrp1Anaef*, with a point-mutated EF hand, perturbs both regulatory roles of this domain and leads to autoimmune features in *Rasgrp1Anaef* mice[179]. The structural basis for PR-domain-facilitated autoinhibition and the transition to the activated state of SOS is unknown, because efforts to produce functional full-length SOS1 protein including the PR domain have been unsuccessful to date. Mining public databases, we found several *SOS1* variants with point mutations or stop codons in the PR domain, which are linked to Noonan developmental syndrome, hyperplastic syndromes such as hereditary gingival fibromatosis[180], and various cancers (**Supplementary Fig. 8e**). It is plausible that subtle point mutations in the PR domain may have substantial biological effects and contribute to human disease.

METHODS

Proteins and reagents
H-Ras$^{C118S\ C181}$ (H-Ras construct containing residues 1–181 with a single cysteine at position C181 used for coupling to the bilayer, termed Ras herein), SOS^{Cat} Cys-lite (residues 566–1049 with the following mutations: C838A, C635A, C980S, and E718C), SOS^{DPC} (residues 198–1049), SOS^{HDPC} (residues 1–1049), and SOS$^{HDPC\ R552G}$ (residues 1–1049 with R552G) of human SOS1 were expressed in *Escherichia coli* and purified as previously described[38]. Lipids were purchased from Avanti. TR-DHPE, BODIPY-GDP, and BODIPY-GTP were purchased from Invitrogen. ATTO 647N–maleimide, ATTO 488–labeled guanosine diphosphate (EDA–GDP–ATTO 488) and EDA–GppNp–ATTO 488 (nonhydrolyzable analog of GTP were purchased from Jena Bioscience. GTP was purchased from Sigma-Aldrich, and GDP was purchased from MP Biomedicals. Biotinylated anti-chicken IgM was purchased from Sigma (SAB3700240), and Cy5-labeled streptavidin was from Life Technologies (43-4316). Validation information for commercial antibodies is available on the manufacturers' websites.

Protein labeling and benchmarking
SOS constructs were fluorescently labeled by reaction of 1:10 molar ratio of unlabeled protein with ATTO 647N–maleimide for 2 h at 23 °C. Unreacted fluorophores were removed with PD-10 columns (GE Healthcare). The degree of labeling was determined by UV-vis spectroscopy (NanoDrop 2000, Thermo Scientific), yielding 90% for SOS^{Cat} Cys-lite, 119% for SOSDPC, 106% for SOS^{HDPC}, and 118% for SOS$^{HDPC\ R552G}$. SOS^{DPC}, SOS^{HDPC} and SOS$^{HDPC\ R552G}$ contained multiple cysteines, thus explaining why labeling efficiencies exceeded 100%. Dye labeling can potentially alter protein behavior, and caution is always needed in the interpretation of related results. Here, nucleotide-exchange experiments were conducted to ascertain that labeling did not alter enzyme behavior; comparison of unlabeled and labeled constructs in the stopped-flow assay indicated that labeling had a negligible effect on the *in vitro* activity of SOS in our system (**Supplementary Fig. 1c**).

Ras-decorated supported lipid bilayers for *in vitro* assays
Ras decorated bilayers were prepared as previously described[38,116]. Lipids dissolved in chloroform were mixed in a round-bottomed flask. Solvent was evaporated by rotary evaporation (40 °C, 10 min) followed by N2 flow (20 min). Small unilamellar vesicles (SUVs) were formed by rehydration of the dried lipid film in PBS (pH 7.45). The vesicle suspension was extruded 11 times (Avestin Miniextruder, 30-nm-pore-diameter polycarbonate membranes; Millipore). The lipid composition was 3% DOPS, 3% MCC-DOPE, 0.01% TxRed-DHPE, and the remainder Egg-PC.

SLBs were formed by incubation of the SUV suspension for 30 min on cleaned piranha-etched glass slides mounted in flow chambers (FCS2 flow chambers, Bioptechs). The sample was incubated with casein in PBS (2.5 mg/ml) for 10 min and was then incubated for 2.5 h with Ras

in PBS (1 mg/ml). After Ras incubation, unreacted MCC was quenched by treatment with 2-β-mercaptoethanol in PBS (5 mM) for 10 min. A motorized syringe pump (PHD 2000, Harvard Apparatus) was used throughout the sample preparation for liquid injections and washing steps.

For loading of fluorescent nucleotide onto Ras, samples were equilibrated at 4 °C and washed with 3 mL loading buffer (40 mM HEPES and 150 mM NaCl, pH 7.4); the native nucleotide bound to Ras was stripped in a 20-min incubation with EDTA in loading buffer (50 mM EDTA, 40 mM HEPES, and 150 mM NaCl, pH 7.4). This step was immediately followed by overnight incubation of samples with 10 μM fluorescent nucleotide analog in reaction buffer (40 mM HEPES, 100 mM NaCl, and 5 mM $MgCl_2$, pH 7.4). Fluorescent nucleotides used in this study included BODIPY-GDP, BODIPY-GTP, ATTO 488–GDP, and ATTO 488–GppNp. A control experiment in which samples underwent all steps except Ras incubation showed no detectable nonspecific binding of the applied fluorescent nucleotides to the SLB.
Immediately before microscopy, samples were brought to room temperature, and any unbound fluorescent nucleotide was removed by washing with 3 mL reaction buffer (40 mM HEPES, 100 mM NaCl, 5 mM $MgCl_2$, and 1 mM TCEP, pH 7.4) under constant flow. The two-dimensional fluidity of lipids and Ras was confirmed for each sample with fluorescence recovery after photobleaching (FRAP).

Antibody-functionalized supported lipid bilayers for live cell imaging
Bilayers for live-cell experiments were prepared as described above, with a lipid composition of 5% DOPS, 0.1% biotinyl cap PE, 0.005% TxRed-DHPE, and the remainder Egg-PC. A piranha-etched glass slide (1, Fisher Scientific) mounted in a microscopy chamber (A-7816, Life Technologies) was incubated with SUV suspension (1 mg/mL) for 30 min. The sample was then treated with Cy5-labeled streptavidin (18.8 nM) for 30 min and was then incubated with biotinylated anti-chicken IgM (62 nM; SAB3700240, Sigma) for 30 min. Each incubation step was followed by copious washing with PBS.

Stopped flow supported lipid bilayer assay
Labeled and unlabeled SOS constructs were mixed at the desired ratio (typically 1:20) at a total concentration of 100 nM and flowed over the bilayer as a transient pulse. The number of labeled SOS molecules remaining on the bilayer after the pulse (due to capture by catalytic Ras in the absence of free nucleotide)[99,155] was counted at the single-molecule level and used to infer the recruitment probability (**Supplementary Note 7**). We experimentally confirmed that SOS in our system was indeed stably tethered to the bilayer via Ras in the absence of free nucleotide. For Y64A experiments, SOS engaged the membrane in a transient manner (**Fig. 3.2c**), and the extent of binding was inferred from the observed peak binding during the SOS pulse instead of from the plateau (data in **Fig. 3.2d**).

The nucleotide-exchange reaction was initiated by providing a continuous flow of nucleotide (120 μM GDP or GTP). SOS desorption and nucleotide-exchange kinetics were quantified at

different time points by acquisition of an image of the fluorescent nucleotide on Ras and ten images of the labeled SOS. For each time point, we imaged a different position in the flow chamber to avoid bleaching. The ten images of SOS at each position allowed us to discard immobile SOS in the analysis (i.e., SOS bound to defects in the bilayer). This is a crucial aspect of the experimental design because it avoids bias from sample-to-sample variation in the number of defects as well as possible differential tendencies of various protein constructs to adhere to bilayer defects. By counting membrane-bound SOS through single-molecule tracking, we were able to focus entirely on species that are laterally mobile.

A clear demonstration that the assay probed specific interactions between Ras and SOS came from the observation that all SOS constructs tested exhibited sensitivity to the nucleotide state of Ras with consistently increased recruitment probability as well as a prolonged residency period on membranes displaying RasGTP (**Fig. 3.2d** and **Supplementary Fig. 3a–c**).

For specific comparison of desorption for successfully activated SOS constructs (**Fig. 3.3c**), traces were normalized to the SOS count at the membrane observed at the initiation of the nucleotide chase. For SOS^{Cat}, we observed a fraction of rapidly desorbing species during the first few seconds of the chase (**Fig. 3.2c**). This fast-desorbing fraction did not contribute to processive Ras turnover (**Supplementary Fig. 1d**), and for the comparisons with other constructs (**Fig. 3.3c** and **Supplementary Fig. 3b,c**), we cropped the first 10 s of the trace.

Maintenance and transfection of DT40 and Jurkat cell lines
Culture maintenance, plasmid transfection, and BCR stimulation of chicken DT40 B cell lines were carried out as previously described[98]. Jurkat cell culture and transfection techniques were also performed as previously described[59]. The SOS1−2− DT40 B cells were generated in T. Kurosaki's laboratory (RIKEN). Both wild-type and SOS1−2− DT40 B cells were gifts from T. Kurosaki. The obtained cell lines were confirmed to be free of mycoplasma contamination. For routine cell functional authentication, surface expression of B-cell receptor (BCR) was confirmed by flow cytometry and by BCR-induced pERK2 measurement similar to the experiment shown in **Supplementary Figure 4**. Jurkat T cells were obtained from the ACCC and were maintained according to the provided guidelines.

To generate EGFP-tagged hSOS1 variants, EGFP coding sequence (CDS) was PCR-amplified with Xba I- and Not I-flanked primers from pEGFP-N1 plasmid (Clontech). The resulting SOS1-EGFP construct bears a five–amino acid linker (SRGGR) between SOS1 and EGFP CDS. Expression was confirmed by western blotting with anti-GFP antibody (Cell Signaling, 2956) (Supplementary Fig. 4a).

Live cell imaging
For live cell microscopy, 2.5 million cells were exchanged from cell culture media to 1mL of serum-free RPMI by pelleting cells through 5 min centrifugation at 500g; this was followed by

30-min incubation in serum-free RPMI at 37°C. Cells were imaged in pH 7.40, 10 mM HEPES, 68 mM NaCl, 2.5 mM KCl, 0.35 mM Na_2HPO_4, 3 mM D-Glucose, 1 mM $CaCl_2$, 2 mM $MgCl_2$, and 0.1% BSA.

Live-cell imaging was performed with a stage-top incubator and an objective heater (Chamlide TC-A, Quorum Technology). Experiments were initiated by addition of cells to SLBs functionalized with anti-BCR (Sigma, SAB3700240). The bilayer was heated to 37 °C before addition of cells. The 488-nm channel was used for SOS-EGFP, and the 640-nm channel was used for BCR-engaged antibody on SLBs. For a few selected cells, TIRF images were acquired every ~1–5 min to follow the kinetics of the signaling reaction. Approximately 30 min after cells were added to the chamber, 488-nm and 640-nm TIRF, together with bright field and RICM micrographs were acquired at a number of positions in the microscope chamber.

Flow cytometry and data analysis

Jurkat T cells were transiently transfected for 20 h with 10 μg of wild-type or allosteric mutant (W729E) SOS^{Cat}-encoding plasmid together with 10 μg of GFP plasmid. The activity of the Ras-ERK pathway was measured by FACS staining of surface CD69 (sCD69, BD Pharmingen, 555531) together with GFP intensity measurements. GFP-positive cells were subgated into nine fractions. The geometric mean fluorescence of CD69 was determined for each fraction.

For quantitative and qualitative assays of the RAS-ERK signal module, intracellular staining of BCR-induced ERK phosphorylation was performed according to established procedures46. In brief, cells were stimulated with BCR cross-linking mouse IgM (clone M4, Southern Biotech, 8300-01) for the desired time period. Stimulation was then stopped by addition of 4% paraformaldehyde-PBS, and cells were fixed for 20 min at room temperature. Fixed cells were washed three times with FACS wash buffer (PBS, 1% BSA, and 10 mM EDTA) and subsequently permeabilized with prechilled 90% methanol overnight. Cells were then washed three times with FACS wash buffer and stained for pERK with rabbit antisera (Cell Signaling, 9101). pERK was visualized by secondary staining with goat anti-rabbit IgG conjugated with APC (Jackson Immunochemicals, 711-136-152).

For FACS acquisition, a minimum of 100,000 events were collected for each time point with a FACSCalibur machine (BD) and analyzed with FlowJo software. For analysis of ERK activation, cells were sorted into nine bins of equal intervals according to their SOS expression level. Subsets with fewer than 100 acquired events were disregarded for fair comparison of SOS1 variants with different expression levels.

COS1 cell transfections and immunofluorescence staining

COS1 cells were cultured and treated as previously described[38]. COS1 cells were obtained from ACCC. In brief, cells grown on cover slips were transfected with either the pCGT-T7-SOS^{Cat} or $SOS^{Cat-L687ER688A}$ construct together with GFP-tagged H-$Ras^{A59G\ D38E}$–encoding plasmid. After 24

51

h, transfected cells were fixed in 3.7% (v/v) formaldehyde and permeabilized with 0.1% (v/v) Triton X-100. Expressed SOS proteins were visualized by staining with anti-T7 antibody (EMD Millipore, AB3790), followed by rhodamine-conjugated anti-mouse antibody (Cappel, R-6393). Rab5 protein was expressed as a GFP-fusion protein. EGF was obtained from Invitrogen. Imaging was conducted on a Zeiss Axiovert 200M microscope.

Optical microscopy platforms
Epifluorescence and total internal reflection fluorescence microscopy was performed on a Nikon Eclipse Ti inverted microscope with a Nikon Apo TIRF 100× oil immersion objective (1.49 NA) and an EMCCD camera (Andor iXon 597DU). A mercury arc lamp was used for epifluorescence illumination. 488-nm (Sapphire HP; Coherent) and 647-nm (RCL-050-640; Crystalaser) lasers were used for through the objective TIRF imaging. Band-pass emission filters for 488- and 647-nm TIRF images were HQ515/30 and HQ700/75 (Chroma Technology), respectively. The microscope was operated with MetaMorph software (Molecular Devices).

For live-cell experiments, an additional TIRF setup was used with the following specifications: inverted microscope body (Nikon Eclipse Ti (Ti HUBC/A), Technical Instruments) equipped with a Nikon Apo TIRF 100x oil objective (1.49 NA). The microscope had a custom-built laser launch with 488-nm, 561-nm, and 633-nm lasers (all from the OBIS product line, Coherent) controlled via a laser control module (OBIS scientific remote). The TIRF setup was operated through the objective mode, and images were collected on an EMCCD (iXon ultra 897, Andor). The microscope was controlled with μManager[128].

Confocal microscopy was performed on a custom-built spinning-disk confocal system[181]. Briefly, images were captured with a Nikon Apo TIRF 100× oil-immersion objective (1.49 NA) and an EMCCD (Andor iXon3 888), and the microscope was controlled with μManager[128]. The axial slice step size was 0.5 μm.

Data analysis: A detailed description of the data analysis procedures relating to imaging experiments can be found in **Supplementary Note 7**.

Code availability: Supplementary Note 7 provides a detailed description of the data analysis procedures that can be implemented in a given coding language.

FIGURES
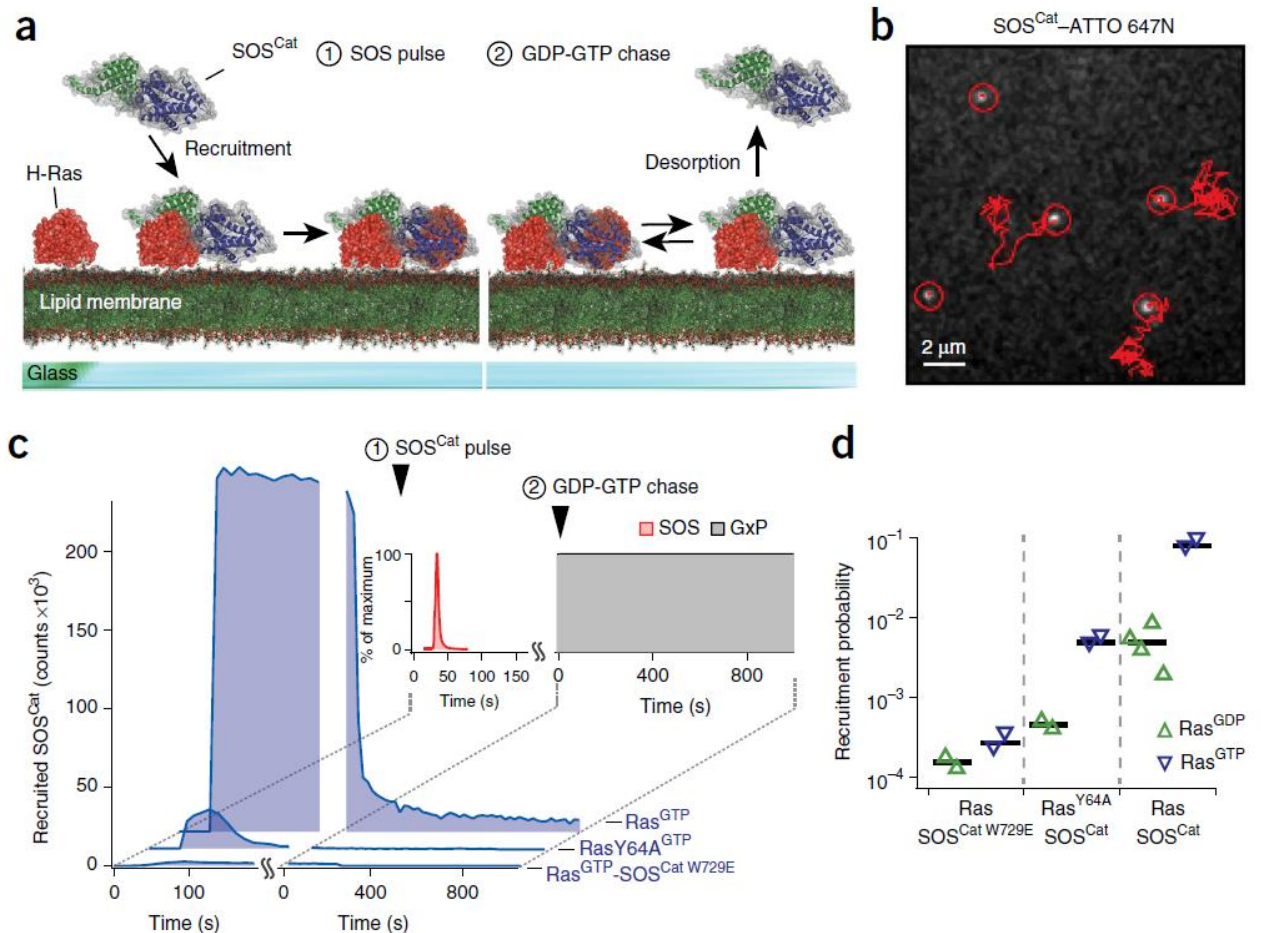
Figure 3.1. The catalytic core of SOS is stably and functionally recruited to Ras-decorated SLBs *in vitro*, independently of Grb2 and lipid-binding domains. (**a**) The domain architecture of full-length (FL) hSOS1. The catalytic unit (Cat) is depicted together with the flanking regulatory domains. Yellow boxes in the C-terminal PR domain indicate PxxP motifs, which interact with Grb2. (**b**) Classical model of the SOS-Ras-ERK signal-transduction pathway. In the shown example, SOS is recruited to the plasma membrane downstream of activated B-cell receptors via binding of Grb2 to phosphotyrosine motifs on the adaptor protein LAB. (**c**) Single SOS activity assay based on micropatterned Ras-functionalized fluid SLBs. (**d**) Representative overlay image of fluorescent GDP bound to Ras (red channel) and membrane-recruited SOS^{Cat} (green channel) in the single-molecule assay depicted in **c**. Darker areas with depleted signal in the GDP channel indicate membrane corrals to which individual copies of SOS^{Cat} were recruited and exhibited highly processive SOS^{Cat} activity, activating Ras in a sustained manner without dissociating from the membrane surface. This experiment was repeated five times.

53
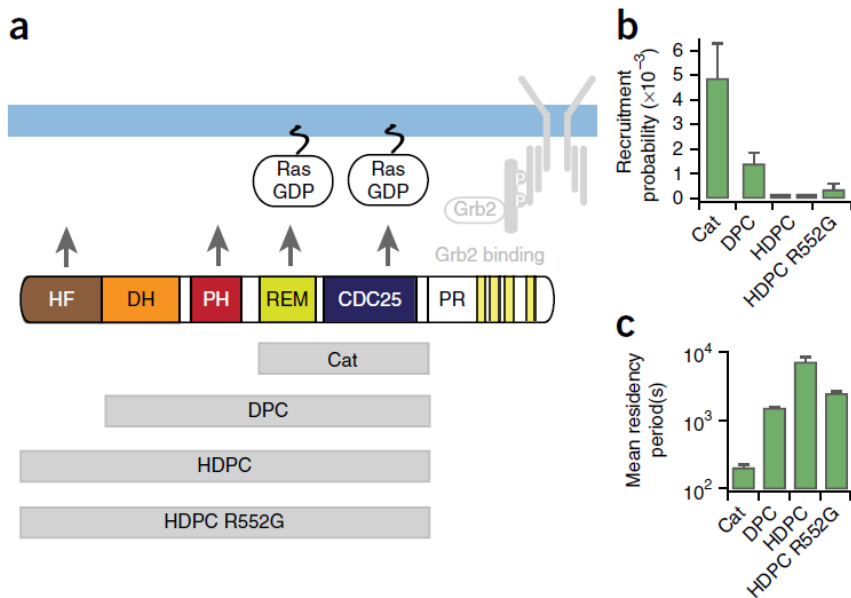
Figure 3.2. Stopped-flow SLB assay probing SOS recruitment and desorption. (**a**) Cartoon representation of the two phases of the assay. (**b**) Single-molecule tracking of ATTO 647N–labeled SOS^{Cat} diffusing at the bilayer. (**c**) Traces from the stopped-flow assay. Experiments used SOS^{Cat}; SOS$^{Cat\ W729E}$, a mutant with an abolished allosteric pocket; and RasY64A, a construct deficient in binding to the active site of SOS. The indicated counts are for a field of view of 55 × 55 μm^2 and were scaled according to the applied ratio of unlabeled to labeled enzymes. (**d**) Membrane recruitment probabilities quantified from phase 1 of the stopped-flow assay. Each triangle represents data from a SLB sample. Black horizontal lines indicate the average of the data shown for each condition. Source data for plots and graphs are available online.
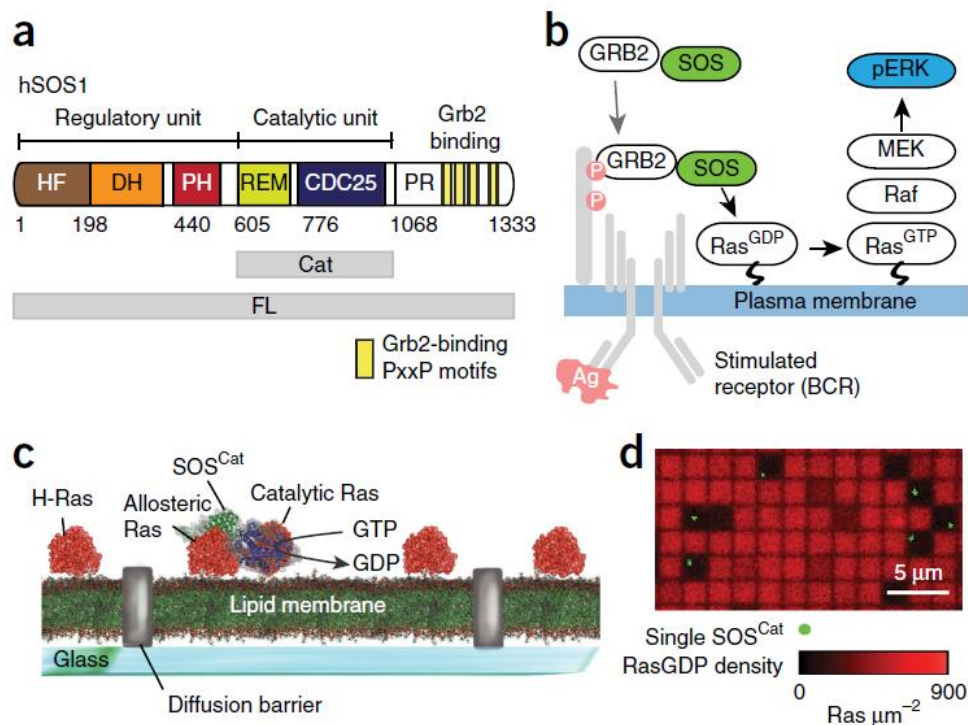
Figure 3.3. The N terminus of SOS suppresses bilayer recruitment while prolonging dwell time in the active membrane-bound state. (**a**) SOS constructs tested in the stopped-flow SLB assay. All experiments shown were conducted with RasGDP on the bilayer. (**b**) Recruitment probability of SOS constructs obtained from the stopped-flow assay. Each bar represents the average of data collected for the following number of SLB samples, except for HDPC, for which each bar reflects data from one SLB: SOS^{Cat}, $n = 4$; DPC, $n = 4$; HDPC, $n = 2$; HDPC R552G, $n = 3$. Each sample was imaged in at least 15 different positions. Error bars, s.e.m. (data for SOS^{Cat} are replotted from **Figure 2** for comparison). (**c**) Membrane residence time of SOS constructs obtained from the stopped-flow assay. The mean residency period for each construct was obtained by fitting desorption traces (**Supplementary Fig. 3b**) from the following number of SLB samples: SOS^{Cat}, $n = 5$; DPC, $n = 4$; HDPC, $n = 2$; HDPC R552G, $n = 3$. Error bars, estimated s.d. of the fit coefficient for an average over the indicated samples. Source data for plots and graphs are available online.
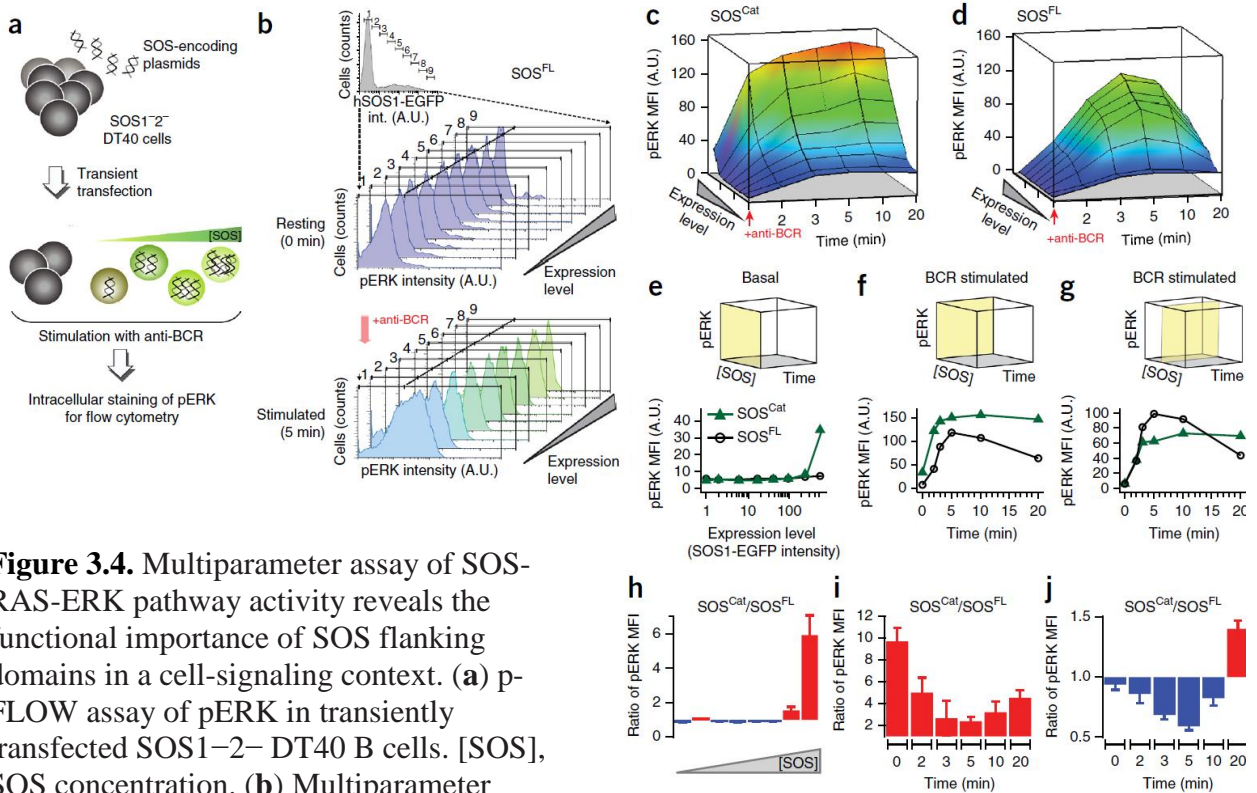
Figure 3.4. Multiparameter assay of SOS-RAS-ERK pathway activity reveals the functional importance of SOS flanking domains in a cell-signaling context. (**a**) p-FLOW assay of pERK in transiently transfected SOS1−2− DT40 B cells. [SOS], SOS concentration. (**b**) Multiparameter analysis of the SOS-RAS-ERK pathway in model B cells expressing human SOS^{FL} C-terminally fused to an EGFP label. A.U., arbitrary units; int., intensity. (**c,d**) BCR-induced SOS-RAS-ERK pathway activation as a function of increasing SOS expression level and time after stimulation of BCR for SOS^{Cat}-expressing (**c**) and SOS^{FL}-expressing (**d**) cells. Arrowheads indicate the time of BCR activation. The pERK level is reported as mean fluorescence intensity (MFI). (**e**) Comparison of basal pERK level across increasing protein concentrations of SOS^{Cat} and SOS^{FL}. The yellow plane on the cube indicates the subspace of the 3D parameter space of the assay corresponding to the shown traces. (**f,g**) Comparative plots representing the dynamic change in BCR-induced pERK as a function of stimulation time in cells expressing superphysiological levels (**f**) and intermediate levels (**g**) of SOS^{Cat} and SOS^{FL}. (**h–j**) Ratios of pERK observed in SOS^{Cat}- and SOS^{FL}-transfected cells, corresponding to traces in **e–g**. Red fill indicates increased activity of SOS^{Cat} as compared to SOS^{FL}, whereas blue fill highlights decreased relative activity. Data are based on seven independent cell cultures and p-FLOW experiments. Error bars, s.e.m. Source data for plots and graphs are available online.
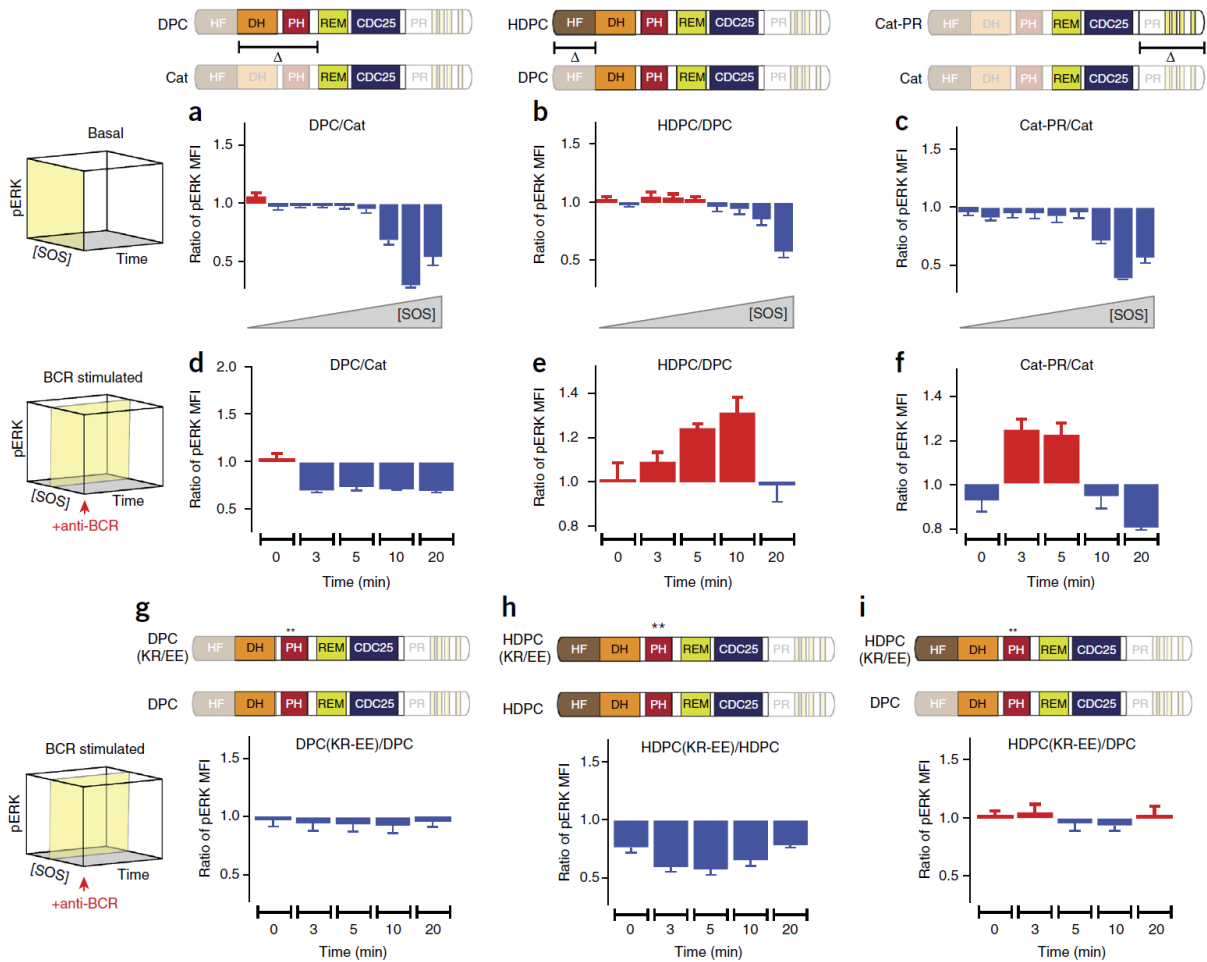
Figure 3.5. SOS^{Cat} flanking domains block spontaneous activation in the basal state but promote RAS-ERK signal transduction after receptor stimulation. (**a–c**) p-FLOW assays showing inhibition of spontaneous ERK activation after addition of SOS^{Cat} flanking domains: DH-PH domain (**a**), HF domain (**b**), and PR domain (**c**) (depicted schematically in domain diagrams at the top). The ratio of pERK MFI for longer to shorter SOS variants is plotted against increasing SOS concentration for unstimulated cells (basal state). (**d–f**) Time dependence of the pERK MFI ratio after BCR stimulation, plotted for the DH-PH domain (**d**), HF domain (**e**), and PR domain (**f**) (depicted schematically in domain diagrams at the top). (**g–i**) Comparison of BCR-induced ERK activation in the KR-EE PH-domain mutant (**) and wild-type SOS1 variants, showing disruption of membrane lipid interaction in the KR-EE mutant. Yellow planes on the cubes to the left indicate the corresponding subspace of the 3D parameter space in the p-FLOW assay (c.f. **Fig. 4c,d**). Data are based on three independent experiments. Error bars, s.e.m. Source data for plots and graphs are available online.
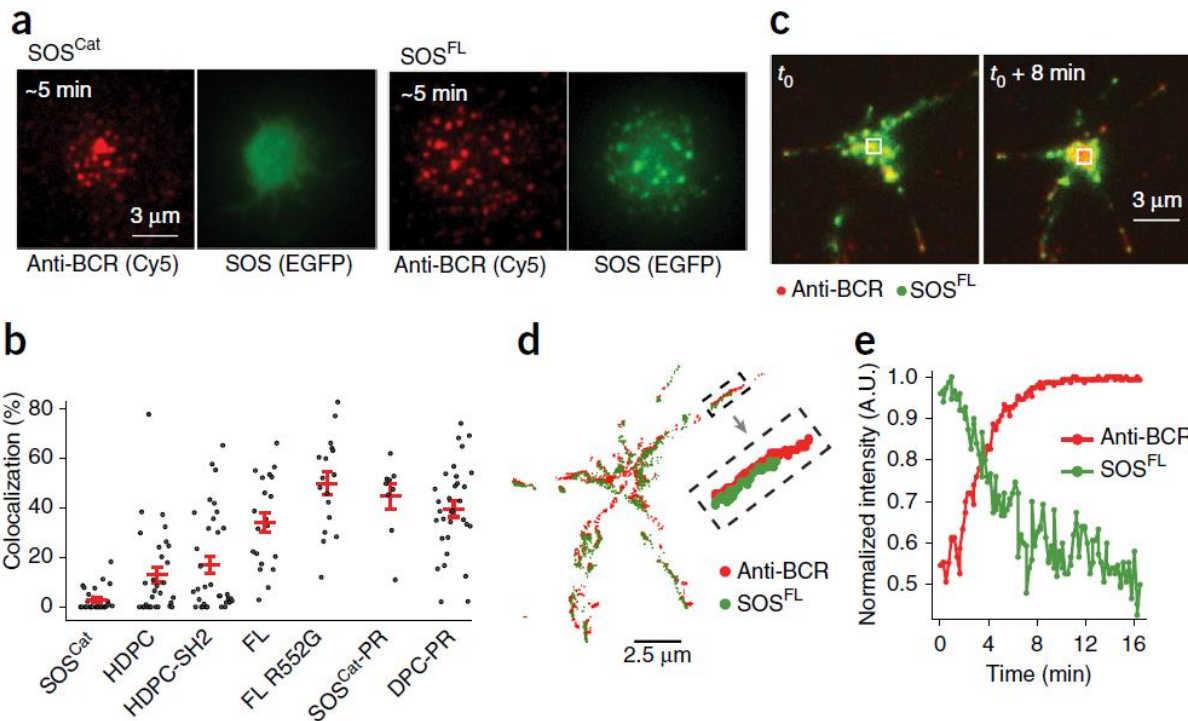
Figure 3.6. PR-domain-dependent localization of SOS to BCR microclusters and SOS depletion from the central BCR cluster formed between B cells and SLBs decorated with BCR-cross-linking antibody. (**a**) Representative TIRFM images illustrating spatial localization of SOS and BCR microclusters. Cells expressing SOS^{Cat} (left) and SOS^{FL} (right) at an early (~5-min) time point after contacting the bilayer are shown. The number of replicates is given in **b**. (**b**) Colocalization of different SOS variants and BCR microclusters. Each dot on the graph represents data from one cell. Red horizontal lines indicate average ± s.e.m. for the shown scatter data. Numbers of cells/SLB samples are: SOS^{Cat}, 28/5; HDPC, 30/2; HDPC-SH2, 34/2; FL, 21/2; FL R552G, 17/2; SOS^{Cat}-PR, 9/2; DPC-PR, 32/1. (**c**) Overlay of anti-BCR (Cy5, red) and SOS (EGFP, green) fluorescence signals before (left) and after (right) the formation of a central BCR cluster. The displayed overlays are also plotted as separate image channels in **Supplementary Figure 7c**. (**d**) Trajectories of BCR (red) and SOS^{FL} (green) movement at the cell-bilayer interface. The trajectories were obtained by tracking individual BCR and SOS clusters in a time lapse (**Supplementary Movie 1**) of the cell shown in **c**. Each tracked position of a microcluster is indicated by a dot. Chains of connected dots draw out microcluster trajectories. (**e**) Normalized time traces of the fluorescence intensity of SOS^{FL}-EGFP and BCR at the center of the cell-supported bilayer synapse for the cell shown in **c**. The phenomenon of SOS depletion from the central BCR cluster was observed in 69% of SOS^{FL}-expressing cells (95 cells imaged over five experiments). Source data for plots and graphs are available online.
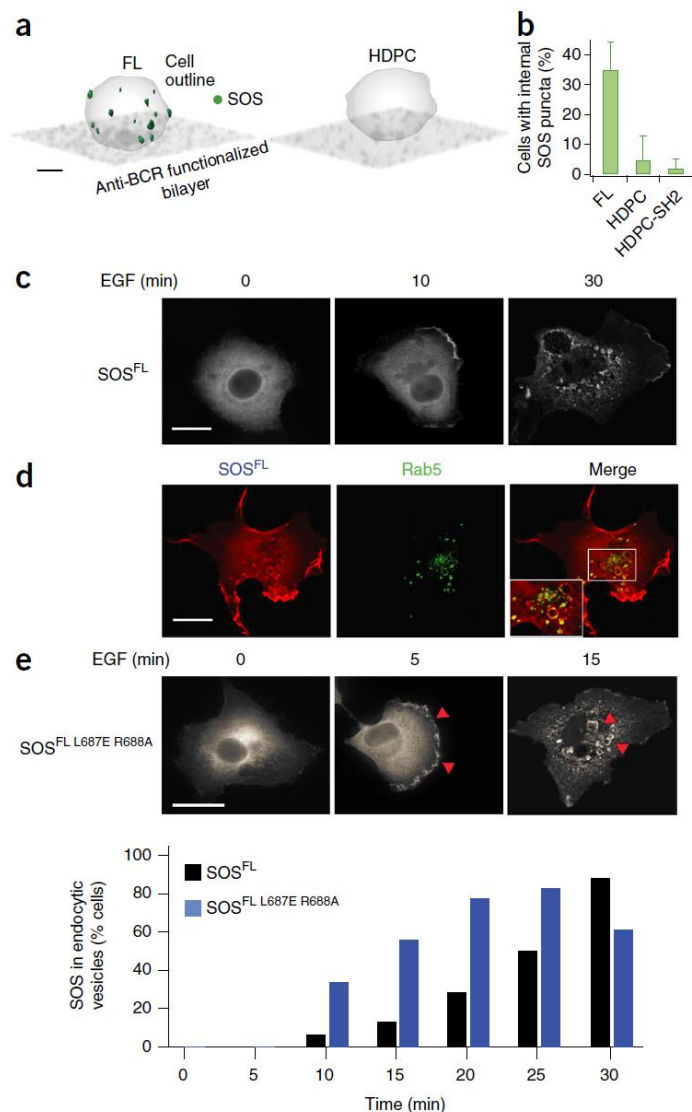
Figure 3.7. PR-domain-dependent SOS endocytosis mediates signal attenuation. (**a**) Confocal data in 3D rendering, showing SOS^{FL}-enriched vesicle-like structures appearing away from the cell-bilayer contact zone at late time points (~10–30 min after cell landing). Scale bar, 3 μm. (**b**) Statistics of cells displaying internal SOS puncta, as shown in **a**. Numbers of cells/SLB samples/cell cultures are: FL, 97/4/2; HDPC, 75/3/2; HDPC-SH2, 78/3/2. Error bars, s.d. across SLB samples. (**c**) Localization of EGFP-tagged SOS1^{FL} in COS-1 cells stimulated with EGF for the indicated time points. Scale bar, 10 μm. (**d**) Colocalization of internalized SOS1 with the Rab5 endosomal marker in COS-1 cells stimulated for 25 min with EGF. Images shown are representative of the colocalization pattern observed in >75% of the cells in three independent experiments (25 cells analyzed per experiment). The enlarged inset in the merged image is also plotted in **Supplementary Figure 7d** as separate image channels. Scale bar, 10 μm. (**e**) Kinetics of SOS localization to endocytic vesicles in EGF-stimulated COS-1 cells. EGFP-tagged SOS^{FL} is compared with an SOS1FL molecule with a functionally impaired allosteric pocket (SOS$^{FL\ L687E\ R688A}$). Representative images accompany the bar graph. The results represent an average of two independent experiments (25 cells counted per condition for each experiment). Scale bar, 10 μm. Source data for plots and graphs are available online.

CHAPTER 4.

A SMALL MOLECULE DRUG TARGETS RAS ACTIVATION BY PREVENTING SOS RECRUITMENT

Meredith G. Triplet[1], Shalini T. Low-Nam[1], Nicholas F. Endres[3], Jay T. Groves[1,2]

[1]Department of Chemistry, University of California, Berkeley, California 94720, USA; [2] Physical Biosciences Division, Lawrence Berkeley National Laboratory, Berkeley, California 94720, USA; [3]Genentech, Inc., One DNA Way, South San Francisco, CA 94080

AUTHOR CONTRIBUTIONS

MGT, NFE, and JTG conceived experiments. MGT performed in vitro experiments and analyzed data. STLN provided cells, and MGT and STLN performed live cell measurements. NFE provided DCAI compound. MGT and JTG wrote the paper. All authors discussed and commented on the manuscript.

ACKNOWLEDGMENTS

ABSTRACT

Due to the prevalence of oncogenic Ras mutations, effective drugs are needed to target this protein in the clinical setting. In solution studies, a small molecule, DCAI, has been shown to interact with a novel binding site of the surface of Ras and to interfere with Ras activation by the effector SOS. Here, we establish that DCAI activity functions by modulating the recruitment of SOS to Ras. Reducing the recruitment of SOS can impede the activation of Ras. Combined measurements on supported lipid bilayers and in EGF-stimulated single-cell measurements show that DCAI impacts both receptor-mediated SOS recruitment and the non-mediated positive feedback SOS engagement with Ras. This proposes a novel mechanism for targeting Ras activation and suggests clinical potential for the small-molecule binding pocket on Ras's surface utilized by DCAI.

MAIN TEXT

Ras serves as a molecular switch that is 'off' when bound to GDP, but 'on' when it is bound to GTP. Aberrant activation of Ras causes 30% of all human cancers[101,106,163]. Nevertheless, as of yet, there is no drug that is used clinically to restore regular activation levels in Ras-driven cancer cells[182]. Recent studies have attempted to block interactions between Ras and its effectors and modifying proteins, but have had mixed success[182–185]. DCAI is a small molecule that binds to a previously unknown pocket on the surface of Ras, resulting in reduced activation[109].

Ras undergoes substantial post-translational modification, including farnesylation[54,101]. Not only does this serve to localize Ras to the membrane surface, but also positions it to activate, and to be activated by, its effectors[106,186]. One important class of Ras effectors, Guanosine nucleotide Exchange Factors (GEFs), spur the activation of Ras by causing nucleotide release, allowing cytosolic GTP to take the place of GDP[97,187,188].

Son of Sevenless (SOS) is a Ras GEF that is known to participate in Ras activation leading towards diverse responses, including cell growth[139]. The catalytic core of Ras includes a REM and a CDC25 domain, and can bind Ras in two distinct sites: one allosteric, and one catalytic. The allosteric site preferentially binds RasGTP, providing a positive feedback loop[152]. When combined with spatiotemporally confinement, this feedback loop is speculated to be a key component of the cell's triggering mechanism[60]. The Dbl homology (DH), pleckstrin homology (PH) and histone fold (HF) N-terminal domains, along with a C-terminal proline rich (PR) domain, flank the SOS catalytic core. The DH, PH, and HF domains play vital roles in membrane association and autoinhibition[100,164]. The PR domain serve as a GRB2-binding site, which is part of a signaling cascade and brings SOS to the membrane in cells[139].

Historically, it has been assumed SOS is dependent upon the signaling cascade, and specifically GRB2 activation, to be recruited to the membrane[97]. However, recent results have shown that SOS is able to dwell on the membrane for long times (minutes to hours) without any upstream signaling partners[60,93]. This surprising result is possible because of the combined action of the SOS's catalytic and the allosteric binding sites[134]. The allosteric binding site can serve to anchor SOS to the membrane surface, while spurring nucleotide exchange of many Ras proteins at the catalytic site. Therefore, these two domains alone are able to stably recruit SOS to the membrane and enable processive activation of Ras. It has been shown that tethering SOS to the membrane is sufficient to activate the Ras pathway[168]. Therefore, processivity could play a crucial role in signal amplification and the determination of cell fate[59,134]. Thus, SOS displays two activation pathways: 1) the textbook receptor-mediated signaling initiation pathway through GRB2 recruitment of SOS (**Fig 4.3a**), as well as 2) a non-mediated positive feedback pathway where SOS recruits directly to pre-activated Ras (**Fig 4.3b**).

Mutations in SOS are known to impact the Ras signaling cascade, such as in Noonan syndrome[103]. Therefore, SOS remains an appealing target to modulate Ras activation. The largest

focus of previous work has been on the catalytic activity of SOS – its ability to switch into a highly active state, dependent upon the nucleotide state of the allosterically bound Ras. However, SOS recruitment could itself provide an important step in regulating this signaling pathway, especially if both recruitment pathways could be targeted simultaneously. Decreased recruitment of SOS would decrease the resultant Ras signal.

The small molecule inhibitor DCAI is known to bind in the Ras-SOS catalytic binding site, and to impede SOS mediated activation of Ras[109]. However, previous studies exploring the activity of DCAI have used Ras in solution—and therefore may not apply to the physiologically relevant membrane environment[153]. A membrane mimic is required to meaningfully distinguish protein recruitment from catalytic activity. In solution assays, SOS binding to Ras is convolved with exchange rates. Here, using combined in vitro and live-cell imaging assays, we show that DCAI action is mediated through reduced recruitment of SOS to Ras at the catalytic site. Not only does DCAI impede recruitment in the in vitro context, but is also able to reduce receptor-mediated SOS recruitment. Reducing SOS recruitment alone is shown to activation of the Ras pathway. More fundamentally, these results suggest that GRB2-mediated recruitment of SOS involves a Ras-binding step. Recent data from our lab indicate that receptor-mediated SOS recruitment involves a seconds-long activation lag-time (unpublished result); this time could be sufficient for SOS to bind (or fail to bind) to Ras.

A supported lipid membrane platform that was functionalized with H-Ras (noted as Ras throughout) through maleimide chemistry was used, mimicking Ras tethered to the membrane through the native farnesyl moiety[60,134]. Bilayer quality was assessed before each experiment using Fluorescent Recovery after Photobleaching (FRAP). Using a commercially available stop/flow chamber controlled by pump for an consistent pressure and exposure profile, SOS-Atto647 was added. SOS's catalytic domain (including both REM and CDC25) was used in order to maximize SOS action in the absence of autoinhibition, simulating an overactive state. Fluorescent signals were used to monitor SOS interactions with Ras (**Fig 4.1**).

When exposed to a Ras bilayer in the absence of nucleotide, SOS binds to Ras, begins the catalytic process, and is trapped stabilizing the nucleotide-free state[188]. Fluorescent intensity was used to determine the amount of time-integrated SOS recruitment (**Fig 4.1a**). As compared to a control with DCAI, there was a 40% decrease in SOS recruitment in the presence of 250uM DCAI (**Fig 4.1b**). This held both in wild type (WT) Ras and in Ras-Y64A, a mutation which abolishes SOS binding to the catalytic site. As expected, the overall recruitment of SOS to Ras-Y64A bilayers is much less than to WT bilayers, since the catalytic site contributes to SOS recruitment in the wild type case; this mutation then suggests the lower limit of sensitivity of this assay. Titrating the concentration of DCAI reproduces the effect curve that was previously reported[109], suggesting that the reduced binding between SOS and Ras is the main mechanism of DCAI inhibition. DCAI also modulates the membrane bilayer itself (**Figs 4.4-4.6**), potentially complicating the interpretation of live-cell measurements—but more importantly, setting the expectation for spontaneous transport through the cell membrane.

Even though the overall level of SOS recruitment to Y64A Ras is quite low, SOS binding is decreased further in the presence of DCAI. The preservation of the DCAI-mediated reduction of SOS recruitment to catalytically-incapable Ras would seem to indicate that DCAI primarily targets the Ras-SOS allosteric interaction. However, given the structural evidence that DCAI impedes SOS binding to the catalytic site[109], the simplest interpretation is likely misleading. It is well understood that both catalytic and allosteric sites are required for robust SOS activation[62,116,134]. One possible explanation of these results is that the Y64A mutation allows for some small amount of SOS binding even at the catalytic site, which is further reduced by the presence of DCAI in an additive way. Alternatively, it is also possible that DCAI has an effect on allosteric binding that is not predicted by structural studies, and that inhibition of SOS binding at both sites plays an important role in the loss of activity caused by DCAI.

In order to assess the impact of DCAI directly on SOS in live cells, MDAMB231 cells were transfected with full length SOS-GFP and were exposed to DCAI. Recruitment of SOS to the membrane is decreased with increasing DCAI concentration (**Fig 4.2**), consistent with the in vitro measurements. After EGF exposure, the fluorescent EGF can be seen bound to the cell membrane and colocalized with SOS-GFP (**Fig 4.2b, yellow arrows**). The degree of EFG binding was not significantly perturbed by DCAI-mediated membrane disruption (**Fig 4.7**). This strongly suggests that recruitment is the key mechanism of DCAI action even in the more complex live cell environment. Further, this demonstrates that DCAI has an impact on full-length SOS; the additional membrane interacting domains on SOS, and the full activating complex with GRB2, are not able to compensate for the inhibition of allosteric Ras-SOS binding. As in the in vitro measurements, DCAI has a notable impact on the lipid membrane of the cell, resulting in a phenotype of less adhesion and a pocked surface appearance, likely due to a changed membrane tension (**Fig 4.8**). The impact of DCAI in live cells matches that in vitro (**Fig 4.2c**). This supports a model of receptor-mediated SOS recruitment that includes a verification step, where SOS is stably localized at the membrane only after binding to Ras.

An activation lag-time between SOS binding to GRB2 and Ras activation (unpublished result) permits SOS to respond to a Ras drug even in the presence of the Ras activating cascade. Such a proofreading step provides an explanation of the efficacy of DCAI on preventing SOS recruitment of even full-length SOS in a live-cell environment. A reduction of SOS binding to Ras at the catalytic site, with potential reduction at the allosteric site in addition, would prevent activation by modulating the SOS binding kinetics, likely leading to a failure to overcome the necessary wait-time check-point (**Fig 4.3c**). As SOS allosteric binding and membrane localization leads to a built-in positive feedback loop upon the relief of autoinhibition[62], preventing SOS recruitment could stop a signaling cascade by interfering with this positive feedback (**Fig 4.3d**). A drug that can halt the recruitment of the effector SOS to Ras could have a significant impact in clinical settings. The mechanism of interaction utilized by DCAI, blocking the recruitment of SOS to the membrane, could provide a novel way of targeting Ras-driven disease states.

Supported lipid bilayers have been widely used in the academic context, but could also provide utility in industry in combination with live cell measurements, as demonstrated here. The SLB platform provides a straight-forward technique to uncover the mechanism of drugs and effector proteins in a physiologically relevant membrane environment, and when used in combination with single-cell imaging, can provide a complete picture of a drug's mechanism in a signaling pathway.

METHODS

Protein purification and labelling

H-Ras$^{C118S\ C181}$ (residues 1-181 with a Cys addition for coupling to the bilayer), called Ras throughout, and SOS-Cat Cys-lite (residues 198-1049 with four mutations: C838A, C615A, C980S, and E718C) were expressed and purified as previously reported[38]. SOS was labelled by incubating with Atto 647N-meleimide for 2h at room temperature, and non-reacted dye was removed using a PD10 column purchased from GE Healthcare as previously reported[134].

Ras-functionalized supported lipid bilayers

Bilayers were made from Egg-PC – 99% purity (93.99%), DOPS (3%), MCC-DOPE (3%), and TR-DHPE (0.01%). All lipids were purchased from Avanti Polar Lipids (Alabaster, Alabama). Lipids were mixed in a piranha-etched round bottom flask and the chloroform was evaporated using a rotovap with a 40°C bath for 30 minutes, and then was put under nitrogen for at least 10 minutes. Lipids were then rehydrated with ultra-pure water, sonicated with a Sonics Vibra-Cell to achieve single unilamellar vesicles (SUVs), and spun down at 15000rpm at 4°C for at least 20 minutes in an Eppendorf Centrifuge 5424 R. #1.5 glass slides were etched with piranha for 10 minutes within an hour of bilayer assembly and attached to an Ibidi sticky-Slide VI$^{0.4}$ (Cat# 80608) chamber. Lipids were mixed with concentrated PBS stock to achieve a 1x PBS final concentration, and added to the chamber for a 30 min incubation. Defects in the bilayer were blocked with 2.5mg/mL casein for 10 minutes, and then Ras was attached to the bilayer using maleimide chemistry. 0.5mg/mL Ras was incubated on the bilayer for 2.5 hours. Unreacted maleimide lipids were reduced with 10mM BME for 10 minutes. Dark nucleotide was provided in excess (at least 10uM) overnight to allow for Ras nucleotide exchange. All measurements were made in Reaction Buffer (40mM HEPES, 100mM NaCl, 5mM MgCl, pH 7.4, 10mM BME).

SOS recruitment assay

Ibidi chambers were connected with tubing, male and female luer-lock connectors, and valves, ensuring no bubbles entered the chamber. Using an additional length of tubing, a syringe was connected to the valve and attached to a syringe pump (Harvard Apparatus 11plus, Cat# 70-2208) to maintain a steady, consistent flow profile during the experiment. All tubing connections were kept the same length in all experiments. 200uL of a desired concentration of SOScat was

injected into the Ibidi chamber well using a valve and a 1mL luer lock syringe. SOS injected occurred while data was being collected, to ensure the capture of the initial time point measurements. The SOS pulse was followed with 1mL flow at a 1mL/min flow rate. During imaging, 20 frames were captured at any location before stepping down one frame-width to minimize the effects of photobleaching and other photo-effects. All injections were diluted into Reaction Buffer (composition listed above).

Cell transfection
Four days before imaging, MDAMB231 cells were plated on TC-treated 6-well dishes at around 50% confluency. The next day, the cells were transiently transfected with a full-length SOS plasmid with GFP attached at the C-terminus (FL-SOS-GFP). Cells were either transfected with 1ug of FL-SOS-GFP DNA with either 4 ug of PEI in OptiMEM or with 5 uL of Lipofectamine 2000. Transfection efficiency and cell health looked similar in both conditions. After 5-6 hours, the media was changed to fresh DMEM. The following day, the transfected cells were replated on #1.5 glass slides. The day before imaging, cells were starved with DMEM – serum overnight.

Cell imaging
Cells were imaged in a 37C imaging chamber. Multiple cells were found on each glass side; TIRF images were taken before adding DCAI or a DMSO control, after a 10-minute incubation period, and during stimulation with a final concentration of 100ng/mL of EGF-Atto647. The concentration of DCAI or DMSO was kept consistent in all steps after the initial image, ranging from 0uM – 250uM DCAI.

TIRF microscopy
Images were taken on a Nikon microscope (Nikon Eclipse Ti (Ti HUBC/A), Technical Instruments, Burlingame, CA)with a Nikon Apo TIRF 100x/ 1.49 oil objective and an Andor EM-CCD camera (iXon ultra 897, Andor Inc., South Windsor, CT), as controlled by micro-manager2. Coherent's OBIS lasers were used (488, 561, and 647), along with Chroma emission filters for each matching line. A Nikon Intensilight C-HGFIE lamp was used for RICM and bright field imaging.

Imaging analysis
All images were analyzed using FIJI software from the ImageJ software family. For SLB data, an initial average shade correction was applied to all images, and then the peak intensity was found. The average intensity from that peak recruitment timepoint was then calculated, avoiding DCAI defects when relevant. For live cell data, the cell outline was found. Then, the total area of membrane surface with SOS recruitment above that threshold was integrated both before and after EGF activation, and the final level of SOS recruitment was divided by the initial level of SOS present on the membrane to control for transfection efficiency variance. High-expressing cells were excluded. 14 cells were imaged with both 0uM DCAI and 250uM DCAI; 6 cells were imaged with 125uM DCAI (shown in supplement).
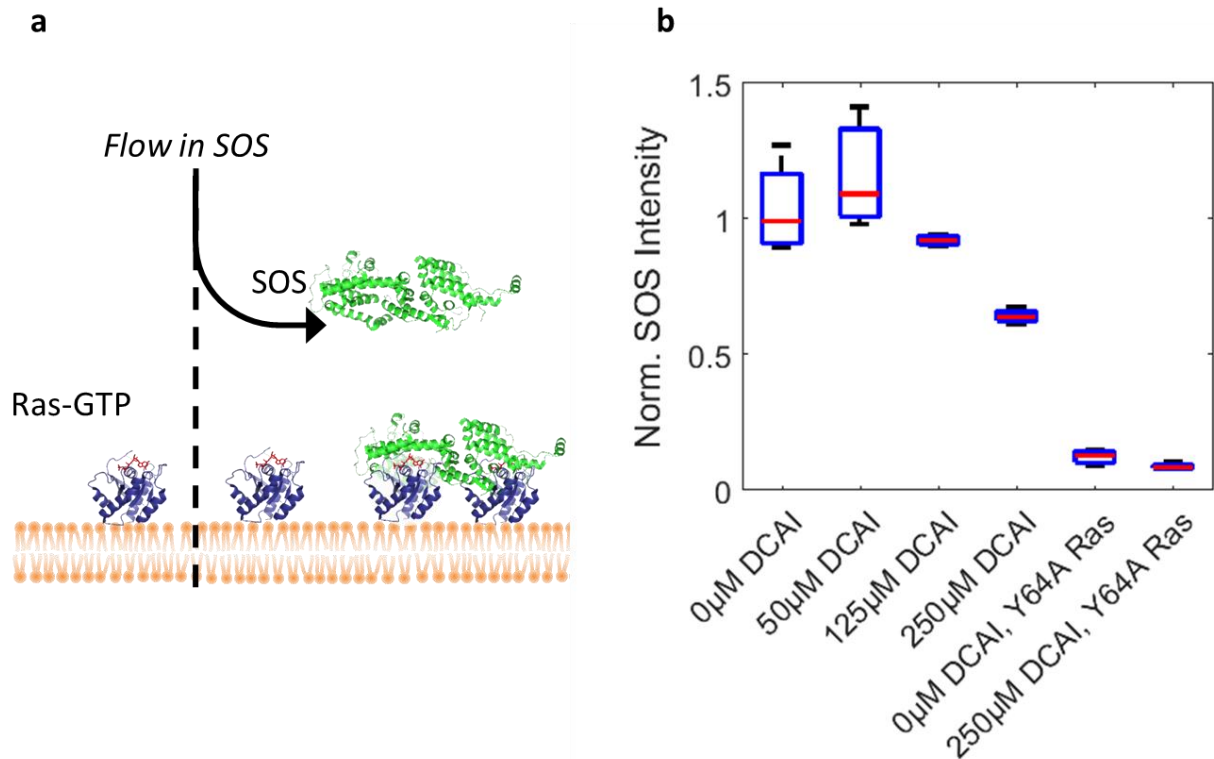
Figure 4.1. Output information of the SOS recruitment assay. DCAI reduces SOScat recruitment to Ras in the lipid membrane context. This platform enables recruitment and activation measurements of lipid-interacting enzymes, such as SOS to Ras. (**a**) Recruitment of SOS to the membrane can be measured upon flowing in SOS to a Ras-decorated bilayer using a controlled pulse of protein and buffer through the chamber. (**b**) Recruitment data for a titration of DCAI exposures. Ras-Y64A has a catalytic site mutation that permits only allosteric SOS binding. DCAI reduces SOS recruitment by about 40%, with confidence of $P > 0.05$. Altering [DCAI] produces a titration curve of SOS recruitment.
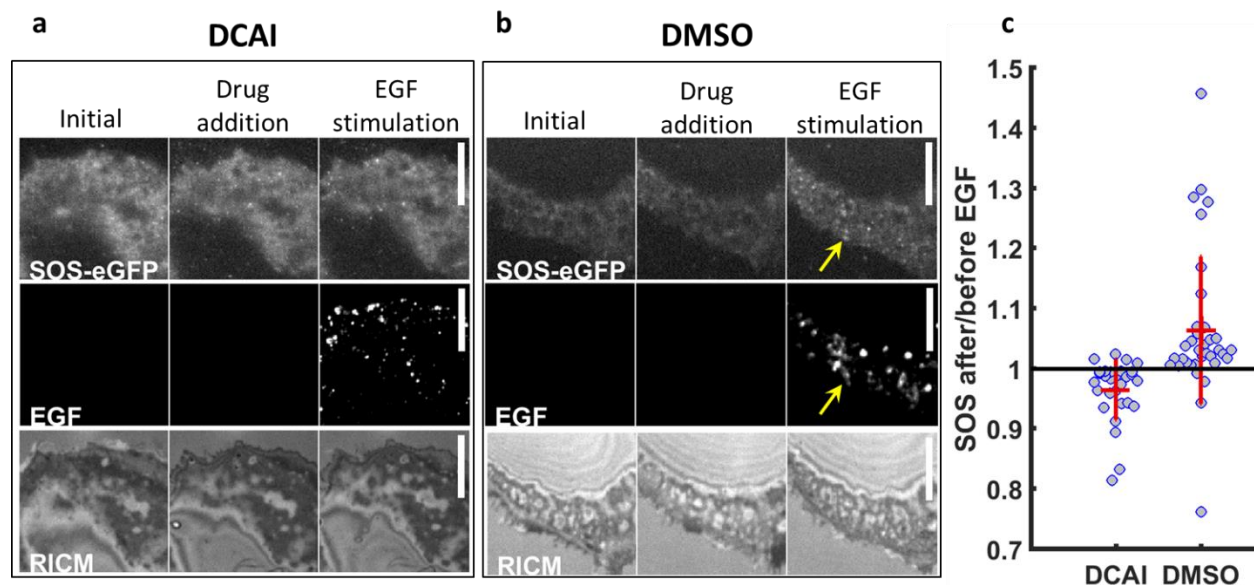
Figure 4.2. DCAI suppresses SOS recruitment in starved, activated MDAMB231 cells. **a/b** RICM and TIRF imaging of cells MDAMB231 cells transfected with full length SOS-GFP before and after activation with fluorescent EGF. Top row: SOS-eGFP; middle row: EGF; bottom row: RICM. Cells were starved overnight and exposed to DMSO or the stated concentration of DCAI for 10 minutes prior to stimulation. Cells were exposed to (**a**) DCAI; (**b**) DMSO. **c** After/before EGF stimulation ratio of SOS recruitment to the membrane of activated MDAMB231 cells. Each circle represents one independent cell measurement. SOS recruitment was measured by identifying integrating SOS intensity on the cell membrane.
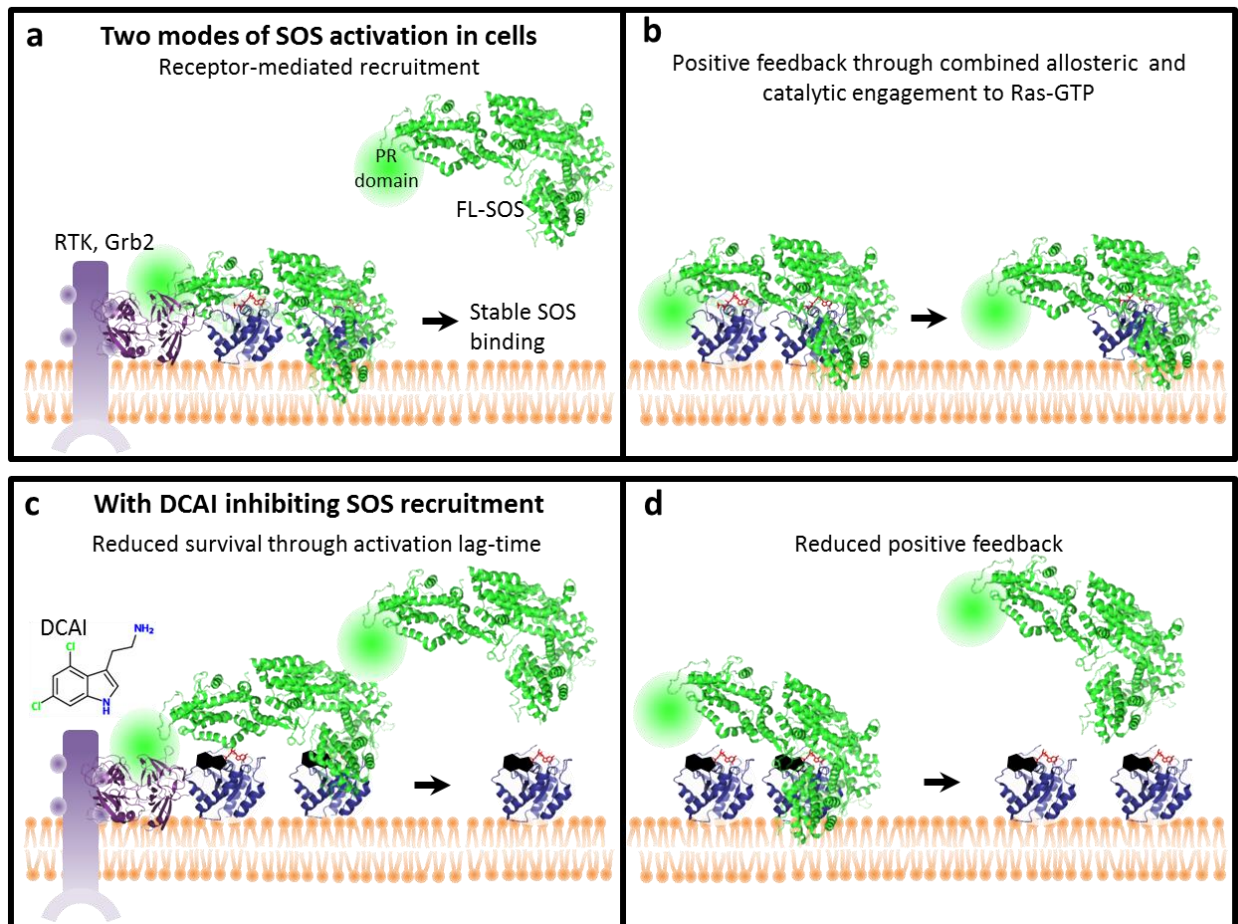
Figure 4.3. Schematic depiction of the two modes of Ras activation by SOS, with the perturbations caused by DCAI. Ras/SOS signaling in an activated cell. There are two modes of SOS recruitment: (**a**) one through the signaling cascade leading up to Grb2-mediated recruitment of SOS through the PR domain; and (**b**) a second through direct SOS binding to Ras through positive feedback, once a pool of Ras-GTP has been formed through receptor-mediated activation or other GEF activity. (**c/d**) DCAI reduces recruitment to the allosteric binding site, reducing Ras activation at both steps. (**c**) SOS recruitment is reduced even in the presence of upstream effectors, suggesting that SOS binding to Ras is an important stabilization step in receptor-mediated recruitment. Further, combined catalytic and allosteric binding of Ras to SOS is required for full activation of SOS, so even through receptor-mediated recruitment, reduced binding to either site would reduce catalysis. (**d**) The positive feedback loop of SOS activation would be reduced in cells by alleviating SOS recruitment to either the catalytic site or the activating allosteric site, as both are required for processivity.
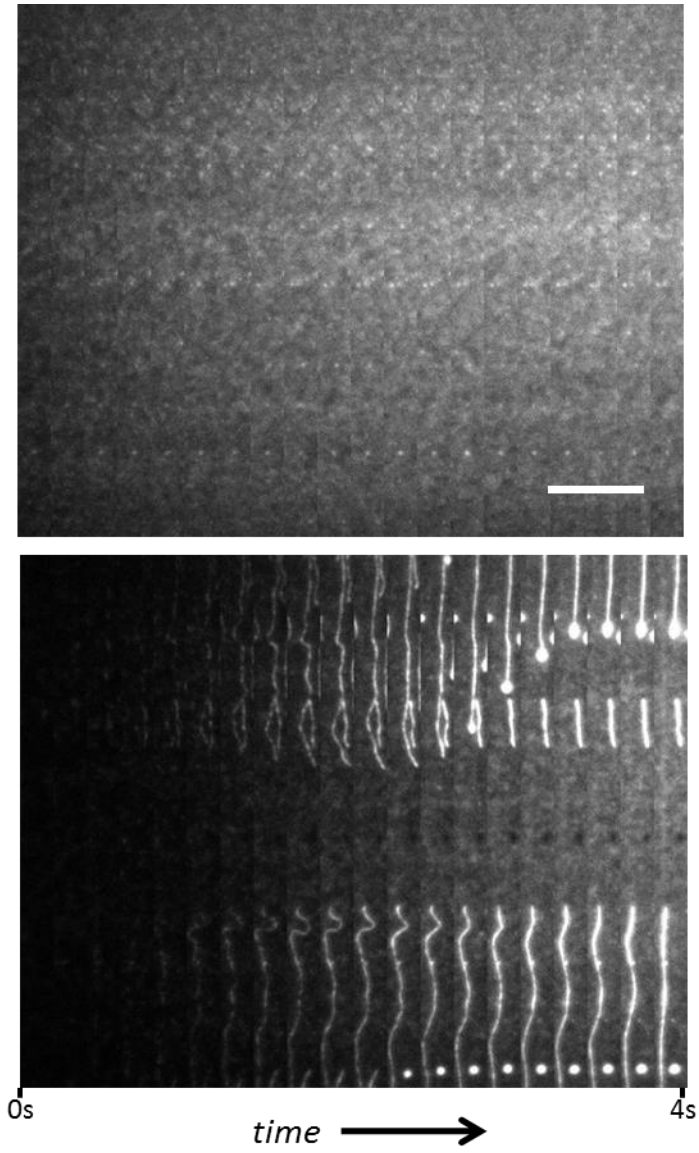
Figure 4.4. DCAI interacts with the bilayer (DMSO, top; DCAI, bottom). Kymograph of SOS channel displayed, 200ms between frames. Scalebar 1μm.
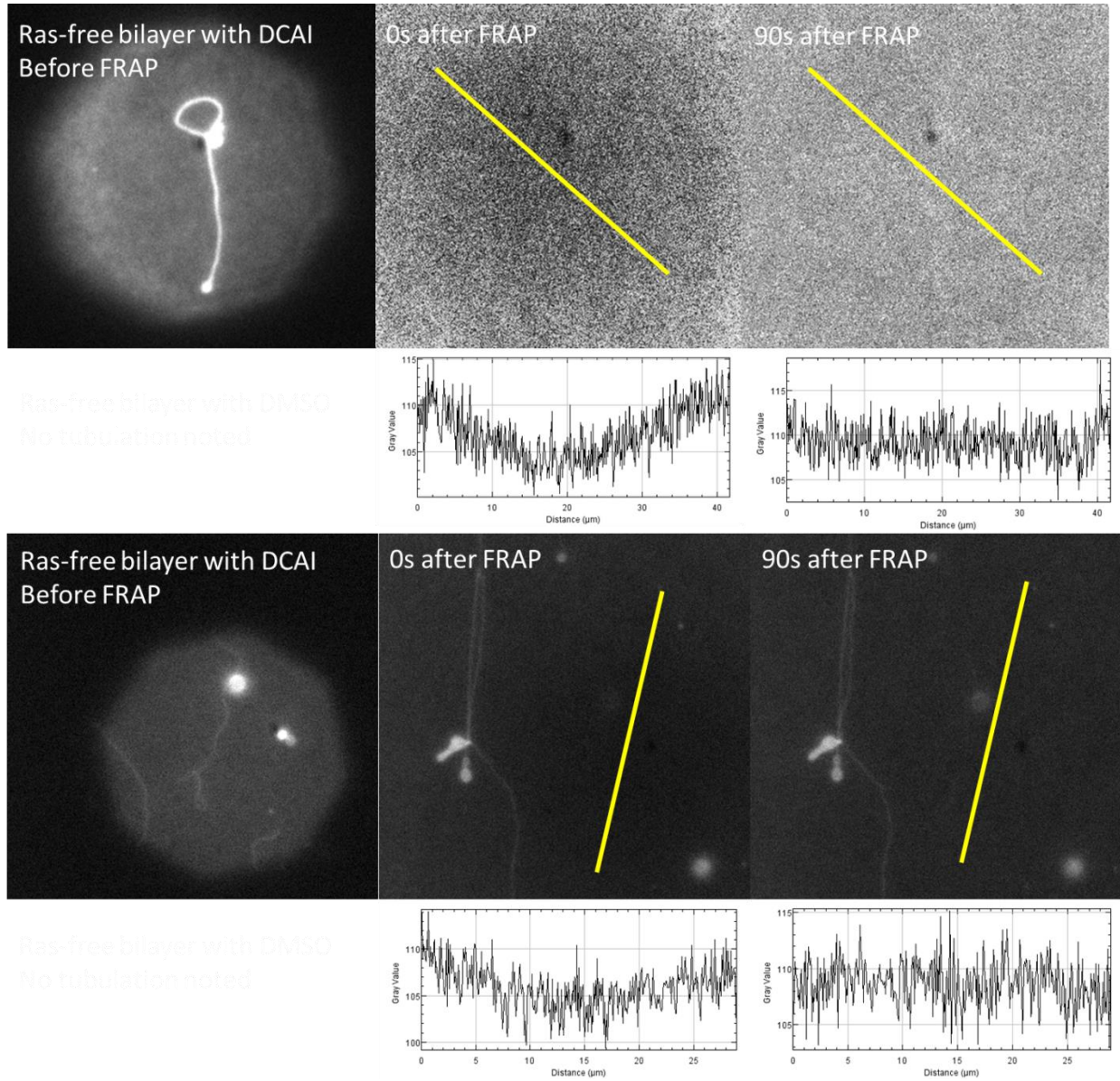
Figure 4.5. DCAI interacts with the bilayer. DCAI-caused tubules are diffusively distinct (top), and are themselves mobile (bottom).
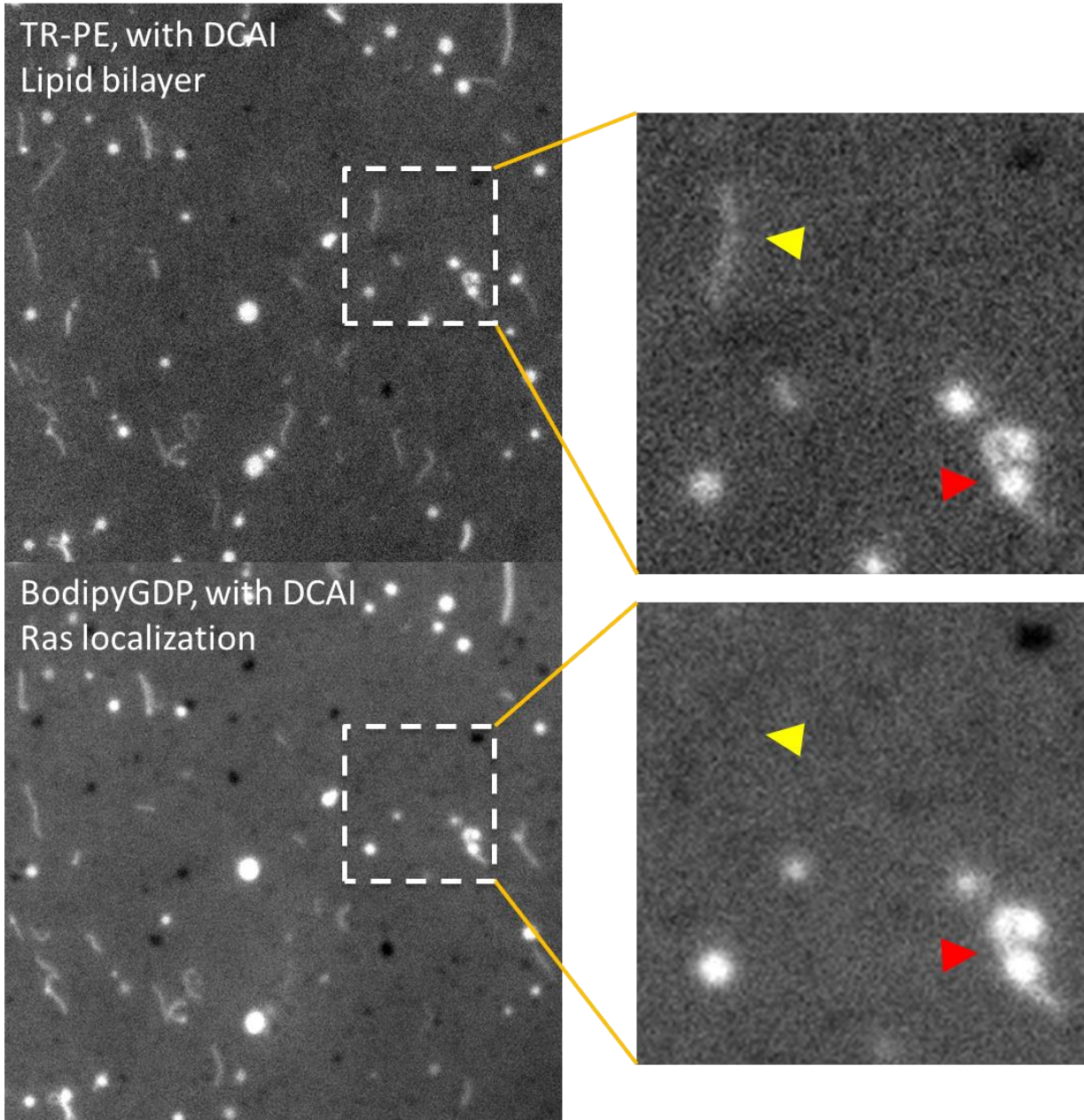
Figure 4.6. Ras is not enriched on all tubules. This suggests that tubulation is caused by a membrane effect, not by Ras.
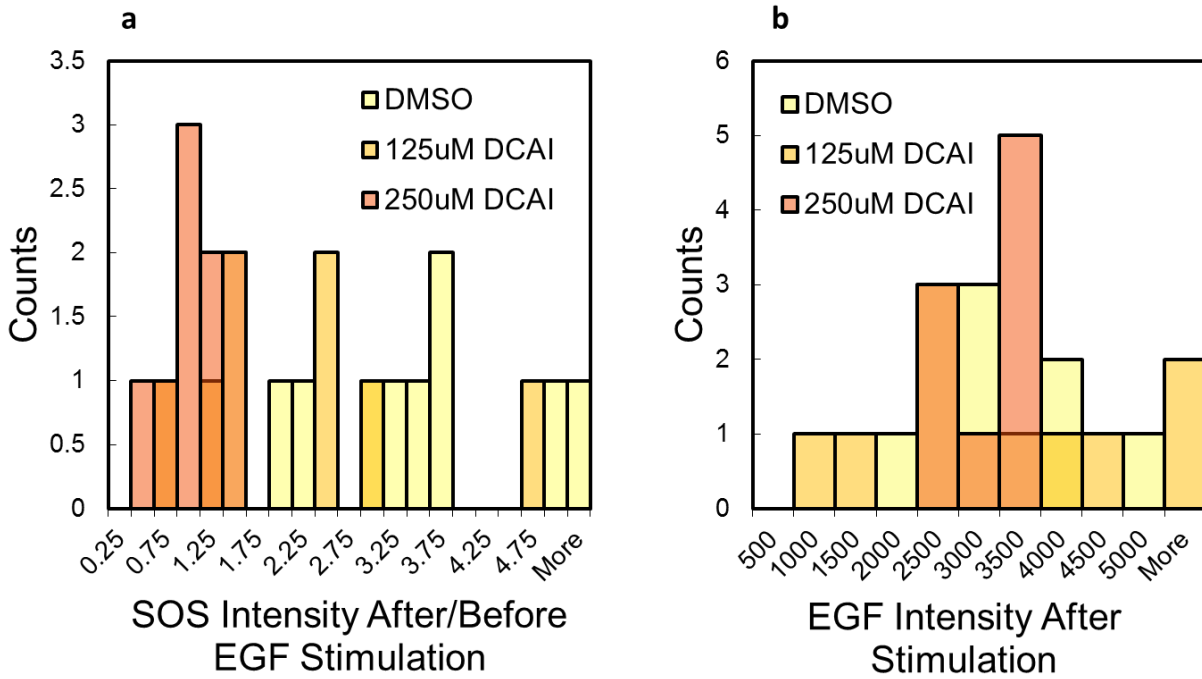
Figure 4.7. DCAI suppresses SOS recruitment in starved, activated MDAMB231 cells. (**a**) Distribution of intensity ratios for TIRF SOS channel after/before stimulation with EGF. Note that the distributions are distinct for all three DCAI concentration conditions (with DMSO as the control). Cells were starved overnight and exposed to DMSO or the stated concentration of DCAI for 10 minutes prior to stimulation. (**b**) Distribution of EGF intensity after stimulation for all measured cells. Note that the distribution of EGF intensity is not distinct for the DCAI conditions. Therefore, even though DCAI does perturb cell morphology, EGF has equal binding access to cells in all conditions.
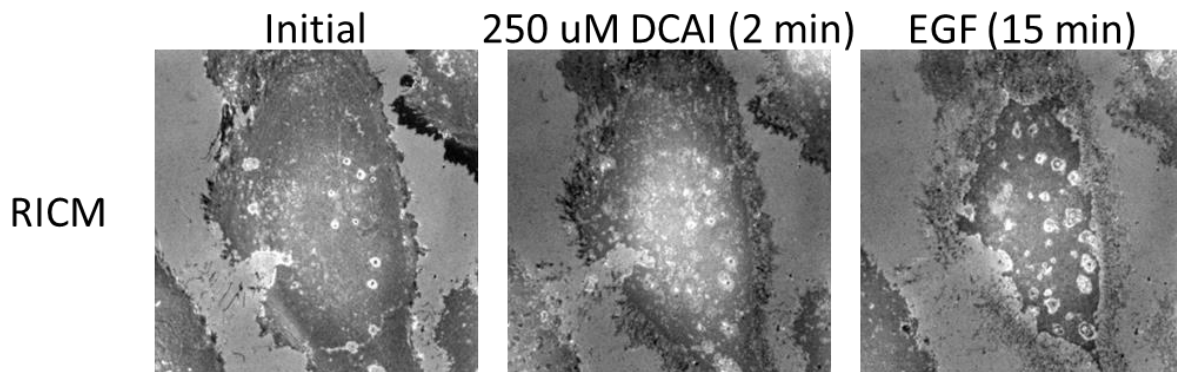
Figure 4.8. Membrane perturbations caused by DCAI are clearly visible in cells. Note here a typical cell that dramatically shrinks its adherent zone after DCAI addition, and even more so after the addition of EGF with more DCAI. This is likely caused by a change in membrane tension.

CHAPTER 5.

ONCOGENIC RAS MUTATIONS IMPACT SOS RECRUITMENT AND ALLOSTERIC SENSITIVITY

Meredith G. Triplet[§], Emily C. Laubscher[§], Shalini T. Low-Nam[§], Jay T. Groves[§].

§Department of Chemistry, University of California, Berkeley, CA 94720, USA.

AUTHOR CONTRIBUTIONS

ACKNOWLEDGEMENTS

ABSTRACT

While Ras oncogenesis is widely understood to be caused by modulations of hydrolysis and intrinsic nucleotide exchange, secondary impacts of Ras oncogenic mutations on SOS activity have not been deeply explored. Here, we quantitatively measure the impact of oncogenic Ras mutations on time-integrated SOS recruitment and SOS-mediated Ras nucleotide exchange rates. We demonstrate that SOS recruitment is increased to Q61L-Ras and to G13R-Ras, while the catalytic rate of nucleotide exchange is decreased to both Q61L-Ras and G12V-Ras. This suggests that SOS activity is modulated by Ras mutations, and provides insight into new mutation-specific therapeutic drug targets.

INTRODUCTION

The GTPase Ras is a highly regulated signaling hub whose activation leads to a wide range of cell responses, including cell growth and proliferation[36]. Ras binds to the nucleotides GTP and GDP with picomolar affinity[50]. The nucleotide state results in shifts in the Switch 1 and Switch 2 regions of the protein (**Fig 5.1a**), causing conformational states that can be sensitively detected by Ras effectors. The GTP-bound state of Ras is active, recruiting downstream signaling proteins, while the GDP-bound state is inactive. Once activated, Ras behaves as a "loaded spring" that can deactivate via GTP hydrolysis[189]. Deactivating pressures in an inactivated cell keep a majority of the Ras population GDP-bound, preventing spurious activation[190].

As the intrinsic rates of Ras hydrolysis and nucleotide exchange are low, Ras depends on signaling partners to catalyze both of these reactions and to properly regulate its nucleotide state. Guanine nucleotide Exchange Factors (GEFs) catalyze the release of bound nucleotide for exchange with cytosolic GTP, while GTPase Activating Proteins (GAPs) catalyze the hydrolysis of the bound GTP[99,189,191]. Many structural features are preserved among the many existing GEFs and GAPs. GEFs stabilize the nucleotide free confirmation of Ras by replacing the bound Mg^{2+} and shifting the switch regions[187]. GAPs provide charge stabilization of the hydrolysis transition state to dramatically increase the slow rate of native Ras hydrolysis. A GAP "arginine finger" inserts into the Ras catalytic site and complexes with the negatively charged cleaved phosphate intermediate[192].

If Ras experiences an over-activating mutation, then oncogenesis is likely. Ras mutations cause 30% of human cancers and are especially prevalent in colorectal and pancreatic cancers[51]. Unsurprisingly, Ras and its regulatory partners are prime targets for drug-discovery research. While some drug strategies have garnered preliminary enthusiasm, Ras has been deemed "undruggable" and no Ras drug has yet survived to market[50]. It is probable that a combination of drugs will be required to impede the growth of Ras tumors, as this protein regulates many interconnected pathways[190].

Oncogenic Ras mutations perturb its signaling switch behavior such that the GTP-bound population of Ras is increased. These mutations either increase nucleotide exchange or decrease GTP hydrolysis, leading to over-activation of the proliferatory pathway. The most common oncogenic Ras mutations occur at codons 12, 13, and 61[51]. Mutations at all three sites lower hydrolysis rates, but G13 is notable for its role in nucleotide exchange (**Fig 5.1b**). Q61 aids in charge stabilization of the γ-phosphate of GTP as it is hydrolyzed. Additionally, Q61 hydrogen bonds with the GAP arginine finger such that the transition-state mimic is formed. The Q61L replacement both fails to mitigate negative charge during intrinsic hydrolysis and prevents GAP-mediated rate enhancement during GTP hydrolysis[51]. Similarly, mutations of both G12 and G13 can interfere with GAP activity, as both codons come into close contact with the arginine finger. Some residues at these locations – including G12V and G13R – clash with the arginine finger,

75

reduce GAP binding, and are GAP-insensitive[51,52]. More importantly for G13 mutations, however, is the drastic increase in nucleotide exchange. In a solution-based NMR study, intrinsic nucleotide change was 15-fold faster for the highly active G13D, but only 2.4-fold faster for Q61L, and reduced by 1.8-fold for the G12V mutation[53].

In addition to the main mechanisms of oncogenesis just described, Ras interactions with other regulatory proteins – such as GEFs – might also be perturbed by these mutations. Understanding secondary reactions that contribute to Ras deregulation could yield important insights in the discovery of clinically successful drug cocktails.

The most studied Ras GEF is Son of Sevenless (SOS). SOS binds two Ras molecules in its allosteric and catalytic sites. Binding at the catalytic site exchanges the Ras-bound nucleotide for one in the cytosol – which, due to its higher concentration, is likely GTP. The allosteric site binds stably to Ras, allowing the catalytic site to processively activate all of the Ras in the vicinity. Without free nucleotide in solution, SOS will become trapped on the membrane, unable to complete nucleotide exchange[134]. Our time-integrated SOS recruitment utilizes this fact to quantify varying amounts of SOS catalytic engagement for different Ras mutations (**Fig 5.1c**).

The allosteric site of SOS has a higher affinity for Ras-GTP than Ras-GDP, creating a positive feedback loop in which catalytic activity of SOS on Ras leads to more SOS recruitment. The most common SOS-Ras interaction is short-lived (unpublished result), but the long-lived events lead to the activation of thousands of Ras molecules, caused by a stably recruited, highly processive SOS molecule[116]. These behaviors may contribute to the ability of Ras to integrate analog signal input to a switch-like digital signal output[59].

To prevent spurious Ras activation, SOS is highly autoinhibited. It binds Ras by its catalytic core, which consists of the REM and CDC25 domains, together known as SOS^{cat}. Its N-terminal domains, the Dbl homology (DH), pleckstrin homology (PH), and histone-fold (HF) domain are involved in the autoinhibition of SOS. The histone packs against the PH-Rem linker to occlude the allosteric binding site[61]. However, the PH and histone domains can have their autoinhibition relieved by contact with PIP$_2$ and charged lipid, respectively[61]; in fact, these membrane interactions result in upregulation of signaling[134]. The C-terminal PR domain also plays a role in autoinhibition[62]. As SOS interacts with Ras only at the catalytic core REM and CDC25 domains, oncogenic mutations are expected to have no impact on SOS autoinhibition. Therefore, the SOS used herein consists only of the catalytic core of the protein, SOS^{cat}, and is referred to as SOS throughout.

Herein, we utilize a time-integrated SOS recruitment assay and a SOS-mediated catalytic exchange rate assay to explore the impact of oncogenic Ras mutations on SOS binding and activity. Ras is covalently tethered to a supported lipid bilayer (SLB) and SOS molecules are introduced in solution (**Fig 5.1c**, Methods). In the absence of free nucleotide in solution,

molecules of SOS become trapped in the nucleotide-free Ras/SOS transition state, unable to complete the nucleotide exchange. This allows us to effectively integrate SOS recruitment over time, as each catalytic Ras/SOS binding event is preserved, with the readout of increased fluorescence intensity (**Fig 5.6a**). Moreover, we observe the catalytic rate of SOS by pre-loading Ras with fluorescently labelled nucleotide, and watching the signal decay over time upon the addition of SOS (**Fig 5.6b**). In order to prevent the GTPase activity of Ras from cleaving the γ-phosphate, the non-hydrolyzable analog GppNp was used (referred to as GTP throughout). These assays were reproduced for WT, G12V, G13R, and Q61L Ras mutations.

RESULTS

Bilayer mobility was confirmed for each sample (**Fig 5.5**). As fluorescently-labelled SOS was added to the Ras-tethered supported lipid bilayers under continuous flow of buffer, the concentration of SOS in the chamber changes over time. This was quantified with Epi-fluorescence, as this imaging technique images all fluorophores in solution. In contrast, TIRF imaging focuses only on those fluorophores at or near the surface, within 100-200nm. The SOS pulse profile was quantified using Ras-free bilayers (**Fig 5.2**). In the conditions used, the chamber was exposed to high concentrations of SOS for approximately 20 seconds. In the absence of Ras, minimal SOS persists after the initial flow, verifying that the SOS surface interaction is Ras dependent. The recruitment assay is focused on the success of an initial encounter between SOS and Ras, which artificially traps SOS in the transition state. All SOS not stably bound to Ras through the allosteric site, or trapped in the middle of its catalytic exchange, is removed with the buffer flow[60,134].

This bulk recruitment assay is able to distinguish between the GDP and GTP bound states of WT Ras (**Fig 5.3a**). This is consistent with our current understanding of SOS activation: SOS first interacts with the bilayer through allosteric sampling, and an engagement with Ras-GTP at the allosteric site opens up the catalytic pocket for a Ras engagement at the active site. This activation process is completed in seconds. Ras-GDP spurs some catalytic activity of SOS, but only approximately half of that to Ras-GTP. This modulation of Ras-SOS interaction in a GDP-dependent fashion is consistent with previous structural and quantitative binding results[62,152]. Note further that SOS has greater-than-baseline activation to apo-Ras (nucleotide free), but this recruitment is substantially less than the even non-activating Ras-GDP case – only about a quarter of that to Ras-GTP (**Fig 5.3a**).

SOS recruitment to oncogenic mutations at the three most prevalent codons were explored with this assay, and mutation-specific SOS-binding sensitivities were discovered. Time-integrated SOS recruitment is highest for Q61L, similar to WT for G12V, and much decreased to G13R (**Fig 5.3b,c**). These trends held for both GTP and GDP. However, the G12V mutation might

decrease allosteric sensitivity of SOS to the nucleotide state; note that the G12V-GDP recruits SOS slightly more than the WT case, while G12V-GTP recruits slightly less than the WT case.

Accurate interpretation of G13R Ras recruitment requires a careful consideration of this construct's nucleotide state. As has previously been demonstrated, G13 mutations undergo rapid intrinsic exchange (**Fig 5.1b**). Such rapid exchange has been confirmed herein, as any loaded fluorescent nucleotide is quickly washed away, making the catalytic exchange assay impossible. G13R binds anomalously little SOS, about 10-fold less than wild type Ras; however, much of this trend is likely due to G13R being in the apo state, which recruits substantially less SOS even in the WT case (**Fig 5.1a**). However, its fast nucleotide release rate does not completely explain its lack of affinity for SOS, because – assuming total absence of nucleotide in both cases – SOS recruits to G13R 2.5-fold less than to WT. This result is especially surprising, as G13R is not considered to play a role in Ras/SOS binding.

The catalytic rate of SOS on these Ras mutations (excepting G13R) was also measured. In this assay, the concentration of SOS was lowered and was kept consistent throughout data collection. The photobleaching of fluorescent nucleotide while imaging at one position was assessed, along with the intrinsic exchange rate of Ras when exposed to dark nucleotide in the absence of SOS (**Fig 5.4a**). This data shows the baseline sensitivity of this assay for WT Ras. As seen in time-integrated SOS recruitment, SOS showed higher catalytic activity for Ras-GTP than for Ras-GDP. Q61L Ras shows catalytic exchange rates comparable to wild type Ras despite a demonstrated increase in time-integrated SOS recruitment. G12V Ras on the other hand shows decreased catalytic activity, despite comparable SOS recruitment for this Ras mutation (**Fig 5.4b**). This shows that SOS binding and SOS catalytic rates are both independently impacted by SOS mutations. Individual traces are shown in **Fig 5.7**.

DISCUSSION

The combination of time-integrated SOS recruitment and catalytic rate assays provide a complete picture of the interaction of SOS with Ras. In the absence of nucleotide, each SOS-mediated Ras activation event is trapped and captured, as this protein pair is locked in a nucleotide-free transition state. While this first assay enables us to account for every Ras/SOS interaction, the time integration inherently prevents assessment of the catalytic rate. Therefore, a second assay using a smaller concentration of SOS in the presence of nucleotide in a steady-state measurement can fill in the kinetic gaps.

While the mechanisms of Ras oncogenicity are well understood to be mediated by decreased hydrolysis, insensitivity to GAP, and increased nucleotide exchange[193], SOS might also play a unique role in modulated Ras activity in these disease state. Structurally, Q61 is within the Switch 2 region, part of the GEF binding interaction (**Fig 5.1b**). Therefore, an impact of Q61L

on SOS would be predicted. In contrast, as G12V and G13R are far from the GEF binding interaction, any impact on SOS recruitment is surprising. The minimal shift of G12V in SOS recruitment is therefore expected, but the dramatic impact of G13R requires some deep structural thought. It is possible that this mutation impacts Ras orientation on the membrane in such a way that SOS binding is somewhat occluded[194,195]. Further exploration of the impact of mutation-impacted membrane orientation is required.

Furthermore, the distinction between time-integrated SOS recruitment and catalytic rate is intriguing. This indicates that, upon SOS interaction with Ras, the rate of catalytic exchange has yet to be determined. Whether the differences in catalytic rate are caused by modulated probability of entering a highly active state, or changes in the rate of each catalytic event, has yet to be determined. However, given the rapid rate of each catalytic exchange event in comparison to the relative slow Ras/SOS interaction step, it is easier to imagine that modulation of catalysis occurs through a decreased probability of entering the highly active state. The fact that catalytic rate for both G12V and Q61L is slower than what might be expected opens the possibility that both of these mutations are less likely to promote SOS into its highly activated state. Since both of these mutations reduce intrinsic hydrolysis, perhaps a transition state of SOS with a hydrolyzing GTP at the allosteric site is the structural cause of highly activated, trapped SOS.

Although the exact mechanisms remain ambiguous, it is clear that oncogenic Ras has a distinct impact on SOS binding and catalytic rate. Such differences should be considered in future rational drug design.

METHODS

Protein purification and labeling
H-Ras$^{C118S, C181}$ (residues 1-181 with a single exposed cysteine for coupling to the bilayer), called Ras throughout, and SOS-Cat-Cys-lite (residues 198-1049 with four mutations: C383A, C615A, C980S, and E718C) were expressed and purified as previously reported[38]. SOS was incubated with Alexa647N-maleimide for 2 hours at room temperature, and non-reacted dye was removed with a PD10 column purchased from GE Healthcare as previously reported[134].

Cleaning
Round bottoms flasks used for lipid preparation were rinsed with isopropyl alcohol immediately after use and stored in a 50/50 mixture of isopropyl alcohol/water. Flasks were sonicated in this isopropyl alcohol/water mixture for 30 minutes and rinsed thoroughly with MilliQ water. Flasks were then piranha etched for 30 minutes, rinsed thoroughly with MilliQ water, and stored in a drying oven.

Ibidi chambers were soaked overnight in acetone to remove adhesive and the attached glass slide. The chambers were then sonicated for 30 minutes in each of the following solutions: acetone, 1% Hellmanex (Fischer, Cat# 14-385-864), isopropyl alcohol, isopropyl alcohol/water, and water. The chambers were rinsed thoroughly with MilliQ water between each sonication step and after the last step, were stored in MilliQ water in a beaker covered in parafilm (Heathrow Scientific, Cat# 152-68322-368).

Valves were rinsed thoroughly with isopropyl alcohol and then sonicated for 30 minutes in each of the following solutions: isopropyl alcohol, isopropyl alcohol/water, water. Valves were rinsed thoroughly with MilliQ between each sonication step and after the last step, were stored in MilliQ water in a beaker covered in parafilm.

Ends of tubing were rinsed well with isopropyl alcohol. Tubing was rinsed with flow of 5mL of isopropyl alcohol and 5mL MilliQ water. Tubing was spun dry before storage.

Glass slides are prepared for use by sonication in isopropyl alcohol for 30 minutes. Then slides are rinsed thoroughly in MilliQ water, piranha etched for 10 minutes, and rinsed again in MilliQ.

Ras SLB preparation
Lipids were prepared by mixing 93.990 mol% Egg PC lipids, 3 mol% MCC-DOPE lipids, 3 mol% DOPS, and 0.01 mol% Texas Red lipids in chloroform. All lipids were purchased from Avanti Polar Lipids (Alabaster, Alabama). The chloroform was evaporated on a Rotovap for at least 30 minutes and under flow of nitrogen gas for another 10 minutes. The lipids were rehydrated in MilliQ water with a vortexer. Small unilamellar vesicles (SUVs) were created by sonication with a Sonics Vibra-Cell on ice with a pulse of 20s on, 59s off for 100s total sonication. The SUVs were then spun down in a Eppendorf Centrifuge 5424R at 15000 rpm at 4°C for 30 minutes. 10X PBS (Mediatech In, Cat# 46-013-CM) was then added to the lipids for a final 1X concentration.

#1.5 glass slides were freshly etched before bilayer preparation and attached to an Ibidi sticky-Slide VI$^{0.4}$ (Cat# 80608) chamber. The chamber was hydrated with 1mL 1X PBS before 100uL of SUVs are flowed into the chamber and allowed to deposit for 30 minutes to self-assemble a SLB. Between each subsequent step the chamber was washed with 1mL 1X PBS. Defects in the SLB were blocked with 100uL 2.5mg/mL Casein for 10 minutes. Then, the SLB was functionalized with 100uL 0.5mg/mL Ras, which was incubated for 2.5 hours to allow the Ras to covalently link to the MCC lipids via maleimide chemistry. The MCC lipids were then quenched with 100uL 10mM BME for 10 minutes.

Samples were left overnight at 4°C. Chambers were washed with 40mM HEPES, 100mM NaCl, pH 7.4 (no MgCl$_2$). The nucleotide bound to Ras was removed with 100uL (conc.) EDTA for 20 minutes and washed with stripping buffer. The buffer was exchanged to 40mM HEPES, 100mM

NaCl, 5mM MgCl$_2$, pH 7.4, as the Mg^{2+} allows the Ras to bind a new nucleotide. Then, 100uL Atto488-GppNp (in a range of 1-10uM) was flowed into the chamber and allowed to bind for at least an hour. Ras loading is not dependent upon GppNp concentration in this range (unpublished data).

Time-integrated SOS recruitment assay
All imaging was performed with the sample in 40mM HEPES, 100mM NaCl, 5mM MgCl$_2$, pH 7.4, 10mM BME, 0.25mg/mL Casein. Lengths of tubing, valves, male and female luer-lock connectors, and Ibidi chamber were attached containing imaging buffer such that there were no air bubbles in the sample. An additional length of tubing was used to connect a 10mL syringe of imaging buffer to the valve. Just prior to imaging, the sample was rinsed with 1mL of imaging buffer by hand to remove free nucleotide. Imaging was started before the injection of SOS. 10 images in 647 channel and 1 image in 488 channel were acquired before moving down one frame width to minimize effects of photoeffects and photobleaching. This protocol was repeated at 20 positions. After the first frame was imaged, 200uL of 45nM SOScat, diluted in imaging buffer, was injected into the valve using a 1mL luer-lock syringe, followed by 1mL imaging buffer at a rate of 1mL/min using a syringe pump (Harvard Apparaturs 11plus, Cat# 70-2208) to ensure a consistent SOS pulse profile.

SOS catalytic rate assay
Immediately prior to imaging, samples were washed with 1mL imaging buffer by pipette in 5-200uL washes. Imaging was started before injection of SOS. 1 image in 647 channel and 1 image in 488 channel were acquired before moving down one frame width to minimize photoeffects and photobleaching. This protocol was repeated at 50 positions at an interval of 15 seconds. After the first frame was imaged, 200uL of 2nM SOS cat and 120uM dark nucleotide diluted in imaging buffer were injected by pipette.

TIRF microscopy
Images were taken on a Nikon microscope (Nikon Eclipse Ti (Ti HUBC/A), Technical Instruments, Burlingame, CA) with a Nikon Apo TIRF 100x/1.49 oil objective and an Andor EM-CCD camera (iXon ultra 897, Andor Inc., South Windsor, CT), as controlled by micro-manager2. Coherent's OBIS lasers were used (488, 561, and 647), along with Chroma emission filters for each matching line.

Imaging analysis
All images were analyzed using FIJI software from the ImageJ software family. For SOS images (imaged in 647), Gaussian blur of background intensity before the injection of SOS was subtracted from the sample acquisitions. A shade correction was applied to all images. The average intensity inside a square at the center of the image was taken to create the recruitment traces. The average of all frames after equilibration of SOS recruitment channel was then calculated, average with other samples, and used to create a schematic trace for clarity (**Fig 5.3**).

For nucleotide images (imaged in 488), a shade correction was applied to all images. The average intensity inside a square at the center of the image was taken to create the decay traces. The traces were normalized to the starting intensity and fit with exponential decay curves. The average exponential fit was calculated, and the exponential curve with this fit is displayed in **Fig 5.4**.

FIGURES
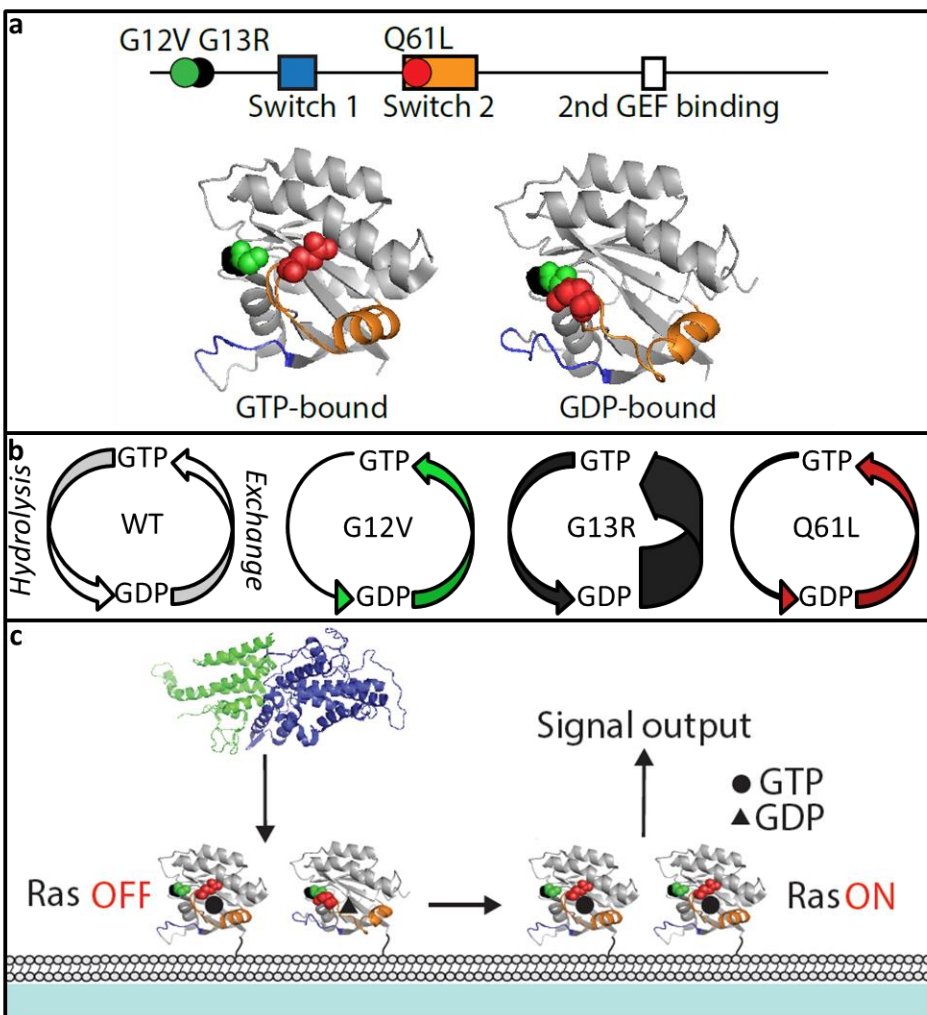
Figure 5.1. Oncogenic Ras mutations perturb nucleotide exchange and hydrolysis rates. (**a**) Domain sequence schematic and crystal structure of GTP- and GDP- bound forms of wild type Ras. Mutated residues G12, G13, and Q61 are highlighted as green, black, and red respectively; switch 1 and switch 2 regions are highlighted as blue and orange respectively (PBD: 4EFL, 3KUD). (**b**) Schematic showing main mechanism of oncogenic behavior: either decrease in GTP hydrolysis rate, resulting in longer-lived activating signals as compared to wild type (G12V, Q61L), or faster nucleotide release rate, yielding increased spurious activation of Ras (G13R). See Ref [53]. (**c**) Diagram of SOS[cat] activation of Ras. Ras (grey) is covalently attached to a supported lipid bilayer. SOS stably recruits through the allosteric site (green) and catalyzes the exchange of Ras-bound nucleotide from GDP to GTP at its catalytic site (blue), which is the activated signal output.
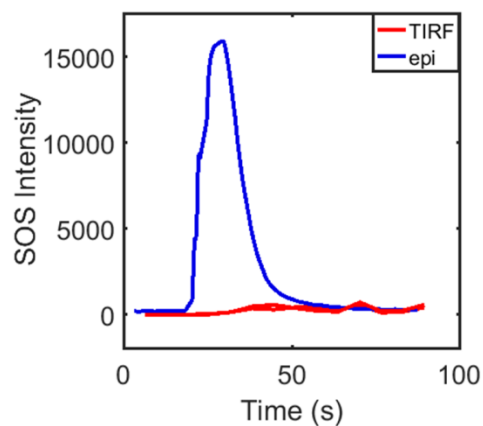
Figure 5.2. Characterization of the pulse of SOS through an imaging chamber. Epi-fluorescence imaging assess the concentration of SOS in the chamber, while TIRF images surface-localized SOS molecules within 100-200nm of the lipid bilayer. Combined, Epi-fluorescence allows for quantitation of SOS exposure, while TIRF allows for measurement of SOS interaction at the bilayer during time-integrated recruitment. Shown is a SOS recruitment to a Ras-free bilayer, allowing for quantification of the SOS pulse.
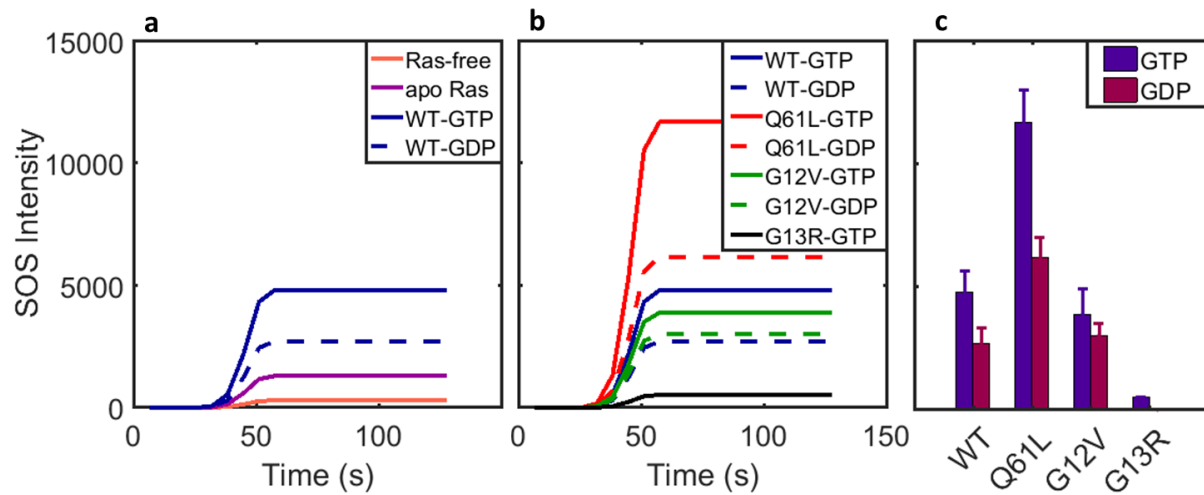
Figure 5.3. SOS recruits to Ras in a mutation-specific manner in the time-integrated recruitment assay. (**a,b**) Idealized depictions of SOS recruitment to lipid bilayers in the absence of nucleotide and under flow, based on the average recruitment values of six independent samples in most cases. (**c**) Bar graph showing average recruitment for each case tested, with error bars showing the standard deviation. (**a**) SOS binding to membranes is highly Ras-specific, and is nucleotide-specific. SOS recruits the least to apo-Ras, and the most to Ras-GTP, highlighting allosteric sensitivity. (**b/c**) SOS recruitment varies based on Ras mutations. SOS recruits the highest to Q61L Ras, and the least to G13R. Although recruitment to G12V Ras is similar, the level of allosteric sensitivity is declined in this mutation.
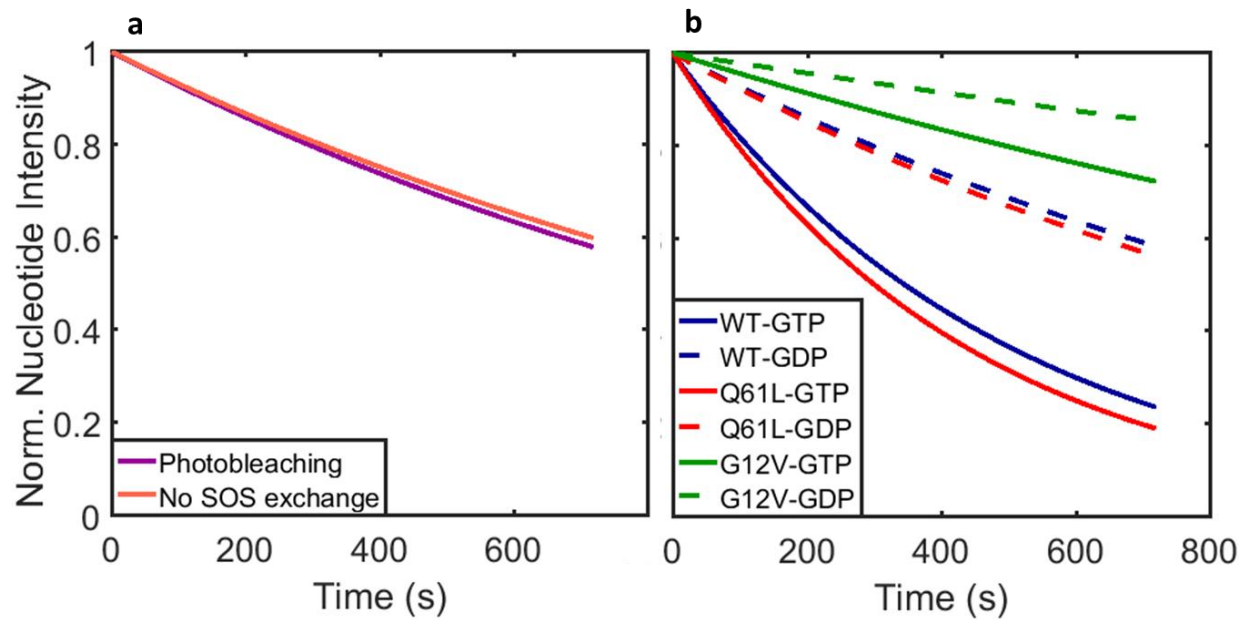
Figure 5.4. Rates of SOS-catalyzed nucleotide exchange are impacted by Ras mutations**.** Each trace is an exponential fit. An average of six independent samples is shown in most cases (see Fig 7 for individual tracles). (**a**) Control traces for WT, highlighting the resolution of the measurement. For the photobleaching curve, imaging was performed at the same position for the entire trace. In the absence of SOS exchange, dark nucleotide was added without SOS. These demonstrates the amount of photobleaching and base-level nucleotide exchange of the fluorescently labelled nucleotide. (**b**) Exponential fit of nucleotide exchange of Ras mutations in the presence of SOS and dark nucleotide.
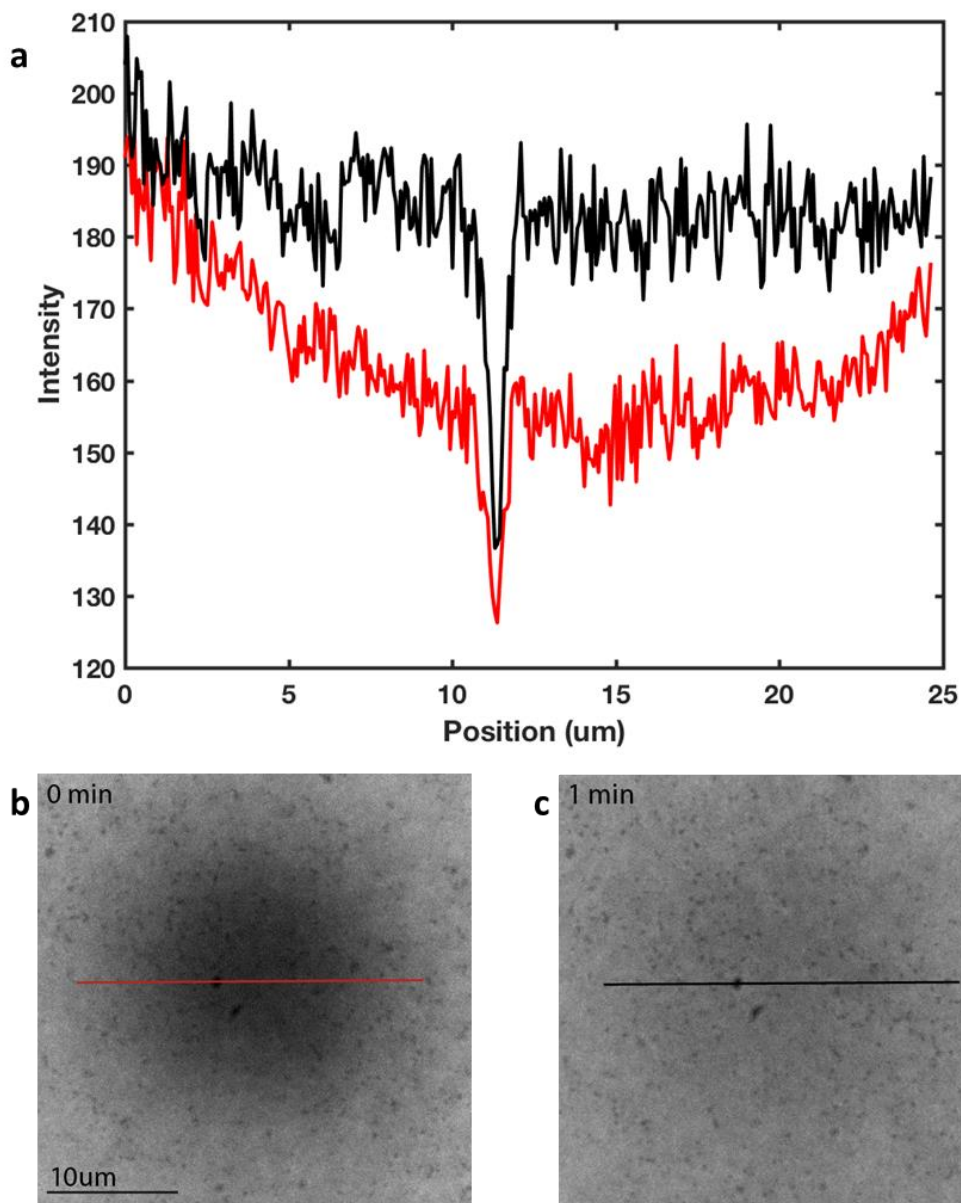
Figure 5.5. Characterization of mobility of lipid bilayer using FRAP. (**a**) Line intensity profile across photobleached region before (red) and after (black) recovery. (**b**) Texas red lipids were bleached with 561 laser in a small region of the bilayer. (**c**) After one minute of recovery, lipids have recovered to uniform fluorescence (with the exception of defects).
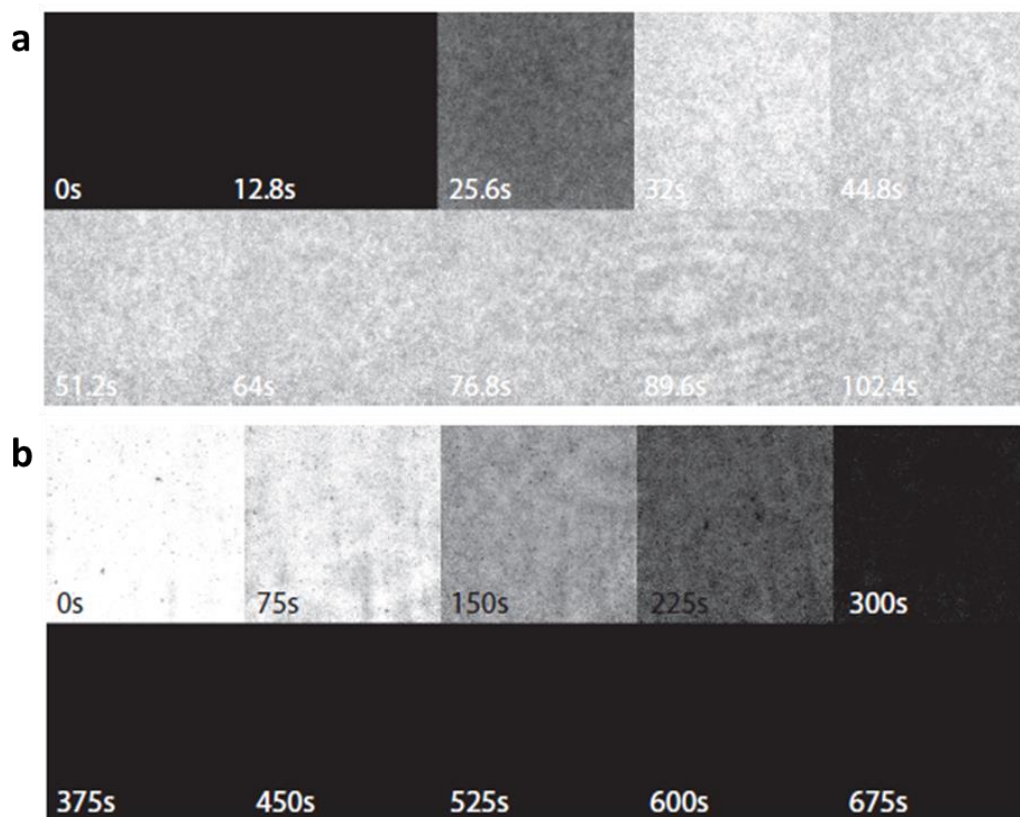
Figure 5.6. SOS recruitment and nucleotide exchange. Montage of SOS recruitment over time (**a**) and GTP exchange (**b**) on lipid bilayers functionalized with WT Ras. Images are shade corrected.
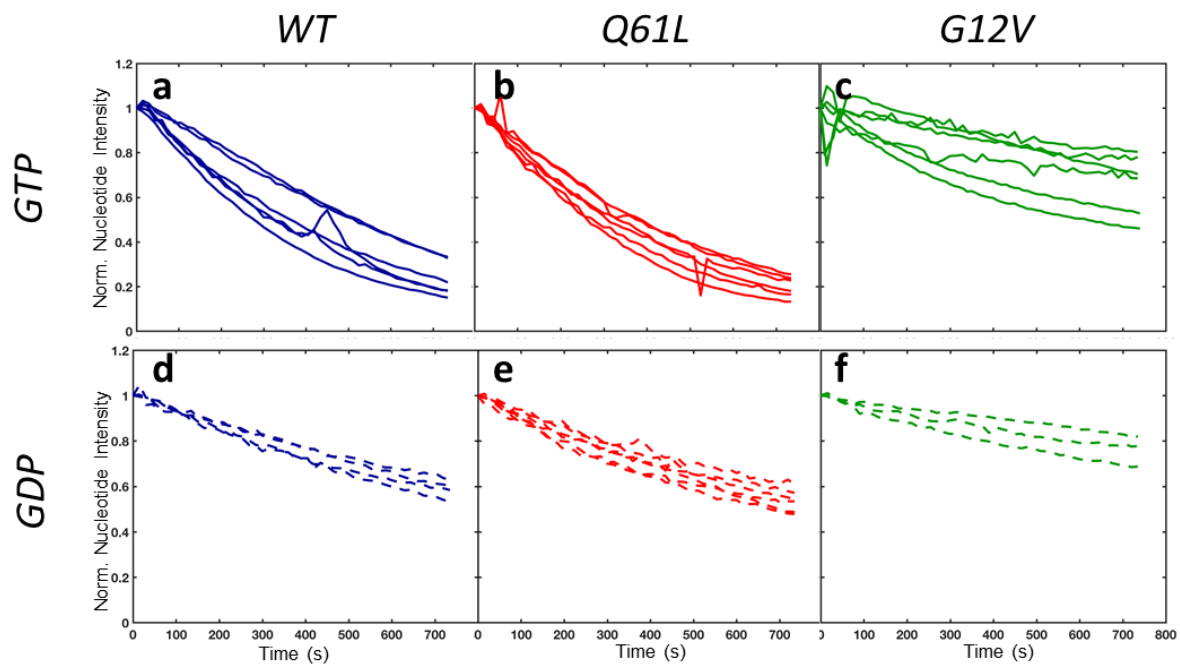
Figure 5.7. Normalized kinetic traces of nucleotide exchange on Ras mutations show reproducible results between independent samples. The top figures with solid lines show exchange of GTP-loaded Ras (**a-c**) and the lower figures with dashed lines show exchange of GDP-loaded Ras (**d-f**). The mutations used are depicted as follows: WT on the left, blue (**a,d**); Q61L in the center, red (**b,e**); and G12V on the right, green (**c,f**).

CHAPTER 6.

ARF ACTIVATION IS MEDIATED THROUGH A MEMBRANE-ASSOCIATING INTERMEDIATE AND RELIEF OF GEF AUTOINHIBITION

Meredith G. Triplet[§], Scott D. Hansen[§], Jean K. Chung[§], Jay T. Groves[§].

[§]Department of Chemistry, University of California, Berkeley, CA 94720, USA.

AUTHOR CONTRIBUTIONS

MGT and JTG conceived experiments. MGT performed experiments and analyzed data. SDH assisted with protein purification and data interpretation. JKC provided helpful suggestions for data analysis and provided Matlab code.

ACKNOWLEDGEMENTS

ABSTRACT

Arf proteins are a class of a small GTPases that have diverse functions in the regulation of the composition and morphology of membranes. Arf proteins have an unusual signaling cycle where the inactive GDP form is solution soluble, but the activated GTP form is membrane-bound. The signals required for robust Arf activation aren't fully understood, in part because previous explorations have lacked the spatial or temporal resolution necessary to resolve key features in the membrane associative dynamics of these proteins. Here, we show diffusion data of both Arf-GTP and Arf-GDP for the first time, providing direct evidence of a membrane-associating Arf-GDP intermediate. Further, the basal (GEF-free) activation rates of Arf are characterized for different membrane charges and the convolution between Arf association with GTP and Arf binding to the membrane is explored. Finally, the kinetic impact of the GEF ARNO and its truncations is measured, providing direct measurements that confirm an autoinhibitory role of the PH domain and its release by PIP3.

INTRODUCTION

Arf proteins, a class of the Ras family of small GTPases, broadly function in the regulation of membrane identification, lipid trafficking, and membrane morphology: Arf proteins are membrane regulators. They function to identify organelle identity[196], engage in lipid trafficking and membrane transport[48], lead to membrane budding[44], and cooperate to regulate the morphology – and possibly the destination – of the ERGIC (ER-Golgi Intermediate Compartment)[47], in addition to other diverse roles in the Golgi complex and in celia formation[46]. Arf has been speculated to play a crucial role in both sensing and defining membrane curvature. Arf1, the most highly studied Arf protein, is known to play a role in COPII vesicle budding from the golgi complex. It is hypothesized that Arf1, at high enough concentration, causes tubulation of membranes at high concentrations and has been speculated to dimerize, leading to membrane scission[197,198]. The creation of positive curvature is likely through changing the tension after the addition of the myristoyl group to the membrane. Arf1 has been seen to play a role in tubulation from the Golgi, likely playing an important role in the secretory pathway[199]. Intriguingly, Arfs can play a role in disease pathologies. Invading pathogens can trigger Arf activation in the host cell, leading to cell ruffling (a feature of *Salmonella* infection) and pathogen uptake through macropinocytosis[200]. One particular strain of *Salmonella* contains a GEF, SopE, that can modulate Arf activation in tandem with host GAPs, leading to cyclical activation patters and create micopinisomes for pathogen infection[201]. Bacterial cells can use Arf-like domains to use "identity theft" to mimic a benign cell compartment and to direct the secretory pathway[196]. As antibiotic resistance continues to spread, deep insight into the Arf pathway might suggest a novel way of combating bacterial infection. In addition to its role in pathogen uptake, Arf is also speculated to play a role in cancer invasion and metastisis[202].

Arf shares many features with the other members of the Ras family, such as the shifting conformation of the Switch 1 and Switch 2 regions based on the identity of the bound guanine nucleotide (either GDP or GTP) (**Fig 6.1b**), and its interactions with GEFs and GAPs[48]. Arf also depends on lipidation – the attachment of a myristoyl group – for proper function, including sufficient nucleotide exchange[203] and membrane localization[204]. One distinct feature of the Arf sub-family is the specific localization of Arf to membranes only when in the activated GTP-bound state. Arf has a β-sheet that serves as an "interswitch toggle" that shifts upon GTP binding, occluding the myristoyl binding pocket, and thus freeing the methylated myristoyl group to bind to membranes[205–207] (**Fig 6.1b**). Thus, Arf-GDP is solution soluble, but Arf-GTP is specifically localized to membranes[43]. While some evidence supports a transient, myristoyl-dependent interaction between Arf-GDP and membranes[203], this has never been directly visualized. The necessity of membranes in order to achieve Arf activation has been speculated to be caused by interactions between Arf's positively charged N-terminus and negatively charged bilayers[208], although no direct measurement of this interaction has been made.

Different Arf GTPases recruit specifically to different membranes[196], even though all species share the myristoyl group as the main driver of membrane localization. It is poorly understood how Arf membrane specificity occurs, but has been speculated GEF activity plays a role[209], and indeed, even that GEF interaction persists until a GAP releases the Arf from the bilayer[196]. Several Arf-GEFs exist, including Cytohesin1-4, EFA6A-D, PSD1-4, and BRAG1-3. All have the catalytic Sec7 domain, flanked by a PIP-lipid sensing pleckstrin homology domain[196,210]. The Sec7 domain activates Arf by causing the release of the bound nucleotide through an a hydrophopic interaction with the switch region, in addition to the insertion of a Sec7 glutamate into the Arf nucleotide binding pocket. The nucleotide exchange causes the shift of the β-sheet "interswitch toggle", which in turn displaces the myristoylated N-terminus[205–207]. Many of the Arf-GEFs are predicted to engage in allosteric activity through cooperativity of their PH domains[210,211], and even through the Sec7 dislocation of the myristoyl switch upon nucleotide exchange[212]. Subtle differences between the Arf switch regions and the GEF Sec7 domains has been shown to be sufficient to change the preference between protein interactions in vesicle studies[213]. Structural studies including a membrane mimic suggest the potential for flexible adaption in binding modes, allowing a myriad of Arf effector proteins to have possible binding sites that are not occluded by the membrane.[214]

One of the most studied Arf-GEFs is ARNO. In ARNO, the Sec7 domain is flanked by a N-terminal coiled-coil region and a c-terminal PH domain, with a concluding poly-cationic region (sometimes referred to as the C-domain)[215,216] (**Fig 6.1a**). While the ARNO PH domain can be activated by PIP2[208], the activation is highest for PIP3[216]. Cell studies that Arf6 and ARNO colocalize on cell membranes[209,217]. Structural and mutational analysis have indicated that the cytohesin Grp1 has an autoinhibited form that is relieved by binding to Arf6[211]. A similar process has been proposed for ARNO; mutational studies looking at the K336A mutation – a residue ARNO's PH domain that is crucial to a suspected Arf6 binding site – in reduces Arf activation on membranes without impacting ARNO's membrane association[218]. Further, vesicle studies show that the initial rate of ARNO exchange of Arf increases with an increasing initial pool of Arf1-GTP[218]. Despite the marked progress in our understanding of GEF activation of Arf proteins, there are many open questions about the spatiotemporal regulation of this process.

As the Arf signaling cycle is inherently meshed with membrane association, any exploration of Arf signaling needs to include a membrane substrate. Glass supported lipid bilayers (SLBs) provide an excellent membrane mimic that can be used in conjunction with TIRF microscopy and single particle tracking (SPT) to explore the kinetics of protein diffusion, association, and desorption[219]. To our knowledge, this is the first exploration of Arf signaling on the SLB platform, and the first use of SPT on this protein system.

Previously, it has been shown that Arf modifications – especially at the C-terminus – can have dramatic impact on Arf activity[220]. Given that many published works fail to make the form of

Arf used fully explicit, some confusion exists in the field in regards to the true activity of Arf. Herein, we attempt to explore the impact of any experimentally necessary modifications of Arf.

RESULTS

Assessing Arf diffusion when bound to GDP and GTP
Supported lipid bilayers were used as a platform to image myr-hArf1-Alexa488 or –Alexa 647 (referred to generically as Arf, or as Arf-Alexa488/Arf-Alexa647 throughout). Activity of the protein was found to be comparable to that of unlabeled myr-hArf1 (**Fig 6.7**). For initial diffusion experiments, Arf exposed to GDP and exposed to GTP were added at low concentrations so that single molecule particles could be distinguished and tracked. Based on the step size data, diffusion information was calculated (**Fig 6.2**). Arf-GTP and Arf-GDP have similar diffusive states, although Arf-GTP has substantially longer dwell times (**Fig 6.3**). Also note that adding in a high concentration of dye labelled with the other fluorophore made no significant impact on the diffusion rates. All data was poorly fit by a one-component Brownian diffusion model (**Fig 6.6**); this suggests that Arf engages with membranes in two distinct conformations: one with deeper engagement with the lipids, and one with a less association into the bilayer.

Note that, although the diffusion values are consistent, the fraction of Arf in the slower diffusive state is increased in the Alexa488 labelled protein as compared to the Alexa647 protein. This suggests that the fluorophore is slightly altering the protein behavior, with Alexa488 increasing the chance for deeper engagement into the bilayer. As fluorophores are widely known to have varying degrees of membrane binding, this could most easily be understood as an interaction between Alexa488 and the bilayer slightly increasing the partitioning into the slow state. Additionally, high-density Arf SPT data was obtained by doping in a large amount of Arf in the alternate channel (**Fig 6.2b,e**). Although some reports of Arf dimerization have been made before, we were unable to determine any change in the diffusion rate for Arf at the concentrations explored. It is possible that dimerization would be apparent at higher densities (about 20 particles/μm^2).

Further, given the amount of Arf in solution in both cases (250pM for GDP), we can make an estimate of the fraction of Arf that is membrane associating. For GDP, the order of 0.001% of Arf –GDP proteins are membrane associating at any given moment. Although this represents a very small fraction of Arf, is it notable for its consistency and reproducibility.

Basal activation of Arf in the absence of GEF
In subsequent measurements, Arf was added at a constant concentration under a variety of conditions and the kinetics of membrane interactions were observed. As the rate of reaction was very slow and did not reach equilibrium within an hour, the off-rates were explored by

93

introducing a buffer flow to remove detached protein and prevent re-association with the membrane. There is a clear difference in the interaction between Arf-GTP and Arf-GDP and membranes, as Arf-GDP immediately comes to an equilibrium where tiny amounts of the protein are membrane associative. Additionally, Arf membrane binding and nucleotide exchange are inherently twined, as Arf isn't able to bind to GTP in a stable way when not exposed to the membrane environment (**Fig 6.3a,b**). If Arf was able to bind to GTP during a solution pre-incubation step, then Arf in the pre-GTP incubation condition would be expected to have a higher initial level of Arf-GTP association. Instead, Arf pre-incubated with GTP has no head-start. Some GTP remains in solution even after dilution and addition to the bilayer sample, but at a limiting concentration (100nM), explaining the slower kinetic on-rate for this condition. This result was also confirmed via spectrophotomer readings of protein in solution with and without vesicles present (**Fig 6.11**). The implication of this is that protein activation (nucleotide exchange to GTP) and recruitment to the membrane and inherently convoluted.

When exposed to GTP, Arf, even in the absence of GEF, exhibits notable recruitment to negatively charged 10% DOPS bilayers (**Fig 6.3a,c**). In contrast, the interaction of Arf-GTP with positively charged 10% DOTAP bilayers was substantially less, with on-rates 20% of the DOPS case, and off-rates around 400% of the DOPS condition (**Table 6.1**). Although Arf responds differently to positively and negatively charged bilayers, Arf doesn't appear to be sensitive to differences in the magnitude of negative charge (**Fig 6.10**). Further, Arf-membrane interaction isn't solely charge mediated, as Arf can in fact activate to DOTAP bilayers in the presence of GTP; this indicates that nonpolar interactions also play a key role in Arf-membrane localizations. Arf interaction with positively charged bilayers is also less for constructs bound to GDP; although the protein doesn't recruit over time, the number of protein engagements with the membrane is much less (**Fig 6.2a,c**). Desorption rates are similar for all conditions (**Fig 6.2b**), showing extremely long dwell times even in the absence GEF. In contrast to GTP bound Arf constructs, Arf-GDP does not dwell on the membrane under flow, but instead is immediately washed away (**Fig 6.3b,c**).

GEF-mediated Arf activation confirms autoinhibitory role of PH domain
The activation rate of Arf binding to membranes is greatly increased in the presence of GEF at high concentrations (1μM). Here, the impact of the GEF ARNO and its truncations, Sec7-PH and the Sec7 catalytic domain, were explored. Herein, the full length protein is referred to as ARNO; the ARNO[Sec7-PH- polycationic] is referred to as Sec7-PH, and the catalytic domain only (ARNO[Sec7]) is referred to as Sec7 (**Fig 6.1a**). All three GEF constructs have dramatically faster activation rates than Arf without GEF (**Table 6.1**). As compared to the no-GEF case, ARNO increases Arf activation by a factor of 10; the removal of the coiled-coil domain nearly doubles the activation, as Sec7-PH increases activation over the no-GEF condition by a factor of about 19; and the Sec7-PH activation is almost doubled by the inclusion of 4% PIP3 lipids; and Sec7 increases the activation of Arf by a factor of around 70, regardless of lipid composition. Sec7 (the catalytic domain only) has the fastest exchange rate, which is independent on PIP3 lipids (as would be

expected). The addition of PIP3 does relieve autoinhibition of the Sec7-PH domain, but not entirely to un-autoinhibited (Sec7) levels (**Fig 6.4**). Although PIP3 does release some of the autoinhibition of the Sec7-PH domain, the rate appears to be slower than the Sec7 domain alone, suggesting that further activation signals – such as higher concentrations of Arf1, or the presence of Arf6[218] – are required to achieve full activation. The off-rates, however, were more consistent for all cases, although suggest the possibility that Sec7-PH stabilizes Arf to remain on the membrane longer (**Table 6.1**). (Desorption data for ARNO could not be calculated, as the protein didn't achieve equilibrium during the allotted time.)

DISCUSSION

The Arf-GDP state has a crucial membrane-interacting conformation that allows for engagement with GEF (**Fig 6.5a**), which is visible in the similar diffusive membrane states for both Arf-GTP and Arf-GDP. This state is likely made possible by the flexible linker (**Fig 6.1b**) that enables the myristol group and the N'-helix of Arf to release from the binding pocket and associate (in a transient way) with the bilayer. The Arf-GDP diffusion data is, to our knowledge, the first direct measurement of a membrane-associating Arf intermediate. The comparison between Arf-GDP and Arf-GTP diffusion also provides insight into the similarity of the membrane interaction between these species, and suggests that the movement of the interswitch toggle shifts the equilibrium of an already-flexible linker to favor bilayer association much more strongly. Given the transience of the Arf-GDP interaction with membranes, supported lipid bilayer (SLB) assays or others like it are necessary to resolve this state.

Even though the membrane-associating diffusive states of Arf-GDP and Arf-GTP are similar, the distinct differences in the kinetics of membrane dissociation provide a clear distinction between how these two constructs engage with membranes. Arf alone is sensitive to membrane charge, and has much greater interaction with negatively charged membranes. However, Arf can still bind to positively charged bilayers, indicating that the hydrophobic residues work in tandem with positively charged residues to bind to membranes. Arf-GDP also appears to have less interaction with DOTAP bilayers, consistent with the hypothesis that Arf-GDP interaction is caused by spurious engagement with the Arf flexible linker. In both cases, all of Arf-GDP is removed upon washing.

Additionally, the exploration of Arf pre-incubated with GTP demonstrate the negligible amount of activation that can occur without the presence of membranes. Arf can't engage in to membranes without GTP, and Arf can't bind to GTP without membranes (**Fig 6.5c,f**). Therefore, Arf membrane binding and nucleotide exchange are inherently twined. A membrane imaging assay, such as is made possible by the SLB platform, is necessary to be able to meaningfully distinguish between Arf localization and Arf activation.

In the absence of PIP lipids, Sec7 can interact with Arf to activate it, despite some degree of autoinhibition (likely by the PH domain occluding the Arf binding pocket) (**Fig 6.5d**). Arf is then converted to a more stably associating form, where the myristoyl group can't rebind due to the relocation of the interswitch toggle. In the presence of PIP lipids, autoinhibition of ARNO is at least partially relieved, allowing for more robust activation of Arf. It seems likely that another signaling component, such as a secondary activating Arf1 or Arf6, or perhaps membrane curvature, is required to achieve full activation of the Arf pathway, as has been previously suggested.

The presence of Arf-GDP on membranes could play a key role in the initiation of Arf signaling pathways, as Arf-GEFs have distinct membrane associative domains that tether that would likely pre-localize them to the membrane. An Arf-GDP membrane associating intermediate would be more likely to encounter a GEF and be activated.

METHODS

Purification and labelling of myristoylated Arf1

The construct [LFASK]-Arf1(C159S, S147C) was co-expressed with yeast N-myristoyltransferase by using a BL21* *E. coli* cell line competently expressing NMT. Antibiotics and 1% glucose was added to TMP media in 50mL flasks, and flasks were inoculated with single, medium-sized colonies. Cultures were grown to an OD of 3 before inoculating 8-1 liter TPM fernbach flasks to a starting OD600= 0.05. Cultures were grown at 37°C until OD600= 0.6. 50µM sodium myristate was added from a 1000x stock prepared in methanol, and growth was continued for an additional 20-30min before the inducing with 0.1 mM IPTG. Protein was expressed for 3 hours at 37°C before harvesting. Cells were resuspended in 20 mM Tris-HCl (pH 8.0 @4°C), 100 mM NaCl, 1 mM MgCl$_2$, 1 mM BME, 1 mM PMSF, DNAse, and were lysed using a microfluidizer. Lysed material was centrifuged at 45,000 rpm (207,871 x *g*) for 45 min in a pre-chilled Beckman Ti70 rotor at 4°C. Ammonium sulfate was added gradually over 20 minutes to reach a final concentration of 35% (209 g/L), and was stirred an additional 20 min, keeping cool throughout. The sample was spun down again in the Beckman Ti70 rotor at 9,000 rpm (8315 x *g*) for 20 min at 4°C. The pellet was resuspended in 20 mM Tris-HCl (pH 8.0 at 4°C), 100 mM NaCl, 1 mM MgCl$_2$, 1 mM DTT, 10% Glycerol, and then dialyzed in 4L of this buffer overnight. The sample was spun down again at 45,000 rpm (207,871 x *g*) for 45 min in a pre-chilled Beckman Ti70 rotor at 4°C and filtered with a 0.45µm and 0.22µm filter to remove cloudiness. Sample was applied to a DEAE Sepharose Fast Flow (GE Healthcare, Cat# 17-0709-01) column, and eluent was collected. The sample was buffer exchanged into 10 mM MES pH5.7, 1mM MgCl2, 1mM DTT, 10% Glycerol using a HiPrep 26/10 desalting column (GE Healthcare, Cat# 17-5087-01). The sample was then applied to a 1mL MonoS (5/50 GL) cation exchange column (GE Healthcare, Cat# 17-5168-01) equilibrated with the low-salt buffer, and was eluted using a linear salt gradient (0-500 mM NaCl) into buffer containing 500mM NaCl

over 50 CV (50 mL total); the protein eluted between 130 and 170mM NaCl. The protein was combined and concentrated using a 5 kDa MWCO Vivaspin 6 (GE Healthcare, Cat# 28-9322-94), and then applied to a Superdex75 (10/300 GL, GE Healthcare, Cat# 17-5174-01) equilibrated in 20mM Tris [pH 8.0], 100mM NaCl, 1mM $MgCl_2$, 0.5mM TCEP, 10% glycerol. Protein was collected and snap-frozen with liquid nitrogen, and purity was confirmed by SDS-PAGE gel. Protein was thawed on ice, and 2x fresh dye dissolved in DMSO (either Alexa647- or Alexa488-maleimide) was added to protein and let sit for at least 10 min before quenching with DTT. Sample was diluted to 5mL and concentrated with 5 kDa MWCO Vivaspin 6 to remove free dye before re-running over superdex75. Concentrated with 5 kDa MWCO Vivaspin 6 again before snap freezing in liquid nitrogen.

Purification of [Δ17]-Arf1-his6

[Δ17] - hArf1 - his6 was expressed in BL21* (DE3) *E. coli* cells. Cells were resuspended in 50 mM Na_2HPO_4 [pH 8.0], 400 mM NaCl, 0.4 mM BME, 1 mM PMSF, DNase and were lysed using a microfluidizer. Lysed material was spun at 16,000 rpm (35,172 x *g*) in a Beckman JA-17 rotor chilled to 4°C for 60 minutes at 4°C. Supernatant was recirculated over a 5 mL HiTrap Chelating column (GE Healthcare, 17-5166-01) charged with 100 mM $CoCl_2$ for 1 hour that was equilibrated in the lysis buffer. The protein was eluted off of this column using a 500mM imidazole buffer. Protein was dialyzed into 20mM Tris [pH 8.0], 100mM NaCl, 1mM $MgCl_2$, 0.5mM TCEP, 10% glycerol overnight. To remove cloudiness, sample was spun at 7000rpm for 10 min at 4C, and filtered through 0.22 μm filter. Loaded cleared sample onto Superdex75 (10/300 GL) column (GE Healthcare, Cat# 17-5174-01). Protein was concentrated with a 5kDa MWCO Vivaspin 6 column (GE Healthcare, Cat# 28-9322-94) before snap freezing with liquid nitrogen. Sample purity was verified with SDS-PAGE gel.

Purification of ARNO

Three constructs (his6-MBP-N10-TEV-GGGGG-ARNO(1-400aa) – referred here as ARNO-FL, his6-MBP-N10-TEV-GGGGG-ARNO(51-400aa) – referred here as Sec7-PH, and his6-MBP-N10-TEV-GGGGG-ARNO(51-252aa) – referred here as Sec7) were expressed in BL21* (DE3) *E. coli* cells in 2 liters of TB per construct at 18°C overnight. Bacteria was lysed using a microfluidizer into 50 mM Na_2HPO_4 [pH 8.0], 400 mM NaCl, 0.4 mM BME, 1 mM PMSF, DNase. Lysed material was spun at 16,000 rpm (35,172 x *g*) in a Beckman JA-17 rotor chilled to 4°C for 60 minutes at 4°C. Lysate was flowed over a 5 mL HiTrap Chelating column (GE Healthcare, 17-5166-01) charged with 100 mM CoCl2 for 1 hour that was equilibrated in 50 mM Na_2HPO_4 [pH 8.0], 400 mM NaCl, 0.4 mM BME. Protein was eluted a buffer containing 500 mM imidazole. TEV protease was added. Protein was dialyzed into 4 L of 50 mM Na_2HPO_4 [pH 8.0], 400 mM NaCl, 0.4 mM BME, and TEV was cleaved overnight. Cleaved protein was recirculated over a HiTrap (Co+2) column (5 mL) for about 1 hour. Protein was applied to G25 Sephadex desalting column to buffer exchange into 10mM HEPES [pH 7.0], 1mM DTT (ARNO-FL and Sec7) or a 20 mM Trip [pH 8.0], 1mM DTT (Sec7-PH). Protein was then applied to a 1mL MonoQ (5/50 GL) anion exchange column (GE Healthcare, Cat# 17-0409-03),

and was eluted with a linear gradient (0.05 – 1M NaCl) into the buffer containing 1 M NaCl. ARNO-FL and Sec7-PH eluted over 90 CV, Sec7 eluted over 50CV. Then, protein was applied to a Superdex75 (10/300 GL) column (GE Healthcare, Cat# 17-5174-01) column equilibrated in 20 mM HEPES [pH 7.0], 150 mM NaCl, 10% glycerol, 0.5 mM TCEP. Protein was concentrated with a 30kDa MWCO Vivaspin 6 (GE Healthcare, Cat# 28-9323-17) (ARNO-FL, Sec7-PH) or with a 5kDa MWCO Vivaspin 6 column (GE Healthcare, Cat# 28-9322-94) (Sec7) before snap freezing with liquid nitrogen.

Supported lipid bilayer platform
Bilayers were made from DOPS (10%), DOTAP (10%), or PIP3 (4%), and TR-DHPE (0.01%) with the remaining lipids Egg-PC – 99% purity. All lipids were purchased from Avanti Polar Lipids (Alabaster, Alabama). Lipids were mixed in a piranha-etched round bottom flask and the chloroform was evaporated using a rotovap with a 40°C bath for 30 minutes, and then was put under nitrogen for at least 10 minutes. Lipids were then rehydrated with ultra-pure water to a density of 1mg/mL, sonicated with a Sonics Vibra-Cell to achieve single unilamellar vesicles (SUVs), and spun down at 15000rpm at 4°C for at least 20 minutes in an Eppendorf Centrifuge 5424 R. #1.5 glass slides (Ibidi, Cat # 10812) were sonicated in IPA for 30 min, rinsed in MilliQ water, and then were etched with piranha for 10 minutes within an hour of bilayer assembly and attached to an Ibidi sticky-Slide VI$^{0.4}$ (Cat# 80608) chamber. Lipids were mixed with concentrated PBS stock to achieve a 1x PBS final concentration, and added to the chamber for a 30 min incubation. Defects in the bilayer were blocked with 2.5mg/mL casein for 10 minutes. Bilayers were either imaged immediately, or were stored at 4°C overnight.

Arf kinetic measurements
All measurements were made in BME + casein reaction buffer (40mM HEPES, 100mM NaCl, 5mM MgCl, pH 7.4, 10mM BME, 0.25mg/mL casein). For Single Particle Tracking (SPT) data, oxygen scavenging buffer was used, including 20 mM glucose + 2 mM Trolox (UV treated) + 320 µg/mL glucose oxidase + 50 µg/mL catalase, kept on ice, and with the glucose added 5-10 minutes before imaging. Immediately prior to the experiment, samples were brought to room temperature (if stored overnight) before buffer exchanging to HEPES buffer, and a FRAP of the Texas Red lipids was performed to assess bilayer quality.

Single Particle Tracking
Background images of 1 frame in the channel used for Single Particle Tracking (SPT) at 50 positions were collected to assess the potential for contamination. These positions were saved for later measurements. (Moving through multiple positions during imaging reduces the potential for photoeffects impacting protein behavior.) Before addition of Arf, an acquisition of 10 frames 488 TIRF and 647 TIRF with a 200ms interval was started in order to assess the recruitment level of Arf. Imaging buffer containing 10pM Arf (for GTP case) or 250pM Arf (for GTP case) (labelled consistent with the channel chosen for SPT), 1µM Sec7, and 1µM nucleotide (either GDP or GTP) was added after the first position was imaged, and the acquisition was aborted once the

density level was appropriate for SPT (around 50 bright particles per field of view – around 5-10 minutes incubation under these conditions). Streaming data of 250-1000 frames per position was then collected in the not-yet-imaged saved positions until at least 2000 SPT frames of data was acquired. To assess any indication of changing diffusion rate upon higher concentrations of protein, a large amount of Arf protein with the other label was then added into the sample. As before, an acquisition of 10 frames of each channel over 50 positions was started to assess Arf recruitment. Imaging buffer containing 50nM Arf with the bulk label, 250pM Arf with the SPT-level label (only in the GDP case – for GTP, the addition of new protein isn't sufficient to remove an appreciable amount of protein associated with the membrane so no more protein in the SPT channel is added), 1µM Sec7, and 1µM nucleotide was then added. As before, streaming data in the SPT channel was taken in new positions for a total of 2000 frames. All streaming data was collected in the presence of oxygen scavenging buffer.

Recruitment and Desorption
After the initial sample images, 50 positions of 1 frame 488 TIRF, 1 frames 647 TIRF with a 200ms interval was collected as a background readout. These 50 positions were saved for later imaging. Before the addition of Arf (with or without GEF), the next acquisition was started (the same 50 positions with 10 frames in each channel). For the condition with pre-incubation with nucleotide, 1µM of Arf-Alexa647 and 1µM of Arf-Alexa488 were left with 33.9µM of GTP for at least 30 minutes (with no lipids present). This stock was then diluted down to a final concentration of 10nM each Arf construct and 100nM nucleotide in solution exposed to the lipid bilayer. (Note that this concentration of GTP appears to be limiting.) For all other protein preps, 10nM Arf-Atto647, 10nM Arf-Atto488, and 1µM nucleotide was added, with our without 1µM GEF. If GEF was added, then it was added at a 1µM concentration. (Note that without GEF, single particles can be resolved per frame using these concentrations. With GEF, the recruitment is greatly increased, so much so that the EM gain was reduced by a factor of 10 to avoid overexposure.) Protein was added during the acquisition. For desorption measurements, the same imaging conditions as before were used. Before starting imaging, the sample was briefly washed to remove protein still in solution and a syringe pump (Harvard Apparatus 11plus, Cat# 70-2208) was attached to the sample. The acquisition was then started, and after the first position was imaged, a steady flow (0.5mL/min, 10mL total) was maintained over the sample.

TIRF microscopy
Images were taken on a Nikon microscope (Nikon Eclipse Ti (Ti HUBC/A), Technical Instruments, Burlingame, CA)with a Nikon Apo TIRF 100x/ 1.49 oil objective and an Andor EM-CCD camera (iXon ultra 897, Andor Inc., South Windsor, CT), as controlled by micro-manager2. Coherent's OBIS lasers were used (488, 561, and 647), along with Chroma emission filters for each matching line. Single Particle Tracking (SPT) data was taken with 20ms exposure time, streaming; all other data was taken with at least a 200ms delay to minimize photobleaching and photoblinking.

Imaging analysis
Single Particle Tracking
All images were analyzed using FIJI software from the ImageJ software family. The TrackMate pluggin[221] was used for Single Particle Tracking (SPT). Particles were found using the DOG detecter, and an estimated spot size of 0.5uM was used, with a threshold ranging between 90-300 for different fluorophores. About the top 50% of particles were kept, based on quality. The max linking distance was 1.5 μm, and the max frame gap was 1. To exclude immobile tracks and inaccurately linked tracks, tracks with the lowest displacement were excluded, as well as tracks below the mode mean velocity, and the top fraction of mean velocity traces. Traces with the lowest average quality were also excluded. Tracks from multiple positions and multiple independent samples were used to calculate diffusion rates using Matlab code written by Jean Chung.

Recruitment and Desorption
A calibration curve was found by counting the number of particles per frame using TrackMate, and then fitting this against the fluorescent intensity to find the linear relationship between particle count and intensity read-out. Recruitment and desorption data was background-subtracted from the initial data collected at the same position. Each line is the average of 3-5 replicates, excepting the Sec7 on 4% PIP3 bilayers where duplicate data sets were used. Kinetic fits were performed using a unimolecular mass action kinetic model. For samples that did not reach equilibrium, the k_r (for recruitment data) or the k_f (for desorption data) was set to 0. All data was put into units of picomole and seconds for kinetic analysis, assuming 30μL of volume within the Ibidi chamber. Kinetic constants are reported in units of s^{-1}.

Cleaning
Round-bottom flasks for lipid preparation were immediately rinsed in IPA 5 times, and stored in isopropyl alcohol/MilliQ water. Flasks were bath sonicated in isopropyl alcohol/MilliQ water for 30 minutes, well rinsed in MilliQ water, and then piranha etched for 30 minutes. Flasks were well rinsed in MilliQ water before storing in the oven to keep try.
Ibidi chambers were soaked overnight in acetone to remove tape. After removing bulk de-adhered tape pieces, chambers were bath sonicated in acetone for 30 min to remove more tape. Chambers were rinsed in MilliQ water, and then left in microwave heated 1% Hellmanex solution (Fisher, Cat# 14-385-864) for an hour. Chambers were rinsed before each of the following 30 min bath sonication steps: isopropyl alcohol, isopropyl alcohol/MilliQ water, MilliQ water. Chambers were rinsed with MilliQ water a final time before storing in MilliQ water under parafilm (Heathrow Scientific, Cat# 152-68322-368).
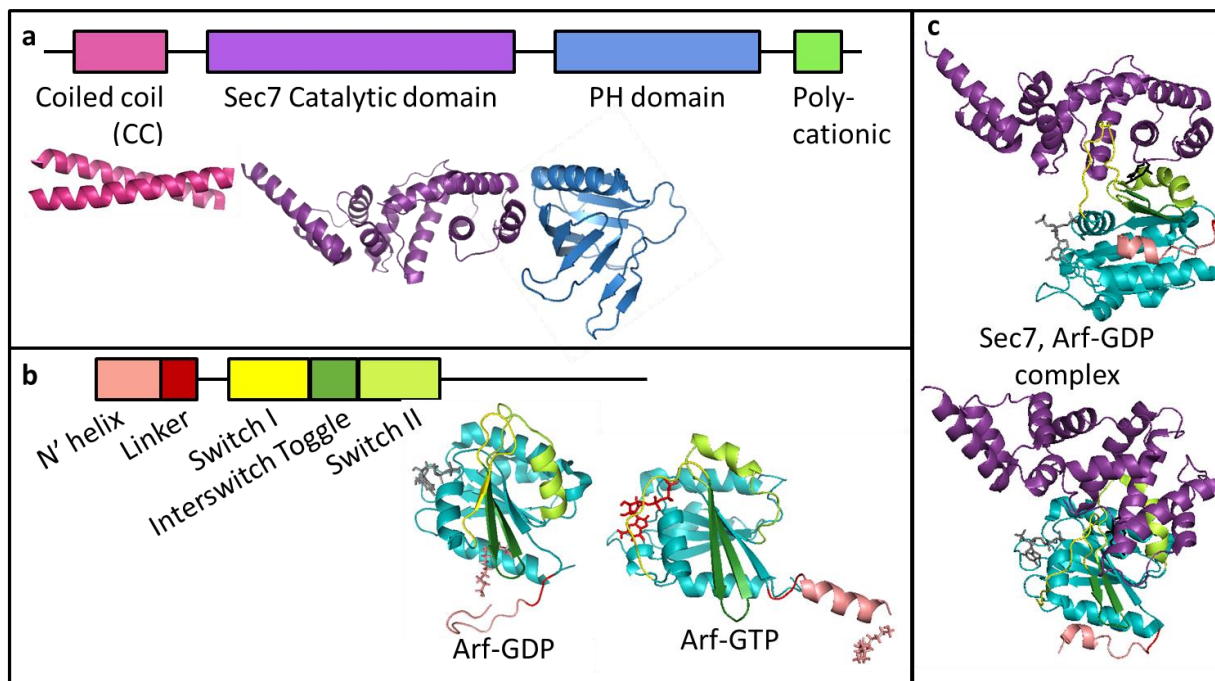
Figure 6.1. Depictions of Arf and ARNO proteins. (**a**) ARNO with key domains colored in a linear and crystal structure schematic. The N-terminal domain of ARNO includes a coiled-coil (fuchsia; representative coiled coil shown is not from ARNO, but is the key example of the domain class: PDB 1ZIK). The Sec7 domain (purple: PDB 4Z21) is the catalytic core of the protein. The PH domain (blue: PDB 1U27) binds to PIP3 lipids with high specificity, and can also interact with PIP2 lipids. (These domains have not been co-crystalized, but are simply displayed in proximity.) (**b**) Arf with key domains colored in both linear and crystal structures (GDP: PBD 2K5U, GTP: PDB 2KSQ). The N-terminal region of Arf is membrane associating, and is bound to a myristoyl group (coral). The flexible linker (dark red) that connects this domain to the remainder of the protein allows for the N' helix and the myristoyl group to dock in the GDP form, but to associate with the membrane in the GTP form. The Switch I and Switch II regions (yellow and light green, respectively) shift dramatically between the two structures, as is common for all small GTPases. In Arf, these two switch domains are linked by an Interswitch Toggle (dark green) that is instrumental in dislocating the membrane-associative group in the GTP form, resulting in membrane binding. GDP is shown in grey, and GTP in red. (**c**) The Sec7 domain in complex with Arf1-GPD and Brefeldin A (PDB 1R8Q), shown in two orientations, and falsely colored as in (**a**) and (**b**).
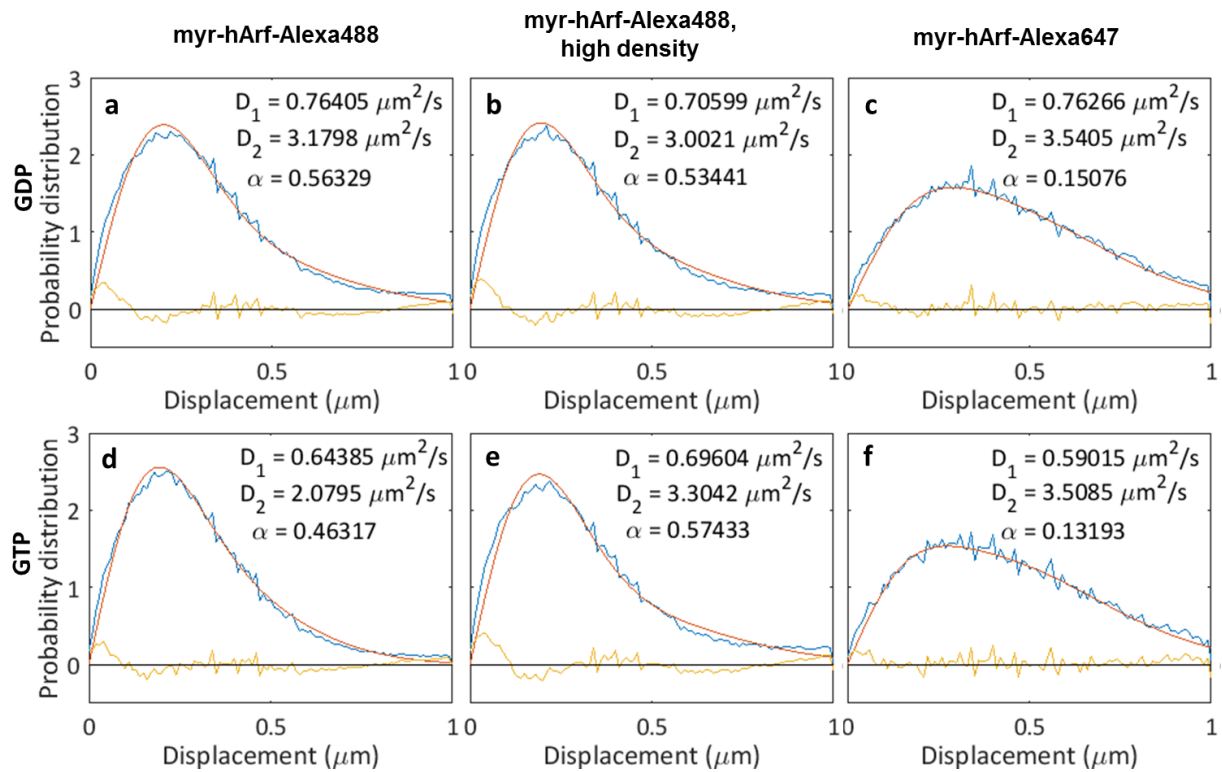
Figure 6.2. Diffusion traces of Arf from Single Particle Tracking (SPT) data in 6 different conditions: GDP nucleotide with myr-hArf1-Alexa488, at low (**a**) and high (**b**) density, and with myr-hArf1-Alexa647 (**c**), and also GTP nucleotide with myr-hArf1-Alexa488, at low (**d**) and high (**e**) density, and with myr-hArf1-Alexa647 (**f**). Note that the two dye constructs show slightly different diffusion rates, but that nucleotide state and protein density doesn't substantially effect diffusion kinetics.
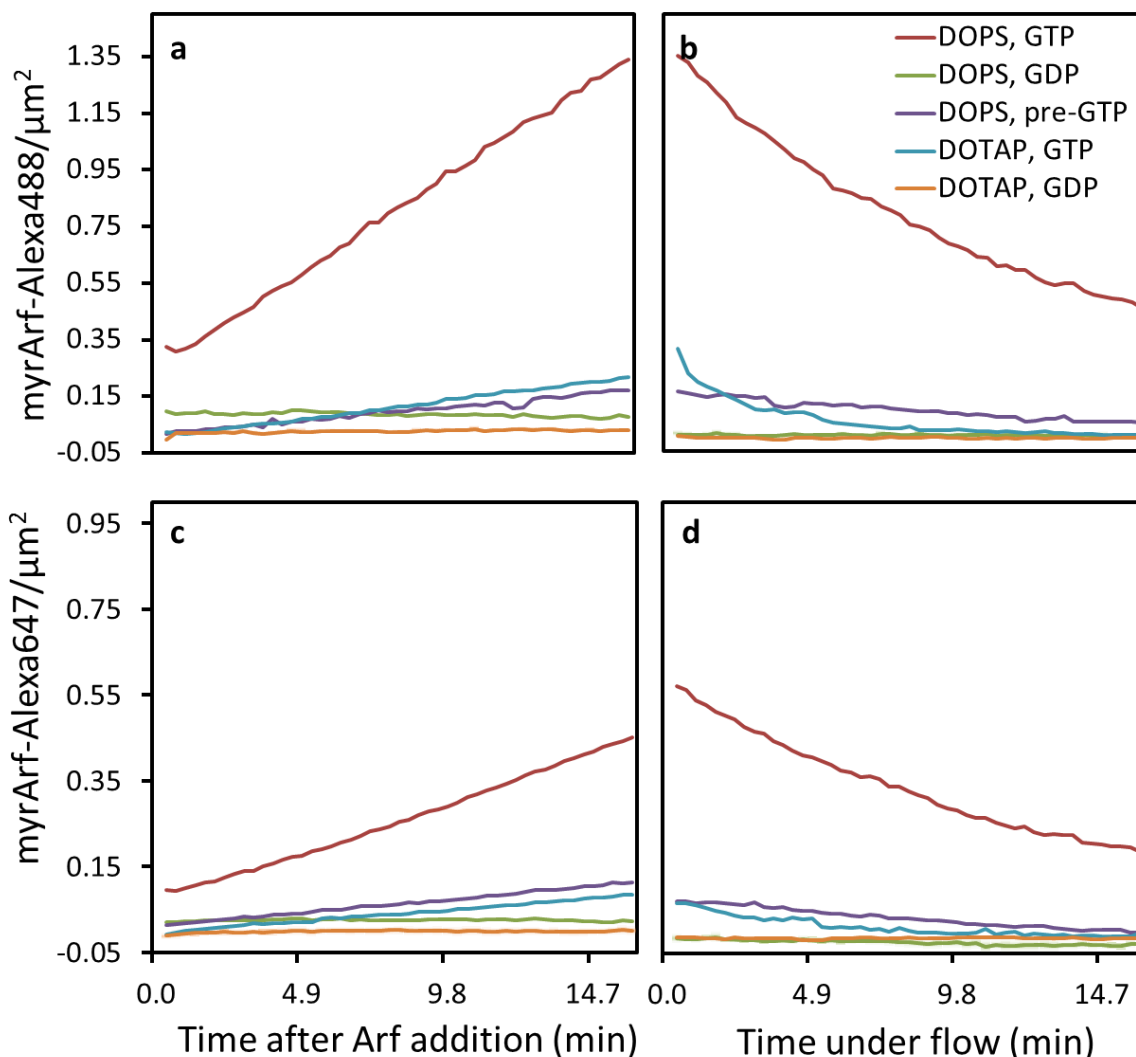
Figure 6.3. Recruitment and desorption of Arf to supported lipid bilayers with differing lipid compositions (either 10% DOPS or 10% DOTAP) without GEF, and when pre-incubated with GTP in solution. (**a**) Recruitment of myr-hArf1-Alexa488; (**b**) desorption of myr-hArf1-Alexa488; (**c**) recruitment of myr-hArf1-Alexa647; (**d**) desorption of myr-hArf1-Alexa647. Each trace is the average of at least three independent samples. Note the distinct different in recruitment and desorption for GDP and GTP in all cases: the amount of Arf-GTP on the bilayer increases linearly over time and is washed out gradually, whereas the amount of Arf-GDP is stable, and is washed out immediately. Further note that negatively charged bilayers are required to activate Arf, and that pre-incubation with GTP does not lead to a head start in recruitment values. Even with negatively charged bilayers, Arf is not able to achieve equilibrium within the 15-minute allotted time.
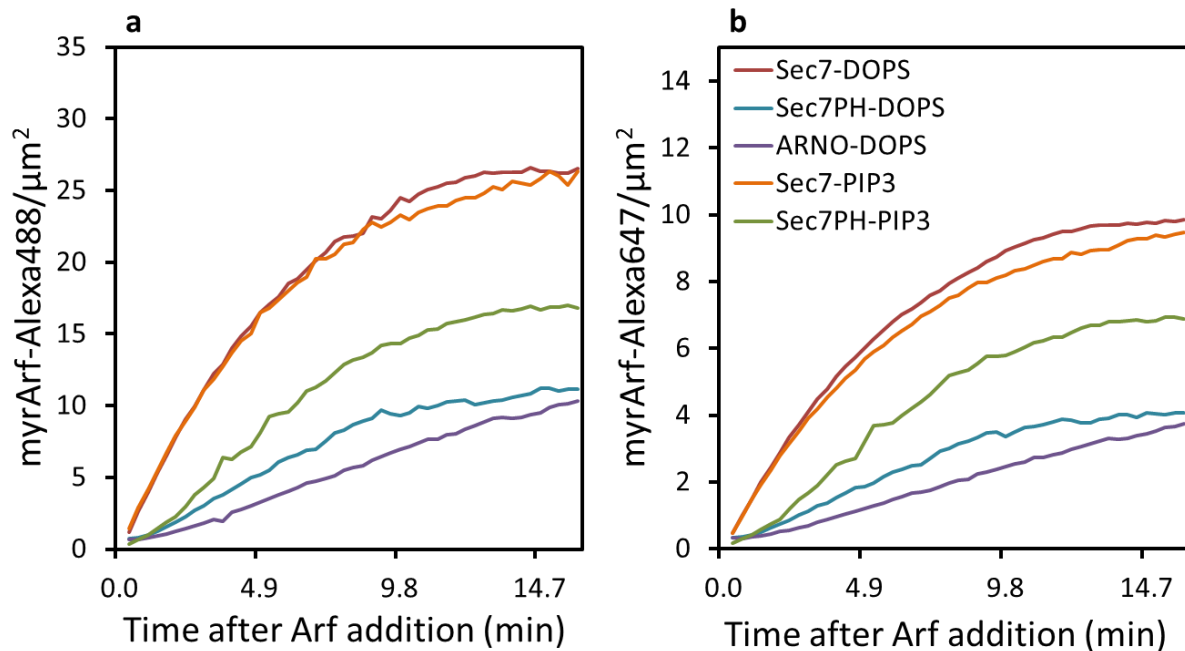
Figure 6.4. Recruitment and desorption of Arf to supported lipid bilayers with differing lipid compositions (either 10% DOPS or 4% PIP3) with GEF (ARNO, Sec7-PH, or Sec7). (**a**) Recruitment of myr-hArf1-Alexa488; (**b**) recruitment of myr-hArf1-Alexa647. Each trace is the average of at least three independent samples (excepting the Sec7-PIP3, which is the average of duplicate samples). Sec7 (the catalytic domain only) has the fastest exchange rate, which is independent on PIP3 lipids (as would be expected). The addition of PIP3 does relieve autoinhibition of the Sec7-PH domain, but not entirely to un-autoinhibited (Sec7) levels. Note that Arno has the slowest activation rate, near that of the Sec7-PH domain, and only about double the rate of Arf activation without GEF.

		488				647			
		k_f	Ratio	k_r	Ratio	k_f	Ratio	k_r	Ratio
no GEF	DOPS	1.81E-08	1	0.00116	1	6.30E-09	1	0.0012	1
	DOTAP	3.41E-09	0.19	0.00542	4.67	1.73E-09	0.27	0.00462	3.85
ARNO	DOPS	1.79E-07	9.89	0		6.24E-08	9.89	0	
Sec7-PH	DOPS	3.40E-07	18.8	0.00121	1.04	1.17E-07	18.6	0.00106	0.88
	PIP3	5.87E-07	32.5	0.00139	1.2	2.23E-07	35.4	0.0012	1
Sec7	DOPS	1.28E-06	70.9	0.00253	2.19	4.68E-07	74.2	0.00249	2.08
	PIP3	1.24E-06	68.4	0.00258	2.22	4.30E-07	68.2	0.00244	2.03

Table 6.1. The kinetic activation rates (forward and reverse) for Arf in all conditions, calculated using a unimolecular mass action model, with units of s^{-1}. Note that positively charged bilayers have only about 20-30% of the basal activation rate of negatively charged bilayers, while the desorption rate is increased by around a factor of 4. As compared to the no-GEF case, ARNO increases Arf activation by a factor of 10; the removal of the coiled-coil domain nearly doubles the activation, as Sec7-PH increases activation over the no-GEF condition by a factor of about 19; and the Sec7-PH activation is almost doubled by the inclusion of 4% PIP3 lipids; and Sec7 increases the activation of Arf by a factor of around 70, regardless of lipid composition.

a	b	c
Arf-GDP transiently binds to membrane	PH-domain partially blocks Sec7 domain binding to Arf	Membrane-bound myr-Arf-GTP

c	d	e
Arf-GDP transiently binds to membrane	GEF associates with lipids to bind to and activate Arf	Membrane-bound myr-Arf-GTP
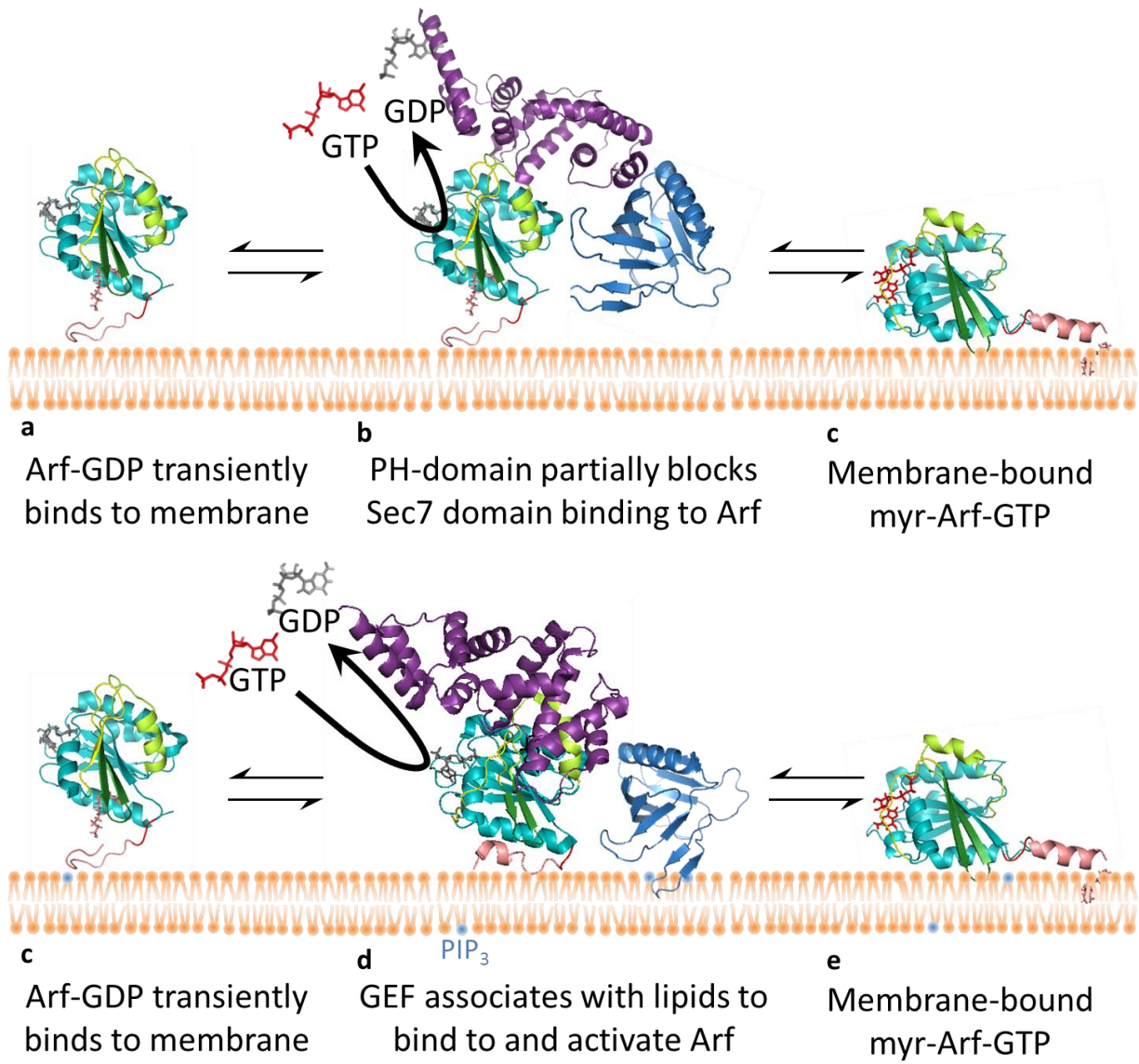
Figure 6.5. Schematic of Arf activation by ARNO in the presence or absence of PIP3.

106
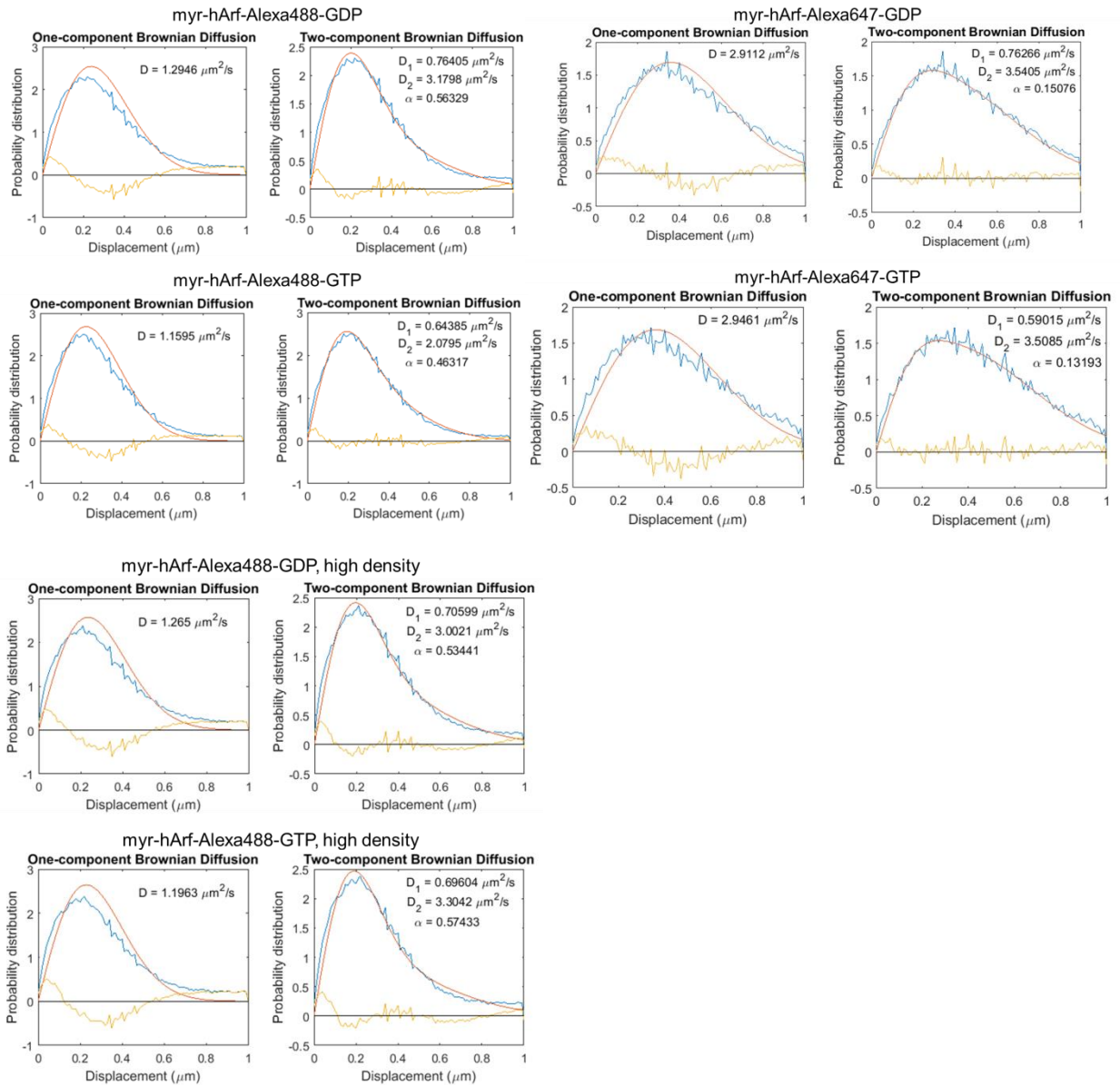
Figure 6.6. Arf diffusion is best fit by a two-component Brownian diffusion model in all cases.
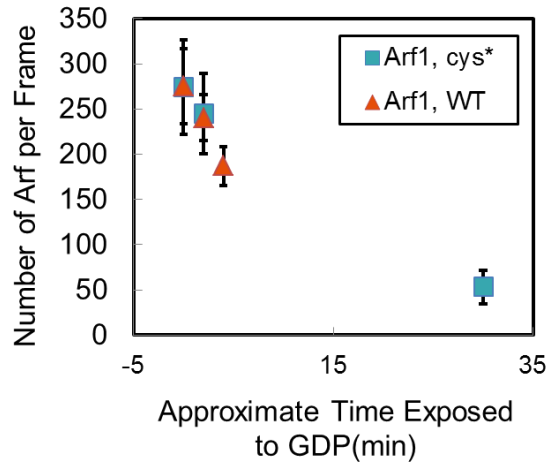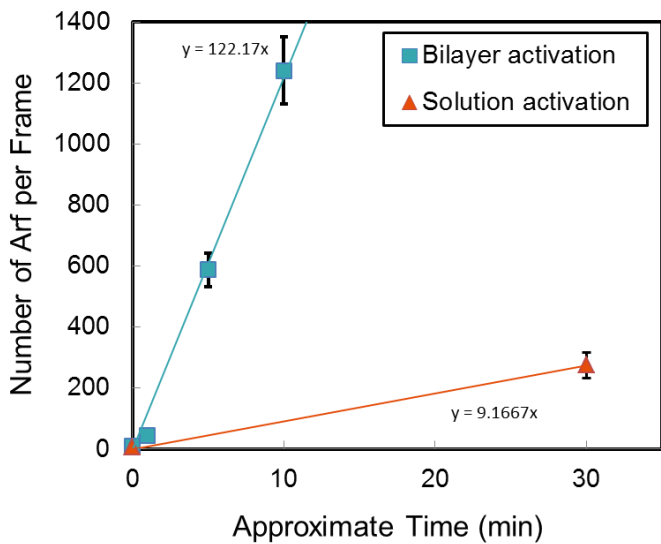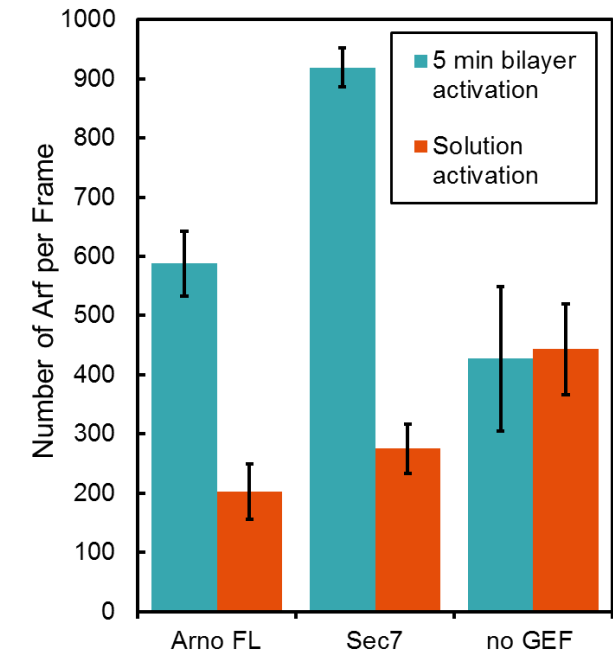
Figure 6.7. Native Arf and the cys* lite version used in this study have similar properties. Top: End-point recruitment data of dark myr-hArf1 from multiple positions on 1 sample, showing results consistent with the kinetic traces found with fluorescently labelled protein. Bottom left: Activation of protein on bilayer and in solution; bottom right: deactivation profile of Arf-WT and Arf-cys* show great consistency.
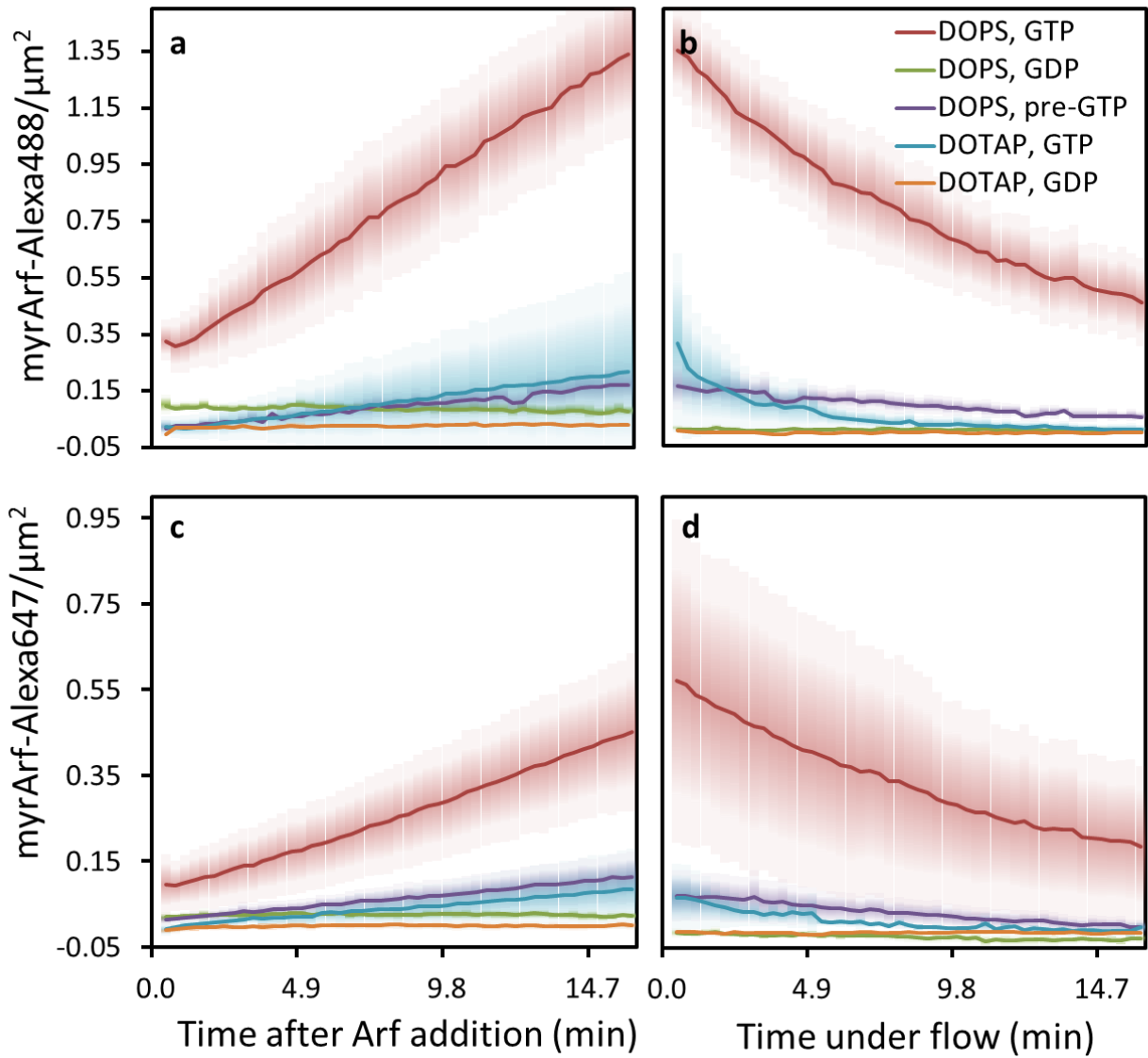
Figure 6.8. Figure 6.3, but with errors (SD) shown as lighter colored region. Differences between GDP/GTP and DOPS/DOTAP are clear, despite variability between samples.
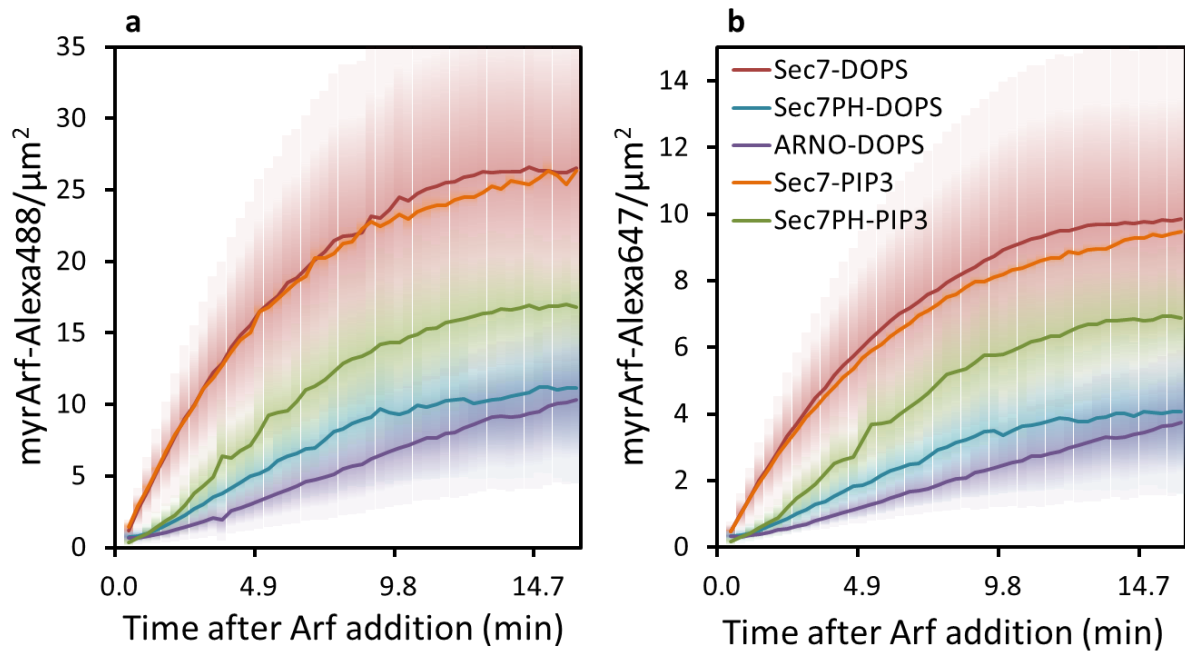
Figure 6.9. Figure 6.4, but with errors (SD) shown as lighter colored region. Differences between Sec7/(ARNO and Sec7-PH with DOPS) are clear; the increase in kinetic rate caused by PIP3 is not quite outside of SD windows, but is nonetheless highly suggestive.
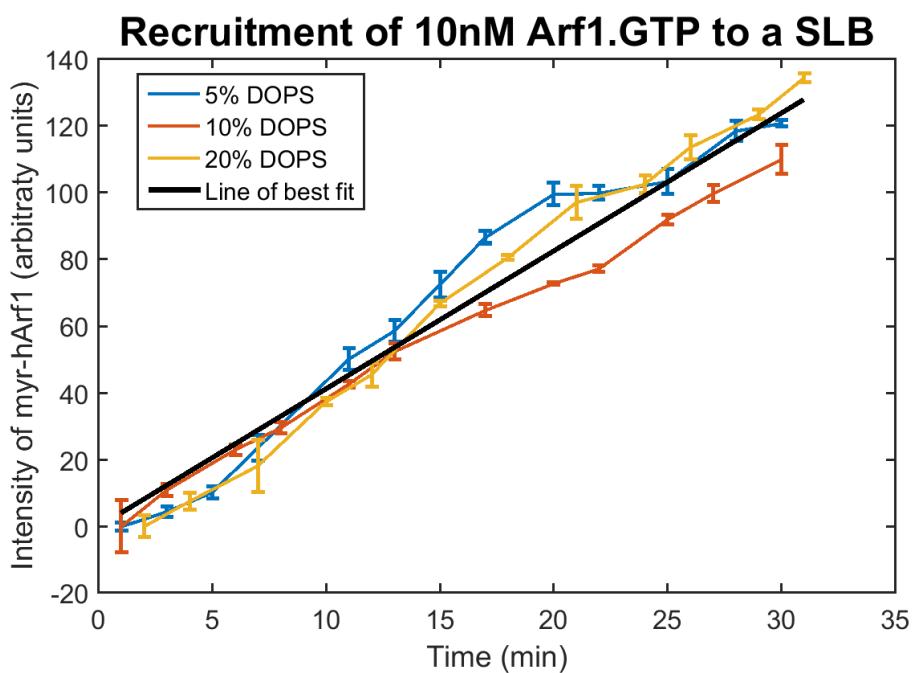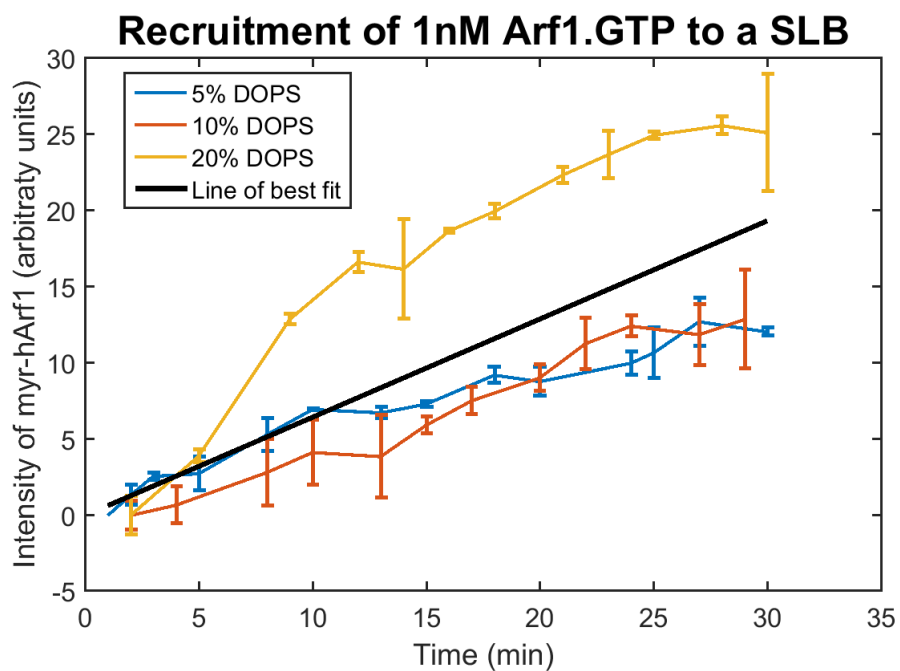
Figure 6.10. Arf recruits similarly to negatively charged bilayers, irrespective of charge intensity.
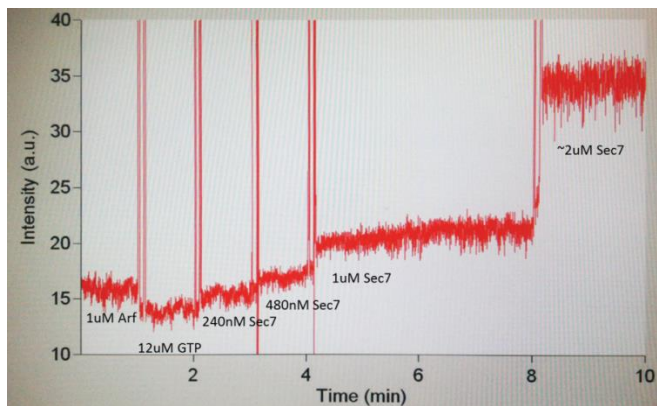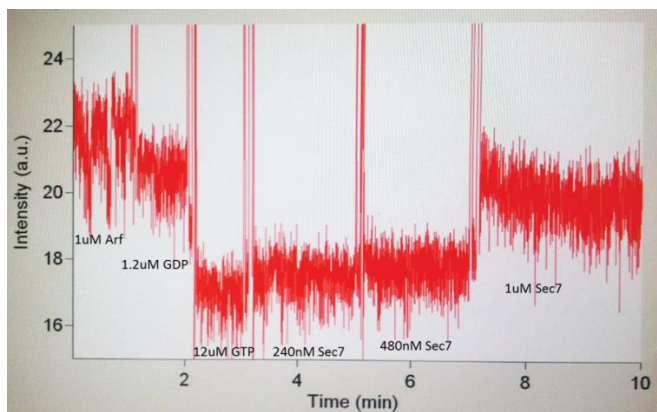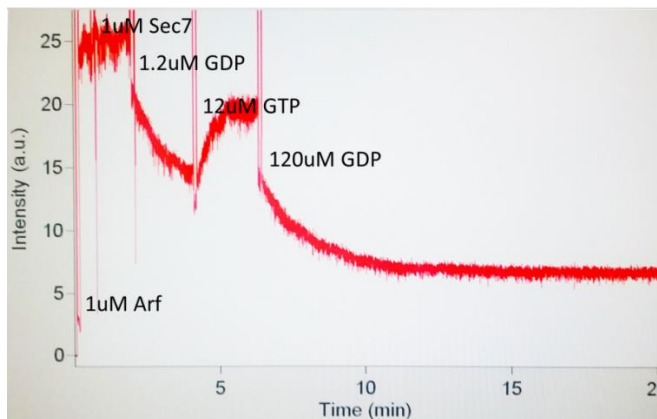
Figure 6.11. Confirmation of protein activity via Cary Eclipse spectrophotometer. Top: activation of Δ17-hArf1-his6 by Sec7 in solution. Middle: activation of dark myr-hArf1 by Sec7 in solution. Bottom: activation of dark myr-hArf1 by Sec7 on vesicles. Note that vesicles are required for robust activation of myristoylated protein.

CHAPTER 7.

CONCLUSIONS

In vitro membrane mimics, in combination with live cell measurements, provide a powerful tool to gain a deeper understanding about the activity and regulation of GTPases.

The kinetics of SOS activation of Ras was explored in three main ways. Firstly, a nanofabricated platform that incorporated liposome reaction chambers was developed to assess the kinetic activity of single SOS molecules with single nucleotide turnover resolution. This assay provides proof-of-concept for high-resolution exploration of other membrane-bound systems. Secondly, the measurement of SOS motility and localization in live cells contributed to an understanding of SOS regulation through a stable membrane-associated active state, resulting in SOS endocytosis. This clarifies the role of SOS in B-cell triggering. Thirdly, a small molecule inhibitor (DCAI) was shown to impact SOS activation of Ras through decreasing SOS^{cat} binding to Ras, both on membranes *in vitro* and in live cells transfected with FL-SOS-GFP. A similar recruitment study was also performed to assess the impact of oncogenic mutations on SOS, showing that these Ras mutations do in fact modulate effector binding. Additionally, the catalytic exchange rate for these mutations can also be lower than that of the WT case. These results can provide insight for future rational drug design targeting oncogenic Ras.

Finally, the kinetics of Arf-GTP and Arf-GDP membrane association were explored for the first time, and a SLB-based assay for GEF-mediated Arf recruitment studies was developed. Arf-GDP was shown to have a well-definable, but transient, interaction with a lipid membrane. Both Arf-GDP and Arf-GTP were shown to have a preference for binding to negative membranes over positive membranes. Also, the presence of GEF was shown to have a dramatic increase in the levels of Arf activation, particularly with the removal of autoinhibitory domains.

Directions for future study
High-throughput, membrane-based high-resolution techniques have yet to be developed. Although the nanofabricated platform used here (ZMWs) have been prepared for high-throughput in the industry setting by corporations like Pac Biosciences, inclusion of membrane mimics in high-throughput assays has proven more complex. One advantage of a liposome-based system as explored here is the reduced need to make SLBs, which can be technologically challenging at the high-throughput level. Since liposomes remain in solution until the last step, they could be dramatically easier to work with in a scaled-up setting. Using a high-throughput ZMW/liposome assay, other GTPases, or even membrane transport proteins, could be embedded into the SUVs and explored.

The impact of DCAI on SOS-mediated Ras catalytic rate is an interesting question that is still unanswered. While some data (unpublished) is suggestive that the catalytic rate is not impacted by DCAI, this is hard to reconcile with structural data that show a clear inhibition between Ras

and SOS at the catalytic site in the presence of DCAI. Higher-resolution data is needed to assess this.

While the impact of Ras oncogenes on SOS recruitment and activation has been studied at the bulk level, greater resolution of this process could be gained by using a Ras Binding Domain (RBD) assay to assess the difference between basal activation (activation of Ras by SOS in solution) and burst activation (where SOS is trapped and engages in a highly processive state). Either of these rates could be impacted by Ras mutations. Additionally, the probability of SOS engaging in the highly activated state could be altered. Further, exploration of the newly-suggested SOS mutations that are cancer-associated or cancer-causing using the recruitment and activation assay could be of great interest.

Given that the SLB assay demonstrated here can resolve both the transient Arf-GDP and stable Arf-GTP interactions with membranes, this assay introduces an exciting new platform for the exploration of the Arf system. Adding in Arf6, or increased concentrations of Arf1 to GEF activation assay with and without PIP3 would be quite interesting, to see if autoinhibition could be further relieved. Additionally, making more measurements with the full-length ARNO protein in comparison to the Sec7-PH domain could lead insight into the potential autoinhibitory role of the coiled-coil domain. Adding in fluorescently labelled fluorophore would allow for the Arf-GDP, Arf-GTP, and Arf-apo states to be distinguished, providing further resolution of the spatial and temporal regulation of Arf activation. In the presence of differing GEFs, Arf has been postulated to preferentially bind to areas of different curvature. This could be experimentally tested in a self-contained SLB assay on a micro- or nano-fabricated substrate that included both curved and planar regions.

REFERNCES

(1)   van Meer, G.; Voelker, D. R.; Feigenson, G. W. Membrane Lipids: Where They Are and How They Behave. *Nat. Rev. Mol. Cell Biol.* **2008**, *9* (2), 112–124.

(2)   DiNitto, J. P.; Cronin, T. C.; Lambright, D. G. Membrane Recognition and Targeting by Lipid-Binding Domains. *Sci. STKE* **2003**, *2003* (213), re16.

(3)   Vonkova, I.; Saliba, A.-E.; Deghou, S.; Anand, K.; Ceschia, S.; Doerks, T.; Galih, A.; Kugler, K. G.; Maeda, K.; Rybin, V.; et al. Lipid Cooperativity as a General Membrane-Recruitment Principle for PH Domains. *Cell Rep.* **2015**, 1–12.

(4)   Lemmon, M. a; Ferguson, K. M.; O'Brien, R.; Sigler, P. B.; Schlessinger, J. Specific and High-Affinity Binding of Inositol Phosphates to an Isolated Pleckstrin Homology Domain. *Proc. Natl. Acad. Sci. U. S. A.* **1995**, *92* (23), 10472–10476.

(5)   Rocks, O.; Gerauer, M.; Vartak, N.; Koch, S.; Huang, Z.-P.; Pechlivanis, M.; Kuhlmann, J.; Brunsveld, L.; Chandra, A.; Ellinger, B.; et al. The Palmitoylation Machinery Is a Spatially Organizing System for Peripheral Membrane Proteins. *Cell* **2010**, *141* (3), 458–471.

(6)   McCloskey, M. a; Poo, M. M. Rates of Membrane-Associated Reactions: Reduction of Dimensionality Revisited. *J. Cell Biol.* **1986**, *102* (1), 88–96.

(7)   Berg, H. C. *Random Walks in Biology*; Princeton University Press, 1983.

(8)   Childress, S. Chapter 7: Stokes Flow. In *Fluid Dynamics*; NYU Mathematics Department: New York, 2007.

(9)   Saffman, P. G.; Delbruck, M.; Delbrück, M. Brownian Motion in Biological Membranes. *Proc Natl Acad Sci USA* **1975**, *72* (8), 3111–3113.

(10)   Abney, J. R.; Scalettar, B. A.; Owicki, J. C. Self Diffusion of Interacting Membrane Proteins. *Biophys. J.* **1989**, *55* (5), 817–833.

(11)   Marčelja, S. Lipid-Mediated Protein Interaction in Membranes. *BBA - Biomembr.* **1976**, *455* (1), 1–7.

(12)   Almeida, P.; Vaz, W. Lateral Diffusion in Membranes. In *Handbook of Biological Physics*; Lipowsky, R., Sackman, E., Eds.; Elsevier, 1995; Vol. 1, pp 306–357.

(13)   Sigurdsson, J. K.; Brown, F. L. H.; Atzberger, P. J. Hybrid Continuum-Particle Method for Fluctuating Lipid Bilayer Membranes with Diffusing Protein Inclusions. *J. Comput. Phys.* **2013**, *252*, 65–85.

(14)   Simons, K.; Ikonen, E. Functional Rafts in Cell Membranes. *Nature* **1997**, *387* (6633), 569–572.

(15)   Baumgart, T.; Hess, S. T.; Webb, W. W. Imaging Coexisting Fluid Domains in Biomembrane Models Coupling Curvature and Line Tension. *Nature* **2003**, *425* (October), 821–824.

(16)   Wit, G. De; Danial, J. S. H.; Kukura, P.; Wallace, M. I. Dynamic Label-Free Imaging of Lipid Nanodomains. **2015**, *2015* (24), 3–7.

(17)   Lingwood, D.; Simons, K. Lipid Rafts as a Membrane-Organizing Principle. *Science* **2010**, *327* (2010), 46–50.

(18)   Veatch, S. L.; Cicuta, P.; Sengupta, P.; Honerkamp-smith, A.; Holowka, D.; Baird, B. Critical Fluctuations in Plasma Membrane Vesicles †. **2008**, *3* (5), 287–293.

(19)   Mueller, V.; Ringemann, C.; Honigmann, a; Schwarzmann, G.; Medda, R.; Leutenegger, M.; Polyakova, S.; Belov, V. N.; Hell, S. W.; Eggeling, C. STED Nanoscopy Reveals Molecular Details of Cholesterol- and Cytoskeleton-Modulated Lipid Interactions in Living Cells. *Biophys. J.* **2011**, *101* (7), 1651–1660.

(20)   Frisz, J. F.; Klitzing, H. a; Lou, K.; Hutcheon, I. D.; Weber, P. K.; Zimmerberg, J.; Kraft, M. L. Sphingolipid Domains in the Plasma Membranes of Fibroblasts Are Not Enriched with Cholesterol. *J. Biol. Chem.* **2013**, *288* (23), 16855–16861.

(21)   Frisz, J. F.; Lou, K.; Klitzing, H. a; Hanafin, W. P.; Lizunov, V.; Wilson, R. L.; Carpenter, K. J.; Kim, R.; Hutcheon, I. D.; Zimmerberg, J.; et al. Direct Chemical Evidence for Sphingolipid Domains in the Plasma Membranes of Fibroblasts. *Proc. Natl. Acad. Sci. U. S. A.* **2013**, *110* (8), E613-22.

(22)   Kraft, M. L. Plasma Membrane Organization and Function: Moving Past Lipid Rafts. *Mol. Biol. Cell* **2013**, *24* (18), 2765–2768.

(23)   Astro, V.; Curtis, I. De. Plasma Membrane – Associated Platforms : Dynamic Scaffolds That Organize Membrane-Associated Events. **2015**, *8* (367), 1–12.

(24)   Fujita, A.; Cheng, J.; Fujimoto, T. Segregation of GM1 and GM3 Clusters in the Cell Membrane Depends on the Intact Actin Cytoskeleton. *Biochim. Biophys. Acta - Mol. Cell Biol. Lipids* **2009**, *1791* (5), 388–396.

(25)   Fujiwara, T. K.; Iwasawa, K.; Kalay, Z.; Tsunoyama, T. A.; Watanabe, Y.; Umemura, Y. M.; Murakoshi, H.; Suzuki, K. G. N.; Nemoto, Y. L.; Morone, N.; et al. Confined Diffusion of Transmembrane Proteins and Lipids Induced by the Same Actin Meshwork Lining the Plasma Membrane. *Mol. Biol. Cell* **2016**, *27*, 11–81.

(26) Kusumi, A.; Nakada, C.; Ritchie, K.; Murase, K.; Suzuki, K.; Murakoshi, H.; Kasai, R. S.; Kondo, J.; Fujiwara, T. Paradigm Shift of the Plasma Membrane Concept from the Two-Dimensional Continuum Fluid to the Partitioned Fluid: High-Speed Single-Molecule Tracking of Membrane Molecules. *Annu. Rev. Biophys. Biomol. Struct.* **2005**, *34*, 351–378.

(27) Honigmann, A.; Sadeghi, S.; Keller, J.; Hell, S. W.; Eggeling, C.; Vink, R. A Lipid Bound Actin Meshwork Organizes Liquid Phase Separation in Model Membranes. *Elife* **2014**, *2014*, 1–16.

(28) Gowrishankar, K.; Ghosh, S.; Saha, S.; C, R.; Mayor, S.; Rao, M. Active Remodeling of Cortical Actin Regulates Spatiotemporal Organization of Cell Surface Molecules. *Cell* **2012**, *149* (6), 1353–1367.

(29) Arumugam, S.; Petrov, E. P.; Schwille, P. Cytoskeletal Pinning Controls Phase Separation in Multicomponent Lipid Membranes. *Biophys. J.* **2015**, *108* (5), 1104–1113.

(30) Raghupathy, R.; Anilkumar, A. A.; Polley, A.; Singh, P. P.; Yadav, M.; Johnson, C.; Suryawanshi, S.; Saikam, V.; Sawant, S. D.; Panda, A.; et al. Transbilayer Lipid Interactions Mediate Nanoclustering of Lipid-Anchored Proteins. *Cell* **2015**, *161* (3), 581–594.

(31) Lee, I.-H.; Saha, S.; Polley, A.; Huang, H.; Mayor, S.; Rao, M.; Groves, J. T. Live Cell Plasma Membranes Do Not Exhibit a Miscibility Phase Transition over a Wide Range of Temperatures. *The Journal of Physical Chemistry B*. March 26, 2015.

(32) Huang, W. Y. C.; Yan, Q.; Lin, W.-C.; Chung, J. K.; Hansen, S. D.; Christensen, S. M.; Tu, H.-L.; Kuriyan, J.; Groves, J. T. Phosphotyrosine-Mediated LAT Assembly on Membranes Drives Kinetic Bifurcation in Recruitment Dynamics of the Ras Activator SOS. *Proceedings of the National Academy of Sciences*. July 21, 2016.

(33) Su, X.; Ditlev, J. A.; Hui, E.; Xing, W.; Banjade, S.; Okrut, J.; King, D. S.; Taunton, J.; Rosen, M. K.; Vale, R. D. Phase Separation of Signaling Molecules Promotes T Cell Receptor Signal Transduction. *Science (80-.).* **2016**, *352* (6285), 595–600.

(34) Wennerberg, K.; Rossman, K. L.; Der, C. J. The Ras Superfamily at a Glance. *J. Cell Sci.* **2005**, *118* (Pt 5), 843–846.

(35) Bourne, H. R.; Sanders, D. A.; McCormick, F. The GTPase Superfamily: A Conserved Switch for Diverse Cell Functions. *Nature*. 1990, pp 125–132.

(36) Bourne, H. R.; Sanders, D. A.; McCormick, F. The GTPase Superfamily: Conserved Structure and Molecular Mechanism. *Nature* **1991**, *349* (6305), 117–127.

(37)   Li, G.; Zhang, X. C. GTP Hydrolysis Mechanism of Ras-like GTPases. *J. Mol. Biol.* **2004**, *340* (5), 921–932.

(38)   Gureasko, J.; Galush, W. J.; Boykevisch, S.; Sondermann, H.; Bar-Sagi, D.; Groves, J. T.; Kuriyan, J. Membrane-Dependent Signal Integration by the Ras Activator Son of Sevenless. *Nat. Struct. {&} Mol. Biol.* **2008**, *15* (5), 452–461.

(39)   Cherfils, J.; Zeghouf, M. Regulation of Small GTPases by GEFs, GAPs, and GDIs. *Physiol. Rev.* **2013**, *93* (1), 269–309.

(40)   Jaffe, A. B.; Hall, A. Rho GTPases: Biochemistry and Biology. *Annu. Rev. Cell Dev. Biol.* **2005**, *21*, 247–269.

(41)   Grosshans, B. L.; Ortiz, D.; Novick, P. Rabs and Their Effectors: Achieving Specificity in Membrane Traffic. *Proc. Natl. Acad. Sci. U. S. A.* **2006**, *103* (32), 11821–11827.

(42)   Clarke, P. R.; Zhang, C. Spatial and Temporal Coordination of Mitosis by Ran GTPase. *Nat. Rev. Mol. Cell Biol.* **2008**, *9* (6), 464–477.

(43)   Pasqualato, S.; Renault, L.; Cherfils, J. Arf, Arl, Arp and Sar Proteins: A Family of GTP-Binding Proteins with a Structural Device for "Front-Back" Communication. *EMBO Rep.* **2002**, *3* (11), 1035–1041.

(44)   Jackson, C. L.; Bouvet, S. Arfs at a Glance. **2014**, *127*, 4103–4109.

(45)   Goitre, L.; Trapani, E.; Trabalzini, L.; Retta, S. F. The Ras Superfamily of Small GTPases: The Unlocked Secrets. In *Ras Signaling: Methods and Protocols*; 2014; Vol. 1120, pp 253–261.

(46)   Donaldson, J. G.; Jackson, C. L. ARF Family G Proteins and Their Regulators: Roles in Membrane Transport, Development and Disease. *Nat. Rev. Mol. Cell Biol.* **2011**, *12* (6), 362–375.

(47)   Ben-Tekaya, H.; Kahn, R. A.; Hauri, H.-P. ADP Ribosylation Factors 1 and 4 and Group VIA Phospholipase A2 Regulate Morphology and Intraorganellar Traffic in the Endoplasmic Reticulum-Golgi Intermediate Compartment. *Mol. Biol. Cell* **2010**, *21* (23), 4130–4140.

(48)   D'Souza-Schorey, C.; Chavrier, P. ARF Proteins: Roles in Membrane Traffic and beyond. *Nat. Rev. Mol. Cell Biol.* **2006**, *7* (5), 347–358.

(49)   Reuther, G. W.; Der, C. J. The Ras Branch of Small GTPases: Ras Family Members Don't Fall far from the Tree. *Curr. Opin. Cell Biol.* **2000**, *12* (2), 157–165.

(50)   Cox, A. D.; Fesik, S. W.; Kimmelman, A. C.; Luo, J.; Der, C. J. Drugging the

Undruggable RAS: Mission Possible? *Nat. Rev. Drug Discov.* **2014**, *13* (11), 828–851.

(51) Prior, I. A.; Lewis, P. D.; Mattos, C. A Comprehensive Survey of Ras Mutations in Cancer. *Cancer Res.* **2012**, *72* (10), 2457–2467.

(52) Wittinghofer, A.; Gremer, L.; Gilsbach, B.; Reza Ahmadian, M. Fluoride Complexes of Oncogenic Ras Mutants to Study the Ras-RasGAP Interaction. *Biol. Chem.* **2008**, *389* (9), 1163–1171.

(53) Smith, M. J.; Neel, B. G.; Ikura, M. NMR-Based Functional Profiling of RASopathies and Oncogenic RAS Mutations. *PNAS* **2013**, *110* (12), 4574–4579.

(54) Hancock, J. F. Ras Proteins: Different Signals from Different Locations. *Nat. Rev. Mol. Cell Biol.* **2003**, *4* (5), 373–384.

(55) Chandra, A.; Grecco, H. E.; Pisupati, V.; Perera, D.; Cassidy, L.; Skoulidis, F.; Ismail, S. a; Hedberg, C.; Hanzal-Bayer, M.; Venkitaraman, A. R.; et al. The GDI-like Solubilizing Factor PDEδ Sustains the Spatial Organization and Signalling of Ras Family Proteins. *Nat. Cell Biol.* **2012**, *14* (2), 148–158.

(56) Konstantinopoulos, P. a; Karamouzis, M. V; Papavassiliou, A. G. Post-Translational Modifications and Regulation of the RAS Superfamily of GTPases as Anticancer Targets. *Nat. Rev. Drug Discov.* **2007**, *6* (7), 541–555.

(57) Rubio, I.; Downward, J. Ras Activation Revisited. **2001**, *1*.

(58) Lowy, D. R.; Willumsen, B. M. Function and Regulation of Ras. *Annu. Rev. Biochem.* **1993**, *62*, 851–891.

(59) Das, J.; Ho, M.; Zikherman, J.; Govern, C.; Yang, M.; Weiss, A.; Chakraborty, A. K.; Roose, J. P. Digital Signaling and Hysteresis Characterize Ras Activation in Lymphoid Cells. *Cell* **2009**, *136* (2), 337–351.

(60) Iversen, L.; Tu, H.; Lin, W.; Christensen, S. M.; Steven, M.; Hansen, S. D.; Thill, P.; Yu, C.; Stamou, D.; Chakraborty, A. K. Single Molecule Analysis of Ras Activation by SOS Reveals Allosteric Regulation via Altered Fluctuation Dynamics. **2014**.

(61) Gureasko, J.; Kuchment, O.; Makino, D. L.; Sondermann, H.; Bar-Sagi, D.; Kuriyan, J. Role of the Histone Domain in the Autoinhibition and Activation of the Ras Activator Son of Sevenless. *Proc. Natl. Acad. Sci. U. S. A.* **2010**, *107* (8), 3430–3435.

(62) Lee, Y. K.; Low-nam, S. T.; Chung, J.; Hansen, S. D.; Lam, M.; Alvarez, S.; Groves, J. T. Mechanism of SOS PR-Domain Autoinhibition Revealed by Single-Molecule Assays on Native Protein from Lysate. *Nature Communications*. April 28, 2017.

(63) Sjölin-goodfellow, H.; Frushicheva, M. P.; Ji, Q.; Cheng, D. A.; Kadlecek, T. A.; Cantor, A. J.; Kuriyan, J. The Catalytic Activity of the Kinase ZAP-70 Mediates Basal Signaling and Negative Feedback of the T Cell Receptor Pathway. **2015**, *8* (377), 1–14.

(64) Mor, A.; Philips, M. R. Compartmentalized Ras/Mapk Signaling. *Annu. Rev. Immunol.* **2006**, *24* (1), 771–800.

(65) Ahearn, I. M.; Haigis, K.; Bar-Sagi, D.; Philips, M. R. Regulating the Regulator: Post-Translational Modification of RAS. *Nat. Rev. Mol. Cell Biol.* **2012**, *13* (1), 39–51.

(66) Seu, K. J.; Pandey, A. P.; Haque, F.; Proctor, E. a; Ribbe, A. E.; Hovis, J. S. Effect of Surface Treatment on Diffusion and Domain Formation in Supported Lipid Bilayers. *Biophys. J.* **2007**, *92* (7), 2445–2450.

(67) Lipowsky, R. The Conformation of Membranes. *Nature* **1991**, *349*, 475–481.

(68) Larsen, J.; Hatzakis, N. S.; Stamou, D. Observation of Inhomogeneity in the Lipid Composition of Individual Nanoscale Liposomes. *J. Am. Chem. Soc.* **2011**, *133*, 10685–10687.

(69) Kunding, A. H.; Mortensen, M. W.; Christensen, S. M.; Stamou, D. A Fluorescence-Based Technique to Construct Size Distributions from Single-Object Measurements: Application to the Extrusion of Lipid Vesicles. *Biophys. J.* **2008**, *95* (3), 1176–1188.

(70) Christensen, S. M.; Stamou, D. Surface-Based Lipid Vesicle Reactor Systems: Fabrication and Applications. *Soft Matter* **2007**, *3* (7), 828.

(71) Lin, W.-C.; Yu, C.-H.; Triffo, S.; Groves, J. T. Supported Membrane Formation, Characterization, Functionalization, and Patterning for Application in Biological Science and Technology. *Curr. Protoc. Chem. Biol.* **2010**, *2* (December), 235–269.

(72) Israelachvili, J. *Intermolecular & Surface Forces*, Second Edi.; Academic Press: San Francisco, 1992.

(73) Bayburt, T. H.; Silgar, S. G. Membrane Protein Assembly into Nanodiscs. *FEBS Lett.* **2010**, *584* (9), 1721–1727.

(74) Pollard, T. D. A Guide to Simple and Informative Binding Assays. *Mol. Biol. Cell* **2010**, *21* (23), 4061–4067.

(75) Fish, K. N. Total Internal Reflection Fluorescence (TIRF) Microscopy. *Curr. Protoc. Cytom.* **2009**, *Chapter 12* (October), Unit12.18.

(76) Davidson, M. W.; Fellers, T. J. Understanding Conjugate Planes and Kohler Illumination. *Aperture* **2002**, 4.

(77)   North, A. J. Seeing Is Believing? A Beginners' Guide to Practical Pitfalls in Image Acquisition. *J. Cell Biol.* **2006**, *172* (1), 9–18.

(78)   Abramowitz, M. *Fluorescence Microscopy: The Essentials*, Volume 4,.; Olympus America: Melville, NY, 1993.

(79)   Ogunyankin, M. O.; Huber, D. L.; Sasaki, D. Y.; Longo, M. L. Nanoscale Patterning of Membrane-Bound Proteins Formed through Curvature-Induced Partitioning of Phase-Specific Receptor Lipids. *Langmuir* **2013**, *29* (20), 6109–6115.

(80)   Hirano-Iwata, A.; Aoto, K.; Oshima, A.; Taira, T.; Yamaguchi, R.; Kimura, Y.; Niwano, M. Free-Standing Lipid Bilayers in Silicon Chips-Membrane Stabilization Based on Microfabricated Apertures with a Nanometer-Scale Smoothness. *Langmuir* **2010**, *26* (3), 1949–1952.

(81)   Nair, P. M.; Salaita, K.; Petit, R. S.; Groves, J. T. Using Patterned Supported Lipid Membranes to Investigate the Role of Receptor Organization in Intercellular Signaling. *Nat. Protoc.* **2011**, *6* (4), 523–539.

(82)   Lohmüller, T.; Iversen, L.; Schmidt, M.; Rhodes, C.; Tu, H.-L.; Lin, W.-C.; Groves, J. T. Single Molecule Tracking on Supported Membranes with Arrays of Optical Nanoantennas. *Nano Lett.* **2012**, *12* (3), 1717–1721.

(83)   Gupta, A.; Khalil, A. S. G.; Winterer, M.; Wiggers, H. Stable Colloidal Dispersions of Silicon Nanoparticles for the Fabrication of Films Using Inkjet Printing Technology. *INEC 2010 - 2010 3rd Int. Nanoelectron. Conf. Proc.* **2010**, 1018–1019.

(84)   Bernard, A.; Bietsch, A.; Renault, J.; Wolf, H. Printing Meets Lithography : Soft Approaches to High-Resolution Patterning. **2001**, *45* (5), 697–719.

(85)   Watt, F.; Bettiol, A. A.; Van Kan, J. A.; Teo, E. J.; Breese, M. B. H. Ion Beam Lithography and Nanofabriation: A Review. *Int. J. Nanosci.* **2005**, *4* (3), 269–286.

(86)   Gates, B. D.; Xu, Q.; Stewart, M.; Ryan, D.; Willson, C. G.; Whitesides, G. M. New Approaches to Nanofabrication : Molding , Printing , and Other Techniques. **2010**, No. 617.

(87)   Henriques, R.; Griffiths, C.; Hesper Rego, E.; Mhlanga, M. M. PALM and STORM: Unlocking Live-Cell Super-Resolution. *Biopolymers* **2011**, *95* (5), 322–331.

(88)   Xie, X. S.; Choi, P. J.; Li, G.-W.; Lee, N. K.; Lia, G. Single-Molecule Approach to Molecular Biology in Living Bacterial Cells. *Annu. Rev. Biophys.* **2008**, *37* (February), 417–444.

(89)   Chen, B.-C.; Legant, W. R.; Wang, K.; Shao, L.; Milkie, D. E.; Davidson, M. W.;

Janetopoulos, C.; Wu, X. S.; Hammer, J. A.; Liu, Z.; et al. Lattice Light-Sheet Microscopy: Imaging Molecules to Embryos at High Spatiotemporal Resolution. *Science (80-.).* **2014**, *346* (6208), 1257998–1257998.

(90)   Wei, L.; Chen, Z.; Shi, L.; Long, R.; Andrew, V.; Zhang, L.; Hu, F.; Yuste, R. Super-Multiplex Vibrational Imaging. *Nature* **2017**, 1–19.

(91)   Valm, A. M.; Cohen, S.; Legant, W. R.; Melunis, J.; Hershberg, U.; Wait, E.; Cohen, A. R.; Davidson, M. W.; Betzig, E.; Lippincott-Schwartz, J. Applying Systems-Level Spectral Imaging and Analysis to Reveal the Organelle Interactome. *Nature* **2017**, *546* (7656), 162–167.

(92)   Huang, B.; Jones, S. a; Brandenburg, B.; Zhuang, X. Whole-Cell 3D STORM Reveals Interactions between Cellular Structures with Nanometer-Scale Resolution. *Nat. Methods* **2008**, *5* (12), 1047–1052.

(93)   Christensen, S. M.; Triplet, M. G.; Rhodes, C. R.; Iwig, J. S.; Tu, H.; Stamou, D.; Groves, J. T. Monitoring the Waiting Time Sequence of Single Ras GTPase Activation Events Using Liposome Functionalized Zero-Mode Waveguides. *Nano Lett.* **2016**, *16* (4), 2890–2895.

(94)   Cherfils, J.; Zeghouf, M. Chronicles of the GTPase Switch. *Nat. Chem. Biol.* **2011**, *7* (8), 493–495.

(95)   Barr, F.; Lambright, D. G. Rab GEFs and GAPs. **2010**, *22* (4), 461–470.

(96)   Pylayeva-Gupta, Y.; Grabocka, E.; Bar-Sagi, D. RAS Oncogenes: Weaving a Tumorigenic Web. *Nat. Rev. Cancer* **2011**, *11* (11), 761–774.

(97)   McCormick, F. Signal Transduction. How Receptors Turn Ras On. *Nature* **1993**, *363* (6424), 15.

(98)   Jun, J. E.; Yang, M.; Chen, H.; Chakraborty, A. K.; Roose, J. P. *Activation of Extracellular Signal-Regulated Kinase but Not of p38 Mitogen-Activated Protein Kinase Pathways in Lymphocytes Requires Allosteric Activation of SOS.*; 2013; Vol. 33.

(99)   Bos, J.; Rehmann, H.; Wittinghofer, A. GEFs and GAPs : Critical Elements in the Control of Small G Proteins. *Cell* **2007**, 865–877.

(100) Findlay, G. M.; Pawson, T. How Is SOS Activated? Let Us Count the Ways. *Nat. Struct. Mol. Biol.* **2008**, *15* (6), 538–540.

(101) Karnoub, A. E.; Weinberg, R. A. Ras Oncogenes: Split Personalities. *Nat. Rev. Mol. Cell Biol.* **2008**, *9* (7), 517–531.

(102) Tartaglia, M.; Pennacchio, L. a; Zhao, C.; Yadav, K. K.; Fodale, V.; Sarkozy, A.; Pandit, B.; Oishi, K.; Martinelli, S.; Schackwitz, W.; et al. Gain-of-Function SOS1 Mutations Cause a Distinctive Form of Noonan Syndrome. *Nat. Genet.* **2007**, *39* (1), 75–79.

(103) Roberts, A. E.; Araki, T.; Swanson, K. D.; Montgomery, K. T.; Schiripo, T. a; Joshi, V. a; Li, L.; Yassin, Y.; Tamburino, A. M.; Neel, B. G.; et al. Germline Gain-of-Function Mutations in SOS1 Cause Noonan Syndrome. *Nat. Genet.* **2007**, *39* (1), 70–74.

(104) Tumurkhuu, M.; Saitoh, M.; Takita, J.; Mizuno, Y.; Mizuguchi, M. A Novel SOS1 Mutation in Costello/CFC Syndrome Affects Signaling in Both RAS and PI3K Pathways. *J. Recept. Signal Transduct. Res.* **2013**, *33* (2), 124–128.

(105) Thompson, H. Pipeline for COPD Drugs Flows with Combination Candidates. *Nat. Med.* **2013**, *19* (9), 1079.

(106) Stephen, A. G.; Esposito, D.; Bagni, R. K.; Mccormick, F. Dragging Ras Back in the Ring. *Cancer Cell* **2014**, *25* (3), 272–281.

(107) Wang, W.; Fang, G.; Rudolph, J. Ras Inhibition via Direct Ras Binding - Is There a Path Forward? *Bioorganic Med. Chem. Lett.* **2012**, *22* (18), 5766–5776.

(108) Patgiri, A.; Yadav, K. K.; Arora, P. S.; Bar-Sagi, D. An Orthosteric Inhibitor of the Ras-Sos Interaction. *Nat. Chem. Biol.* **2011**, *7* (9), 585–587.

(109) Maurer, T.; Garrenton, L. S.; Oh, A.; Pitts, K.; Anderson, D. J.; Skelton, N. J.; Fauber, B. P.; Pan, B.; Malek, S.; Stokoe, D.; et al. Small-Molecule Ligands Bind to a Distinct Pocket in Ras and Inhibit SOS-Mediated Nucleotide Exchange Activity. *Proc. Natl. Acad. Sci.* **2012**, *109* (14), 5299–5304.

(110) English, B. P.; Min, W.; van Oijen, A. M.; Lee, K. T.; Luo, G.; Sun, H.; Cherayil, B. J.; Kou, S. C.; Xie, X. S. Ever-Fluctuating Single Enzyme Molecules: Michaelis-Menten Equation Revisited. *Nat. Chem. Biol.* **2006**, *2* (2), 87–94.

(111) Engelkamp, H.; Hatzakis, N. S.; Hofkens, J.; De Schryver, F. C.; Nolte, R. J. M.; Rowan, A. E.; Vries, R. P. de; Kester, H. C. M.; Poulsen, C. H.; Benen, J. A. E.; et al. Do Enzymes Sleep and Work? *Chem. Commun.* **2006**, *327* (9), 935.

(112) Lu, H. P. Sizing up Single-Molecule Enzymatic Conformational Dynamics. *Chem. Soc. Rev.* **2014**, *43* (4), 1118–1143.

(113) Moffitt, J. R.; Chemla, Y. R.; Smith, S. B.; Bustamante, C. Recent Advances in Optical Tweezers. *Annu. Rev. Biochem.* **2008**, *77*, 205–228.

(114) Lu, H. P.; Xun, L.; Xie, X. S. Single-Molecule Enzymatic Dynamics. *Science* **1998**, *282* (December), 1877–1882.

(115) Choi, Y.; Moody, I. S.; Sims, P. C.; Hunt, S. R.; Corso, B. L.; Perez, I.; Weiss, G. a; Collins, P. G. Single-Molecule Lysozyme Dynamics Monitored by an Electronic Circuit. *Science* **2012**, *335* (6066), 319–324.

(116) Iversen L; Tu HL; Lin WC; Christensen SM; Abel SM; Iwig J; Wu HJ; Gureasko J; Rhodes C; Petit RS; et al. Ras Activation by SOS: Allosteric Regulation by Altered Fluctuation Dynamics. *Science* **2014**, *345*, 50–54.

(117) Zhu, P.; Craighead, H. G. Zero-Mode Waveguides for Single-Molecule Analysis. **2012**.

(118) Levene, M. J.; Korlach, J.; Turner, S. W.; Foquet, M.; Craighead, H. G.; Webb, W. W. Zero-Mode Waveguides for Single-Molecule Analysis at High Concentrations. *Science* **2003**, *299* (5607), 682–686.

(119) Eid, J.; Fehr, A.; Gray, J.; Luong, K.; Lyle, J.; Otto, G.; Peluso, P.; Rank, D.; Baybayan, P.; Bettman, B.; et al. Single Polymerase Molecules. *Exch. Organ. Behav. Teach. J.* **2009**, No. January, 133–138.

(120) Uemura, S.; Aitken, C. E.; Korlach, J.; Flusberg, B. a; Turner, S. W.; Puglisi, J. D. Real-Time tRNA Transit on Single Translating Ribosomes at Codon Resolution. *Nature* **2010**, *464* (7291), 1012–1017.

(121) Sameshima, T.; Iizuka, R.; Ueno, T.; Wada, J.; Aoki, M.; Shimamoto, N.; Ohdomari, I.; Tanii, T.; Funatsu, T. Single-Molecule Study on the Decay Process of the Football-Shaped GroEL-GroES Complex Using Zero-Mode Waveguides. *J. Biol. Chem.* **2010**, *285* (30), 23159–23164.

(122) Tamm, L. K.; Groves, J. T. Supported Membranes in Structural Biology. *J. Struct. Biol.* **2009**, *168* (1), 1–2.

(123) Wenger, J.; Rigneault, H.; Dintinger, J.; Marguet, D.; Lenne, P. F. Single-Fluorophore Diffusion in a Lipid Membrane over a Subwavelength Aperture. *J. Biol. Phys.* **2006**, *32* (1), 18–21.

(124) Samiee, K. T.; Moran-Mirabal, J. M.; Cheung, Y. K.; Craighead, H. G. Zero Mode Waveguides for Single-Molecule Spectroscopy on Lipid Membranes. *Biophys. J.* **2006**, *90* (9), 3288–3299.

(125) Groves, J. T.; Ulman, N.; Boxer, S. G. Micropattering Fluid Lipid Bilayers on Solid Supports. *Science (80-.).* **1997**, *275* (1997), 651–653.

(126) Groves, J. T.; Boxer, S. G. Micropattern Formation in Supported Lipid Membranes. *Acc. Chem. Res.* **2002**, *35* (3), 149–157.

(127) Salafsky, J.; Groves, J. T.; Boxer, S. G. Architecture and Function of Membrane Proteins

124

in Planar-Supported Bilayers: A Study with Photosynthetic Reaction Centers. *Biochemistry* **1996**, *35* (47), 14773–14781.

(128) Stuurman, N.; Edelstein, A. D.; Amodaj, N.; Hoover, K.; Vale, R. D. Computer Control of Microscopes Using Manager. *Current Protocols in Molecular Biology*. Current Protocols in Molecular Biology 2010, pp 1–22.

(129) Ensign, D. L.; Pande, V. S. Bayesian Detection of Intensity Changes in Single Molecule and Molecular Dynamics Trajectories. *J. Phys. Chem. B* **2010**, *114* (1), 280–292.

(130) Palik, E. D. *Handbook of Optical Constants of Solids*; 1998.

(131) Vörös, J. The Density and Refractive Index of Adsorbing Protein Layers. *Biophys. J.* **2004**, *87* (1), 553–561.

(132) Costner, E. a.; Long, B. K.; Navar, C.; Jockusch, S.; Lei, X.; Zimmerman, P.; Campion, A.; Turro, N. J.; Grant Willson, C. Fundamental Optical Properties of Linear and Cyclic Alkanes: VUV Absorbance and Index of Refraction. *J. Phys. Chem. A* **2009**, *113* (33), 9337–9347.

(133) King, G. I.; White, S. H. Determining Bilayer Hydrocarbon Thickness from Neutron Diffraction Measurements Using Strip-Function Models. *Biophys. J.* **1986**, *49* (5), 1047–1054.

(134) Christensen, S. M.; Tu, H.-L.; Jun, J. E.; Alvarez, S.; Triplet, M. G.; Iwig, J. S.; Yadav, K. K.; Bar-Sagi, D.; Roose, J. P.; Groves, J. T. One-Way Membrane Trafficking of SOS in Receptor-Triggered Ras Activation. *Nat. Struct. Mol. Biol.* **2016**, *23* (9), 838–846.

(135) Campbell, S. L.; Khosravi-Far, R.; Rossman, K. L.; Clark, G. J.; Der, C. J. Increasing Complexity of Ras Signaling. *Oncogene* **1998**, No. 17, 1395–1413.

(136) Chang, L.; Karin, M. Mammalian MAP Kinase Signalling Cascades. *Nature* **2001**, *410* (6824), 37–40.

(137) Groves, J. T.; Kuriyan, J. Molecular Mechanisms in Signal Transduction at the Membrane. *Nat. Struct. {&} Mol. Biol.* **2010**, *17* (6), 659–665.

(138) Jun, J. E.; Rubio, I.; Roose, J. P. Regulation of Ras Exchange Factors and Cellular Localization of Ras Activation by Lipid Messengers in T Cells. *Front. Immunol.* **2013**, *4* (SEP), 13–15.

(139) Egan, S. E.; Giddings, B. W.; Brooks, M. W.; Buday, L.; Sizeland, A. M.; Weinberg, R. A. Association of Sos Ras Exchange Protein with Grb2 Is Implicated in Tyrosine Kinase Signal Transduction and Transformation. *Nature* **1993**, *363* (6424), 45–51.

(140) Genot, E.; Cantrell, D. A. Ras Regulation and Function in Lymphocytes. *Curr. Opin. Immunol.* **2000**, *12* (3), 289–294.

(141) Kortum, R. L.; Sommers, C. L.; Alexander, C. P.; Pinski, J. M.; Li, W.; Grinberg, A.; Lee, J.; Love, P. E.; Samelson, L. E. Targeted Sos1 Deletion Reveals Its Critical Role in Early T-Cell Development. *Proc. Natl. Acad. Sci. U. S. A.* **2011**, *108* (30), 12407–12412.

(142) Baltanás, F. C.; Pérez-Andrés, M.; Ginel-Picardo, A.; Diaz, D.; Jimeno, D.; Liceras-Boillos, P.; Kortum, R. L.; Samelson, L. E.; Orfao, A.; Santos, E. Functional Redundancy of Sos1 and Sos2 for Lymphopoiesis and Organismal Homeostasis and Survival. *Mol. Cell. Biol.* **2013**, *33* (22), 4562–4578.

(143) Wang, D. Z. M.; Hammond, V. E.; Abud, H. E.; Bertoncello, I.; McAvoy, J. W.; Bowtell, D. D. L. Mutation in Sos1 Dominantly Enhances a Weak Allele of the EGFR, Demonstrating a Requirement for sos1 in EGFR Signaling and Development. *Genes Dev.* **1997**, *11* (3), 309–320.

(144) Findlay, G. M.; Smith, M. J.; Lanner, F.; Hsiung, M. S.; Gish, G. D.; Petsalaki, E.; Cockburn, K.; Kaneko, T.; Huang, H.; Bagshaw, R. D.; et al. Interaction Domains of Sos1/Grb2 Are Finely Tuned for Cooperative Control of Embryonic Stem Cell Fate. *Cell* **2013**, *152* (5), 1008–1020.

(145) Buday, L.; Downward, J. Epidermal Growth Factor Regulates p21ras through the Formation of a Complex of Receptor, Grb2 Adapter Protein, and Sos Nucleotide Exchange Factor. *Cell* **1993**, *73* (3), 611–620.

(146) Gale, N. W.; Kaplan, S.; Lowenstein, E. J.; Schlessinger, J.; Bar-Sagi, D. Grb2 Mediates the EGF-Dependent Activation of Guanine Nucleotide Exchange on Ras. *Nature* **1993**, *363* (6424), 88–92.

(147) Li, N.; Batzer, A.; Daly, R.; Yajnik, V.; Skolnik, E.; Chardin, P.; Bar-Sagi, D.; Margolis, B.; Schlessinger, J. Guanine-Nucleotide-Releasing Factor hSos1 Binds to Grb2 and Links Receptor Tyrosine Kinases to Ras Signalling. *Nature* **1993**, *363* (6424), 85–88.

(148) Rozakis-Adcock, M.; Fernley, R.; Wade, J.; Pawson, T.; Bowtell, D. The SH2 and SH3 Domains of Mammalian Grb2 Couple the EGF Receptor to the Ras Activator mSos1. *Nature* **1993**, *363*, 88–92.

(149) Waterman, H.; Katz, M.; Rubin, C.; Shtiegman, K.; Lavi, S.; Elson, A.; Jovin, T.; Yarden, Y. A Mutant EGF-Receptor Defective in Ubiquitylation and Endocytosis Unveils a Role for Grb2 in Negative Signaling. *EMBO J.* **2002**, *21* (3), 303–313.

(150) Chardin, P.; Camonis, J. H.; Gale, N. W.; van Aelst, L.; Schlessinger, J.; Wigler, M. H.; Bar-Sagi, D. Human Sos1: A Guanine Nucleotide Exchange Factor for Ras That Binds to

GRB2. *Science* **1993**, *260* (5112), 1338–1343.

(151) Yadav, K. K.; Bar-Sagi, D. Allosteric Gating of Son of Sevenless Activity by the Histone Domain. *Proc. Natl. Acad. Sci. U. S. A.* **2010**, *107* (8), 3436–3440.

(152) Margarit, S. M.; Sondermann, H.; Hall, B. E.; Nagar, B.; Hoelz, A.; Pirruccello, M.; Bar-sagi, D.; Kuriyan, J.; Brook, S.; York, N. Structural Evidence for Feedback Activation by Ras · GTP of the Ras-Specific Nucleotide Exchange Factor SOS State University of New York at Stony Brook. **2003**, *112*, 685–695.

(153) Kholodenko, B. N.; Hoek, J. B.; Westerhoff, H. V. Why Cytoplasmic Signalling Proteins Should Be Recruited to Cell Membranes. *Trends Cell Biol.* **2000**, *10* (5), 173–178.

(154) Karlovich, C. A.; Bonfini, L.; Mccollam, L.; Rogge, R. D.; Daga, A.; Czech, M. P. In Vivo Functional Analysis of the Ras Exchange Factor Son of Sevenless Author (S): Chris A . Karlovich , Laura Bonfini , Linda McCollam , Ronald D . Rogge , Andrea Daga , Michael P . Czech and Utpal Banerjee Published by : American Association for the . **2017**, *268* (5210), 576–579.

(155) Corbalan-Garcia, S.; Margarit, S. M.; Galron, D.; Yang, S. S.; Bar-Sagi, D. Regulation of Sos Activity by Intramolecular Interactions. *Mol. Cell. Biol.* **1998**, *18* (2), 880–886.

(156) McCollam, L.; Bonfini, L.; Karlovich, C. A.; Conway, B. R.; Kozma, L. M.; Banerjee, U.; Czech, M. P. Functional Roles for the Pleckstrin and Dbl Homology Regions in the Ras Exchange Factor Son-of-Sevenless. **1995**, *270* (27), 15954–15957.

(157) Wang, W.; Fisher, E. M. C.; Jia, Q.; Dunn, J. M.; Porfiri, E.; Downward, J.; Egan, S. E. The Grb2 Binding Domain of mSos1 Is Not Required for Downstream Signal Transduction. *Nat. Genet.* **1995**, *10* (3), 294–300.

(158) Zhao, C.; Du, G.; Skowronek, K.; Frohman, M. A.; Bar-Sagi, D. Phospholipase D2-Generated Phosphatidic Acid Couples EGFR Stimulation to Ras Activation by Sos. *Nat. Cell Biol.* **2007**, *9* (6), 706–712.

(159) Roose, J. P.; Mollenauer, M.; Ho, M.; Kurosaki, T.; Weiss, A. Unusual Interplay of Two Types of Ras Activators, RasGRP and SOS, Establishes Sensitive and Robust Ras Activation in Lymphocytes. *Mol Cell Biol* **2007**, *27* (7), 2732–2745.

(160) Chen, R. H.; Corbalan-Garcia, S.; Bar-Sagi, D. The Role of the PH Domain in the Signal-Dependent Membrane Targeting of Sos. *EMBO J.* **1997**, *16* (6), 1351–1359.

(161) Lin, W. C.; Iversen, L.; Tu, H. L.; Rhodes, C.; Christensen, S. M.; Iwig, J. S.; Hansen, S. D.; Huang, W. Y.; Groves, J. T. H-Ras Forms Dimers on Membrane Surfaces via a Protein-Protein Interface. *Proc Natl Acad Sci U S A* **2014**, *111* (8), 2996–3001.

(162) Boykevisch, S.; Zhao, C.; Sondermann, H.; Philippidou, P.; Halegoua, S.; Kuriyan, J.; Bar-Sagi, D. Regulation of Ras Signaling Dynamics by Sos-Mediated Positive Feedback. *Curr. Biol.* **2006**, *16* (21), 2173–2179.

(163) Hall, B. E.; Yang, S. S.; Boriack-Sjodin, P. A.; Kuriyan, J.; Bar-Sagi, D. Structure-Based Mutagenesis Reveals Distinct Functions for Ras Switch 1 and Switch 2 in Sos-Catalyzed Guanine Nucleotide Exchange. *J. Biol. Chem.* **2001**, *276* (29), 27629–27637.

(164) Sondermann, H.; Soisson, S. M.; Boykevisch, S.; Yang, S. S.; Bar-Sagi, D.; Kuriyan, J. Structural Analysis of Autoinhibition in the Ras Activator Son of Sevenless. *Cell* **2004**, *119* (3), 393–405.

(165) Kubiseski, T. J.; Chook, Y. M.; Parris, W. E.; Rozakis-Adcock, M.; Pawson, T. High Affinity Binding of the Pleckstrin Homology Domain of mSos1 to Phosphatidylinositol (4,5)-Bisphosphate. *J Biol Chem* **1997**, *272* (3), 1799–1804.

(166) Oh-hora, M.; Johmura, S.; Hashimoto, A.; Hikida, M.; Kurosaki, T. Requirement for Ras Guanine Nucleotide Releasing Protein 3 in Coupling Phospholipase C-gamma2 to Ras in B Cell Receptor Signaling. *J. Exp. Med.* **2003**, *198* (12), 1841–1851.

(167) Sondermann, H.; Nagar, B.; Bar-Sagi, D.; Kuriyan, J. Computational Docking and Solution X-Ray Scattering Predict a Membrane-Interacting Role for the Histone Domain of the Ras Activator Son of Sevenless. *Proc. Natl. Acad. Sci. U. S. A.* **2005**, *102* (46), 16632–16637.

(168) Aronheim, A.; Engelberg, D.; Li, N.; Al-Alawi, N.; Schlessinger, J.; Karin, M. Membrane Targeting of the Nucleotide Exchange Factor Sos Is Sufficient for Activating the Ras Signaling Pathway. *Cell* **1994**, *78* (6), 949–961.

(169) Mossman, K. D.; Campi, G.; Groves, J. T.; Dustin, M. L. Altered TCR Signaling from Geometrically Repatterned Immunological Synapses. **2010**, *1191* (2005).

(170) Davey, A. M.; Liu, W.; Sohn, H. W.; Brzostowski, J.; Pierce, S. K. *Understanding the Initiation of B Cell Signaling through Live Cell Imaging*, 1st ed.; Elsevier Inc., 2012; Vol. 506.

(171) Balagopalan, L.; Sherman, E.; Barr, V.; Samelson, L. Imaging Techniques for Assaying Lymphocyte Activation in Action. *Nat. Rev. Immunol.* **2011**, *11*, 21–33.

(172) Grakoui, A.; Bromley, S. K.; Sumen, C.; Davis, M. M.; Shaw, A. S.; Allen, P. M.; Dustin, M. L. The Immunological Synapse : A Molecular Machine Controlling T Cell Activation. **2013**, *285* (5425), 221–227.

(173) Weber, M.; Treanor, B.; Depoil, D.; Shinohara, H.; Harwood, N. E.; Hikida, M.;

Kurosaki, T.; Batista, F. D. Phospholipase C-gamma2 and Vav Cooperate within Signaling Microclusters to Propagate B Cell Spreading in Response to Membrane-Bound Antigen. *J. Exp. Med.* **2008**, *205* (4), 853–868.

(174) Brdička, T.; Imrich, M.; Angelisová, P.; Brdičková, N.; Horváth, O.; Špička, J.; Hilgert, I.; Lusková, P.; Dráber, P.; Novák, P.; et al. Non–T Cell Activation Linker (NTAL). *J. Exp. Med.* **2002**, *196* (12), 1617–1626.

(175) Janssen, E.; Zhu, M.; Zhang, W.; Koonpaew, S. LAB: A New Membrane-Associated Adaptor Molecule in B Cell Activation. *Nat Immunol* **2003**, *4* (2), 117–123.

(176) Pierce, S. K.; Liu, W. The Tipping Points in the Initiation of B Cell Signalling: How Small Changes Make Big Differences. *Nat. Rev. Immunol.* **2010**, *10* (11), 767–777.

(177) Stenmark, H. Rab GTPases as Coordinators of Vesicle Traffic. *Nat. Rev. Mol. Cell Biol.* **2009**, *10* (8), 513–525.

(178) Iwig, J. S.; Vercoulen, Y.; Das, R.; Barros, T.; Limnander, A.; Che, Y.; Pelton, J. G.; Wemmer, D. E.; Roose, J. P.; Kuriyan, J. Structural Analysis of Autoinhibition in the Ras-Specific Exchange Factor RasGRP1. *Elife* **2013**, *2013* (2), 1–28.

(179) Daley, S. R.; Coakley, K. M.; Hu, D. Y.; Randall, K. L.; Jenne, C. N.; Limnander, A.; Myers, D. R.; Polakos, N. K.; Enders, A.; Roots, C.; et al. Rasgrp1 Mutation Increases Native T-Cell CD44 Expression and Drives mTOR-Dependent Accumulation of Helios+ T Cells and Autoantibodies. *Elife* **2013**, *2013* (2), 1–26.

(180) Rojas, J. M.; Oliva, J. L.; Santos, E. Mammalian Son of Sevenless Guanine Nucleotide Exchange Factors: Old Concepts and New Perspectives. *Genes Cancer* **2011**, *2* (3), 298–305.

(181) Greene, A. C.; Lord, S. J.; Tian, A.; Rhodes, C.; Kai, H.; Groves, J. T. Spatial Organization of epha2 at the Cell-Cell Interface Modulates Trans-Endocytosis of ephrina1. *Biophys. J.* **2014**, *106* (10), 2196–2205.

(182) Baines, A. T.; Xu, D.; Der, C. J. Inhibition of Ras for Cancer Treatment: The Search Continues. *Future Med. Chem.* **2011**, *3* (14), 1787–1808.

(183) Zimmermann, G.; Papke, B.; Ismail, S.; Vartak, N.; Chandra, A.; Hoffmann, M.; Hahn, S. a; Triola, G.; Wittinghofer, A.; Bastiaens, P. I. H.; et al. Small Molecule Inhibition of the KRAS-PDEδ Interaction Impairs Oncogenic KRAS Signalling. *Nature* **2013**, *497* (7451), 638–642.

(184) Ostrem, J. M.; Peters, U.; Sos, M. L.; Wells, J. A.; Shokat, K. M. K-Ras(G12C) Inhibitors Allosterically Control GTP Affinity and Effector Interactions. *Nature* **2013**, *503* (7477),

548–551.

(185) Dhawan, N. S.; Scopton, A. P.; Dar, A. C. Small Molecule Stabilization of the KSR Inactive State Antagonizes Oncogenic Ras Signalling. *Nature* **2016**, *537* (7618), 112–116.

(186) Pawson, T.; Scott, J. D. Signaling through Scaffold, Anchoring, and Adaptor Proteins. *Science (80-.).* **1997**, *278* (5346), 2075–2080.

(187) Vetter, I. R.; Wittinghofer, A. The Guanine Nucleotide-Binding Switch in Three Dimensions. *Science (80-.).* **2001**, *294* (5545), 1299–1304.

(188) Boriack-Sjodin, P. a; Margarit, S. M.; Bar-Sagi, D.; Kuriyan, J. The Structural Basis of the Activation of Ras by Sos. *Nature* **1998**, *394* (6691), 337–343.

(189) Lenzen, C.; Cool, R. H.; Prinz, H.; Kuhlmann, J.; Wittinghofer, A. Kinetic Analysis by Fluorescence of the Interaction between Ras and the Catalytic Domain of the Guanine Nucleotide Exchange Factor Cdc25 ^{Mm} †. *Biochemistry* **1998**, *37* (20), 7420–7430.

(190) Nussinov, R.; Tsai, C. J.; Mattos, C. "Pathway Drug Cocktail": Targeting Ras Signaling Based on Structural Pathways. *Trends Mol. Med.* **2013**, *19* (11), 695–704.

(191) Scheffzek, K.; Ahmadian, M. R.; Wittinghofer, A. GTPase-Activating Proteins: Helping Hands to Complement an Active Site. *Trends Biochem. Sci.* **1998**, *23* (7), 257–262.

(192) Maegley, K. a; Admiraal, S. J.; Herschlag, D. Ras-Catalyzed Hydrolysis of GTP: A New Perspective from Model Studies. *Proc. Natl. Acad. Sci. U. S. A.* **1996**, *93* (August), 8160–8166.

(193) Wittinghofer, A.; Scheffzek, K.; Ahmadian, M. R. The Interaction of Ras with GTPase-Activating Proteins. *FEBS Lett.* **1997**, *410* (1), 63–67.

(194) Zhang, J.; Nussinov, R. Drugging Ras GTPase: A Comprehensive Mechanistic and Signaling Structural View. *Chem. Soc. Rev.* **2016**, *45* (18), 4929–4952.

(195) Vetter, I. R. Interface Analysis of Small GTP Binding Protein Complexes Suggests Preferred Membrane Orientations. **2017**, *398*, 637–651.

(196) Behnia, R.; Munro, S. Organelle Identity and the Signposts for Membrane Traffic. *Nature* **2005**, *438* (7068), 597–604.

(197) Beck, R.; Sun, Z.; Adolf, F.; Rutz, C.; Bassler, J.; Wild, K.; Sinning, I.; Hurt, E.; Brügger, B.; Béthune, J.; et al. Membrane Curvature Induced by Arf1-GTP Is Essential for Vesicle Formation. *Proc. Natl. Acad. Sci. USA* **2008**, *105* (33), 11731–11736.

(198) Beck, R.; Prinz, S.; Diestelkötter-Bachert, P.; Röhling, S.; Adolf, F.; Hoehner, K.; Welsch,

S.; Ronchi, P.; Brügger, B.; Briggs, J. a G.; et al. Coatomer and Dimeric ADP Ribosylation Factor 1 Promote Distinct Steps in Membrane Scission. *J. Cell Biol.* **2011**, *194* (5), 765–777.

(199) Bottanelli, F.; Kilian, N.; Ernst, A. M.; Rivera-molina, F.; Schroeder, L. K.; Kromann, E. B.; Lessard, M. D.; Roman, S.; Schepartz, A.; Baddeley, D.; et al. A Novel Physiological Role for ARF1 in the Formation of Bi-Directional Tubules from the Golgi. *Mol. Biol. Cell* **2017**.

(200) Humphreys, D.; Davidson, A.; Hume, P. J.; Koronakis, V. Salmonella Virulence Effector SopE and Host GEF ARNO Cooperate to Recruit and Activate WAVE to Trigger Bacterial Invasion. *Cell Host Microbe* **2012**, *11* (2), 129–139.

(201) Davidson, A. C.; Humphreys, D.; Brooks, A. B. E.; Hume, P. J.; Koronakis, V. The Arf GPTase-Activating Protein Family Is Exploited by Salmonella Enterica Serovar Typhimurium To Invade Nonphagocytic Host Cells. **2015**, *6* (1), 1–11.

(202) Sabe, H.; Hashimoto, S.; Morishige, M.; Ogawa, E.; Hashimoto, A.; Nam, J. M.; Miura, K.; Yano, H.; Onodera, Y. The EGFR-GEP100-Arf6-AMAP1 Signaling Pathway Specific to Breast Cancer Invasion and Metastasis. *Traffic* **2009**, *10* (8), 982–993.

(203) Franco, M.; Chardin, P.; Chabre, M.; Paris, S. Myristoylation of ADP-Ribosylation Factor 1 Facilitates Nucleotide Exchange at Physiological Mg2+ Levels. *Journal of Biological Chemistry*. 1995, pp 1337–1341.

(204) Randazzo, P. a; Terui, T.; Sturch, S.; Fales, H. M.; Ferrige, a G.; Kahn, R. a. The Myristoylated Amino Terminus of ADP-Ribosylation Factor 1 Is a Phospholipid- and GTP-Sensitive Switch. *The Journal of biological chemistry*. 1995, pp 14809–14815.

(205) Goldberg, J. Structural Basis for Activation of ARF GTPase. *Cell* **1998**, *95* (2), 237–248.

(206) Cherfils, J.; Ménétrey, J.; Mathieu, M. Structure of the Sec7 Domain of the Arf Exchange Factor ARNO. *Nature* **1998**, *392* (6671), 101–105.

(207) Mossessova, E.; Gulbis, J. M.; Goldberg, J. Structure of the Guanine Nucleotide Exchange Factor Sec7 Domain of Human Arno and Analysis of the Interaction with ARF GTPpase. *Cell* **1998**, *92* (3), 415–423.

(208) Paris, S.; Berauddufour, S.; Robineau, S.; Bigay, J.; Antonny, B.; Chabre, M.; Chardin, P. Role of Protein Phospholipid Interactions in the Activation of ARF1 by the Guanine Nucleotide Exchange Factor Arno. *J. Biol. Chem.* **1997**, *272* (35), 22221–22226.

(209) Cohen, L. A.; Honda, A.; Varnai, P.; Brown, F. D.; Balla, T.; Donaldson, J. G. Active Arf6 Recruits ARNO/cytohesin GEFs to the PM by Binding Their PH Domains. *Mol.*

Biol. Cell **2007**, *18* (6), 2244–2253.

(210) Roy, N. S.; Yohe, M. E.; Randazzo, P. A.; Gruschus, J. M. Allosteric Properties of PH Domains in Arf Regulatory Proteins. *Cell. Logist.* **2016**, *6* (2), e1181700.

(211) Malaby, A. W.; van den Berg, B.; Lambright, D. G. Structural Basis for Membrane Recruitment and Allosteric Activation of Cytohesin Family Arf GTPase Exchange Factors. *Proc. Natl. Acad. Sci. U. S. A.* **2013**, *110* (35), 14213–14218.

(212) Nawrotek, A.; Zeghouf, M.; Cherfils, J. Allosteric Regulation of Arf GTPases and Their GEFs at the Membrane Interface. **2016**, *1248* (September).

(213) Macia, E.; Chabre, M.; Franco, M. Specificities for the Small G Proteins ARF1 and ARF6 of the Guanine Nucleotide Exchange Factors ARNO and EFA6. *J. Biol. Chem.* **2001**, *276* (27), 24925–24930.

(214) Liu, Y.; Kahn, R. a; Prestegard, J. H. Dynamic Structure of Membrane-Anchored Arf*GTP. *Nat. Struct. Mol. Biol.* **2010**, *17* (7), 876–881.

(215) Jackson, C. L.; Casanova, J. E. Turning on ARF: The Sec7 Family of Guanine-Nucleotide-Exchange Factors. *Trends Cell Biol.* **2000**, *10* (2), 60–67.

(216) Macia, E.; Paris, S.; Chabre, M. Binding of the PH and Polybasic C-Terminal Domains of ARNO to Phosphoinositides and to Acidic Lipids. *Biochemistry* **2000**, *39* (19), 5893–5901.

(217) Frank, S.; Upender, S.; Hansen, S. H.; Casanova, J. E. ARNO Is a Guanine Nucleotide Exchange Factor for ADP-Ribosylation Factor 6. *J. Biol. Chem.* **1998**, *273* (1), 23–27.

(218) Stalder, D.; Barelli, H.; Gautier, R.; Macia, E.; Jackson, C. L.; Antonny, B. Kinetic Studies of the Arf Activator Arno on Model Membranes in the Presence of Arf Effectors Suggest Control by a Positive Feedback Loop. *J. Biol. Chem.* **2011**, *286* (5), 3873–3883.

(219) Knight, J. D.; Falke, J. J. Single-Molecule Fluorescence Studies of a PH Domain : New Insights into the Membrane Docking Reaction. *Biophysj* **2009**, *96* (2), 566–582.

(220) Jian, X.; Cavenagh, M.; Gruschus, J. M.; Randazzo, P. A.; Kahn, R. A. Modifications to the C-Terminus of Arf1 Alter Cell Functions and Protein Interactions. *Traffic* **2010**, *11* (6), 732–742.

(221) Tinevez, J.; Perry, N.; Schindelin, J.; Hoopes, G. M.; Reynolds, G. D.; Laplantine, E.; Bednarek, S. Y.; Shorte, S. L.; Eliceiri, K. W. TrackMate : An Open and Extensible Platform for Single-Particle Tracking. *Methods* **2017**, *115*, 80–90.